This is to certify that the

dissertation entitled

ELECTRONIC TRANSPORT IN DOPED CVD

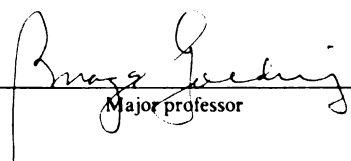DIAMOND MICROCRYSTALS

presented by

Michael D. Jaeger

has been accepted towards fulfillment
of the requirements for

_____Ph.D._____ degree in _Physics_

_____
Major professor

Date _December 20, 1996_

PLACE IN RETURN BOX to remove this checkout from your record.
TO AVOID FINES return on or before date due.

DATE DUE	DATE DUE	DATE DUE
JUN 0 3 2004 060704	032 49 2053	_____
_____	_____	_____
_____	_____	_____
_____	_____	_____
_____	_____	_____
_____	_____	_____
_____	_____	_____

MSU Is An Affirmative Action/Equal Opportunity Institution
c:\circ\datedue.pm3-p.1

ELECTRONIC TRANSPORT IN DOPED CVD DIAMOND MICROCRYSTALS

By

Michael D. Jaeger

A DISSERTATION

Submitted to
Michigan State University
in partial fulfillment of the requirements
for the degree of

DOCTOR OF PHILOSOPHY

Department of Physics and Astronomy

1996

ABSTRACT

ELECTRONIC TRANSPORT IN DOPED CVD DIAMOND MICROCRYSTALS

By

Michael D. Jaeger

Electronic transport in polycrystalline semiconductors is complicated by the presence of structural disorder at grain boundaries. The contributions from disorder are poorly understood in polycrystalline diamond, which can now be produced as thin films on both diamond and non-diamond substrates by chemical vapor deposition (CVD). Understanding transport in doped polycrystalline diamond requires analysis of progressively more complex morphologies beginning with single-crystal diamond, diamond on non-diamond substrates, single grain boundaries, and, finally, finite networks of grains. Although transport in single-crystal diamond, both natural diamond and CVD homoepitaxial films, has been studied previously, there has not yet been a sufficiently careful examination of the significant deviations from single-crystal behavior arising in polycrystalline films.

This study represents the next logical step in clarifying the electronic properties of polycrystalline CVD diamond by examining transport in isolated diamond grains, nominally identical to those which comprise polycrystalline films. A novel lithographic contact technique based on electron-beam lithography has been developed to contact isolated single-crystal grains of micron size. The technique employed a large number of processing steps for forming suitably Ohmic contacts and for planarizing the diamond-substrate topography. Electrical transport measurements were conducted on isolated B-doped CVD diamond microcrystals over the temperature range 200 K to 435 K and compared to results for identically grown homoepitaxial and polycrystalline films. The geometrical factors which relate resistance measurements on 3-dimensional crystallites to resistivity were obtained by using finite element analysis to model the

current density in a digitized reconstruction of the crystallite. This approach should prove useful in studying transport in other materials for which large single-crystals cannot be grown.

The electrical conductivity was interpreted within a standard model for non-degenerate, weakly compensated semiconductors. The measured activation energy for valence band conduction due to B acceptors in microcrystals, $E_a = 0.35$ eV, was indistinguishable from that for the homoepitaxial film, but very different from that for the polycrystalline film, where $E_a = 0.20$ eV. This indicates that B dopants exist in similar structural environments in single-crystal diamond grown on diamond and on oxidized-silicon substrates. B in polycrystalline diamond also exists at the grain boundaries where lattice mismatch and higher B concentrations create disorder. The microcrystal resistivity was a factor of two higher than the homoepitaxial film. This is due either to lower doping concentrations or a smaller temperature independent mobility for microcrystals.

To my parents, David and Marlene Jaeger.

ACKNOWLEDGMENTS

I would first like to thank Professor Brage Golding for his guidance, support, and patience. He has been an excellent mentor and friend, and has given me the space and confidence to become an original thinker and to aspire for something more than mediocrity.

I would also like to thank Dr. Glenn Alers for taking me under his wing when I first started research. He has been a valuable friend, colleague, and second mentor ever since. His advice to "Just do it!" will ring in my ears for years to come.

Thanks goes to Mike Wilson for his friendship and enthusiasm for "really cool" experiments. Thanks also to my physics friends George Jeffers, Lily Hoines, Erik Hendrickson, and "Rooster," who gave a social atmosphere to long lab hours.

My lab mates, Lowell McCann, Amy Engebretson, and Wenhao Wu, bore the brunt of my anxious, at times frenzied, nature in the lab over the last couple of years.

The Dept. of Physics and Astronomy team, Reza Loloee, Mary Curtis, Tom Palazzolo, Jim Munz, Tom Hudson, Stephanie Holland, Sandy Teague, and Mark Olson, can't be praised enough for their efforts to help get things done quickly, easily, and with a smile.

My greatest appreciation goes out to my parents, David and Marlene Jaeger, for their support and encouragement throughout this research, my academic career, and my life. My brothers, Dan and Jon, helped in more ways than they know.

A special thanks to Mikki for her love and patience over the last two years. She was always there for me, and suffered the long hours and disappointments even more than I did.

I thank the Physics and Astronomy Department, the MSU Center for Fundamental Materials Research, and the NSF Center for Sensor Materials at MSU for financial support.

TABLE OF CONTENTS

LIST OF TABLES

LIST OF FIGURES

Chapter I

INTRODUCTION

1. DIAMOND: A CRYSTALLINE SOLID WITH UNUSUAL ELECTRONIC AND PHYSICAL PROPERTIES

Semiconducting diamond is a condensed matter system with a unique combination of unusual electrical and physical properties. The gap between the valence and conduction bands of diamond is 5.45 eV, which is much larger than the gap of group IV semiconductors in common use in devices such as Si (1.12 eV), Ge (0.66 eV), or III-V compounds such as GaAs (1.42 eV). The large bandgap means that pure diamond remains a good insulator at much higher temperatures than other semiconductors since carriers require 5.45 eV to be thermally excited across the energy gap. (See Figure 1.) The few known chemical impurities which are electron donors or acceptors in diamond create states which sit relatively deep in the gap (> 0.3 eV). B and P are common shallow dopants in Si and lie 45 meV above the valence band and 45 meV below the conduction band, respectively. An attractive feature of wide bandgap semiconductors is therefore a conductivity that can be controlled at moderate temperatures by varying the amount of impurities present without
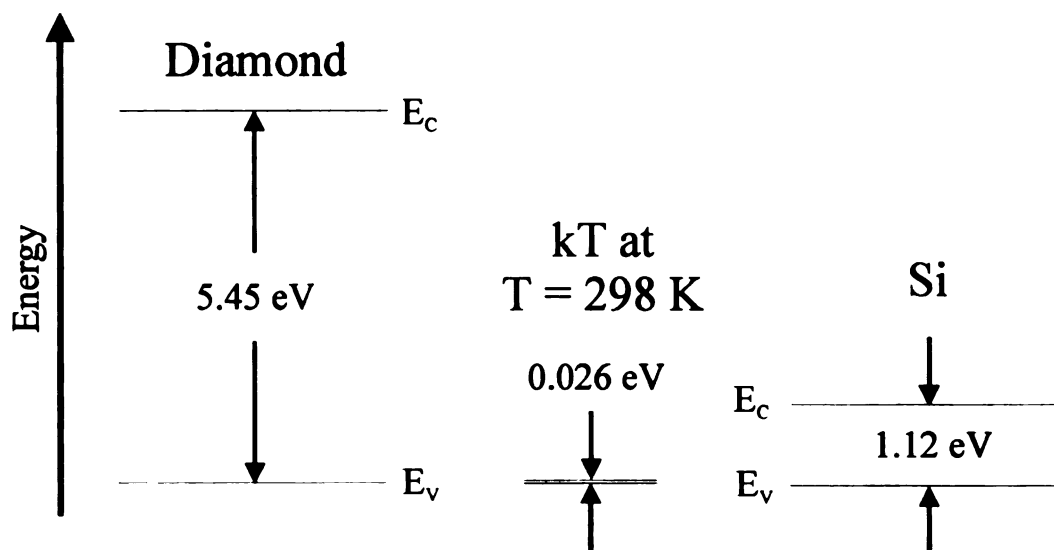
Figure 1 Schematic diagram of band gap energy for diamond and Si compared to room temperature.

1

leading to thermal saturation until very high temperatures (> 600 °C). The wide bandgap also leads to very low optical absorption throughout the visible part of the spectrum.

Many of diamond's extreme properties are a consequence of its small lattice constant and strong interatomic bonding. It is the hardest material known, possesses the highest thermal conductivity of any material at room temperature, and is very resistant to radiation damage. Charge carrier mobilities in diamond can also be larger than 2000 cm^2/V-s, greater than Si or other wide bandgap materials, though less than high mobility GaAs. (See Table 5, page 50.)

Natural diamond may possess finite electrical conductivity as a result of impurity states and has been studied since the early 1900's. Research was stimulated in 1955 with a report by General Electric of discovery of a high-temperature high-pressure (HTHP) process for synthetic diamond. Interest in diamond was revived again in the last two decades due to the discovery of a chemical vapor deposition (CVD) process for growing diamond films. The CVD process has allowed a higher degree of control over properties such as sample morphology and dopant levels.

At present, only CVD diamond films grown homoepitaxially on natural diamond substrates approach the crystallographic perfection and characteristic properties of natural diamond. Films produced on non-diamond substrates are usually polycrystalline, possessing high densities of structural defects such as grain boundaries, twins, and dislocations. Such thin polycrystalline films are composed of individual diamond grains which nucleate at isolated centers, grow, and ultimately coalesce to form a continuous film. Grain sizes may range from less than a micron for very thin films to tens of microns for very thick films. The defects in these films significantly affect their electrical and thermal transport properties. For example, polycrystalline films exhibit hole mobility two orders of magnitude lower than simultaneously grown homoepitaxial films[1] and thermal conductivity an order of magnitude lower. In polycrystalline semiconductors, grain boundaries are regions of disorder, often containing unsatisfied bonds which can trap impurities and charge carriers. Extensive work has gone into explaining these effects in polycrystalline Si. However, the

role played by such defects in polycrystalline diamond is not yet clear. The electrical and physical differences between diamond and smaller bandgap semiconductors are great enough that the character of grain boundaries in diamond is expected to be very different from Si. The most notable difference is that while both diamond and Si have tetrahedrally coordinated bond structure, there is a second stable phase of carbon, namely graphite, which can coexist with diamond and which has very different electrical properties from diamond. Graphite has trigonally coordinated bonding and is likely to occur in diamond grain-boundaries where lattice mismatches make it difficult to satisfy full tetrahedral bonding for all atoms.

2. OVERVIEW OF PRESENT RESEARCH

Transport in polycrystalline diamond is determined by a combination of effects due to intragrain properties, intergrain properties (grain boundaries), and possibly interactions between the two. Strain effects associated with non-diamond substrates may play a role, as may inhomogeneous dopant incorporation. Natural single-crystal diamond represents the simplest doped diamond system, since it is of high crystalline quality and is relatively strain free. It has been the subject of much research, but the dopant levels cannot be controlled. Homoepitaxial CVD diamond films offer highly strain-free single-crystal material, like natural diamond, but with controlled doping levels. CVD diamond on non-diamond substrates adds strain effects due to lattice mismatch with non-diamond substrates, and polycrystalline diamond includes the same effects as each of the above systems with the additional complication of grain boundaries.

This study compares the transport properties of three fundamental systems of boron-doped CVD diamond. The materials studied are: homoepitaxial diamond, single-crystal diamond on a non-diamond substrate, and polycrystalline diamond on a non-diamond substrate, all deposited under identical CVD conditions. The temperature-dependent electronic transport properties are analyzed using standard models for lightly-doped semiconductors, allowing for weak compensation.

This work represents the first transport measurements of single-crystal diamond grown on a non-diamond substrate. Since it is not currently possible to grow large area single crystal diamond on non-diamond substrates, we have accomplished this by measuring isolated, micron-sized diamond grain structures. If allowed to coalesce, the crystals would form polycrystalline films. Electrical transport measurements on these micron-sized structures are conducted using submicron electrical contacts fabricated using a complex lithographic technique specially developed for this study. The transport measurements in themselves require addressing the physics of metal-semiconductor contacts and small-scale transport in a wide bandgap semiconductor. Interpretation of multiprobe resistance measurements requires knowledge of the appropriate geometrical factors relating resistance to resistivity. These factors are easily calculated for simple, standard geometries such as Hall-bars or cylinders, but are difficult or impossible to obtain in closed form for arbitrarily shaped structures, such as three-dimensional microcrystallites. Therefore, a method for obtaining the geometrical factors for crystallites has been developed which involves reconstructing the sample geometry from electron micrographs and numerically calculating the current flow using a finite element method.

This dissertation is organized as follows. After concluding this introductory chapter with a brief section on technological interest in CVD diamond, the physics of semiconductors and semiconductor devices which is relevant to this study is reviewed in Chapter II. As discussed above, CVD diamond is an imperfect material and its electronic properties are strongly affected by defects. Hence, Chapter III, outlines the relevant properties of carbon and the materials issues which influence the electrical properties of CVD diamond, such as diamond growth by CVD, dopant incorporation, diamond film morphology, and common defect characteristics. The physics underlying the electronic properties of diamond is then reviewed in Chapter IV. Chapter V describes the experiments and includes details on the sample growth and characterization, development of the lithographic technique, and a description of electrical transport measurements.

In Chapter VI the results are presented and analyzed to obtain resistivities. Conclusions are drawn in Chapter VII and recommendations made for further research.

Two appendices follow the presentation of the main body of this study. Appendix A provides detailed descriptions of the lithographic contact technique. Appendix B presents a study of ballistic transport measurements on Bi single-crystals with lithographically-produced point-contacts. This study served as a precursor to the developmental work on the lithographic contact process used in the diamond research.

3. APPLICATIONS OF CVD DIAMOND

Currently, most successful applications of diamond are based on its extreme hardness, low coefficient of friction, or high thermal conductivity. Diamond films are used as wear coatings for machine tools and artificial limb joints. The high thermal conductivity is useful as heat-sinks or heat-spreaders for high-power electronic devices. Diamond's high speed of sound makes it useful for surface acoustic wave devices which can be used for high-frequency filters.

Much of the interest in diamond as an electronic material is based on high carrier mobility and wide bandgap reported for natural single-crystal diamond. High mobility is useful for high-frequency applications and the wide bandgap, as stated above, is useful for high-temperature electronic applications. However, this high mobility is not realized in polycrystalline films. More important, there is no suitable n-type dopant for CVD diamond so that bipolar devices cannot be realized. High quality CVD films are transparent in the visible and infrared and have been used in IR windows. Specific surfaces of diamond possess negative electron affinity, making it attractive for cold cathode emitters in field-emission displays. This application seems promising since even poor quality, polycrystalline CVD diamond films function as reasonably good field emitters.

Chapter II

SEMICONDUCTOR PHYSICS

This chapter reviews the background physics necessary for discussing charge transport in semiconductors. It begins by introducing the concept of the effective mass, which allows the motion of wave-like charge carriers in a crystal to be described by classical equations of motion. A discussion on semiconductor statistics is then presented to introduce intrinsic and extrinsic conductivity, the concept of doping in semiconductors, the temperature dependence of the carrier density, and the concept of carrier mobility. Basic references are Sze,[2] Shockley,[3] and Blakemore.[4] The electronic properties of defects in semiconductors are briefly introduced and a model for the electronic effects of grain boundaries in Si is presented. The chapter concludes with a discussion of electrical effects at metal-semiconductor contacts, a particularly important topic for this research.

1. CONCEPT OF THE EFFECTIVE MASS

The dynamics of charge carriers in a metal or semiconductor are usually described using wave packets composed of Bloch wave functions $\psi_k = U_k(\vec{r})\exp\left[i(\vec{k}\cdot\vec{r} - \omega_k t)\right]$ in a periodic potential $V(\vec{r})$ created by the atomic cores of the atoms. The Bloch wave functions are plane waves of angular frequency ω and momentum vector $\vec{k}$ in reciprocal space. (See for example, Ashcroft and Mermin.[5]) The dynamics are obtained from the wave function $\psi_k(x,t)$ which satisfies the time-dependent Schrödinger equation $\dfrac{\hbar^2}{2m_0}\vec{\nabla}^2\psi + \left[E - V(\vec{r})\right]\psi = i\hbar\dfrac{\partial\psi}{\partial t}$. The motion of a charge carrier is described by the group velocity of the wave packet given by $\vec{v} = \dfrac{1}{\hbar}\vec{\nabla}_k E$, where $E = \hbar\omega$. The acceleration in an external field is given by[6]

$$\vec{a} = \frac{d\vec{v}}{dt} = \frac{1}{\hbar}\frac{d}{dt}\vec{\nabla}_k E = \frac{1}{\hbar}\vec{\nabla}_k\left[\vec{\nabla}_k E \cdot \frac{d\vec{k}}{dt}\right].$$

Substituting in the expression for force $\vec{F} = e\vec{\nabla}V = -\hbar\frac{d\vec{k}}{dt}$ gives

$$\vec{a} = \frac{-1}{\hbar^2}\vec{\nabla}_k\vec{\nabla}_k E \cdot \vec{F}$$

which has components

$$a_i = -\frac{1}{\hbar^2}\sum_j \frac{\partial^2 E}{\partial k_i \partial k_j}F_j.$$

The quantity m*, with elements given by

$$\left(m^{-1}\right)_{ij} = \frac{1}{\hbar^2}\left[\frac{\partial^2 E}{\partial k_i \partial k_j}\right],$$

is called the effective mass tensor. Replacing the rest mass of an electron m_0 by the effective mass

in the crystal lattice m* allows the charge carrier motion to be described by the laws of classical

motion since the mass renormalization accounts for the periodicity of the lattice. This greatly

simplifies the description of transport in semiconductors. For materials with ellipsoidal Fermi

surfaces the effective mass tensor diagonalizes to

$$\frac{1}{m^*} = \begin{bmatrix} 1/m_1 & 0 & 0 \\ 0 & 1/m_2 & 0 \\ 0 & 0 & 1/m_3 \end{bmatrix}$$

The simplest situation occurs for materials with a spherical Fermi surface in which the effective

mass components are the same and a scalar effective mass can be used $m^* = \hbar^2\left(\frac{\partial^2 E}{\partial k^2}\right)^{-1}$. Since

the effective mass is a result of the curvature of the E - k surfaces, charge carriers residing in

different energy bands in a material can have different effective masses. If the bands are

energetically degenerate at a given point in k-space, the carriers in the band with greater curvature

are called "light" and those in the band with lesser curvature are called "heavy." Such is the case for diamond which has a doubly degenerate valence band at $k = 0$. If the heavy hole effective mass is denoted by m_{hh} and the light hole effective mass by m_{lh}, then, assuming spherical constant-energy surfaces, the hole density of states (dos) effective mass m^*_{dos} for this situation is given by[7]

$$m^h_{dos} = \left(m_{lh}^{3/2} + m_{hh}^{3/2} \right)^{2/3}.$$ m^*_{dos} is used to describe the effective valence band density of states and is

the mass which is used in calculations involving the Hall coefficient. The conductivity effective

mass is given by $m_c^* \approx \left(m_{lh}^{3/2} + m_{hh}^{3/2} \right) \Big/ \left(m_{hh}^{1/2} + m_{lh}^{1/2} \right).$[7]

2. SEMICONDUCTOR STATISTICS

A. Carrier Concentration in an Undoped Semiconductor—Intrinsic Case

The charge carriers in a semiconductor obey Fermi-Dirac statistics. The probability that a state with energy E will be occupied an electron is given by the Fermi distribution $f(E)$ for spin-½ particles

$$f(E) = \frac{1}{1 + \exp[(E - E_F)/kT]}$$

where k is Boltzman's constant. The Fermi energy E_F is defined by the energy at which $f = 1/2$. If E_F is more than $4kT$ from either band edge, then the semiconductor is called nondegenerate and the distribution approaches the classical Boltzman distribution $f \cong \exp[-(E - E_F)/kT] \propto \exp(- E/kT)$. Since f is the fraction of states occupied by electrons, then $f_h = 1 - f$ is the fraction of states left occupied by holes, and

$$f_h \equiv 1 - f = \frac{1}{1 + \exp[(E_F - E)/kT]}.$$

In a pure semiconductor (no impurities) at $T = 0$, the valence band is completely full and the conduction band is completely empty so that no electrical transport can take place. As the temperature is increased, electrons are excited from the valence band to the conduction band, leaving behind a hole in the valence band. These excited electrons and holes can contribute to a current. The number of occupied conduction band states n is given by the integral of the product of the density of states in the conduction band and the probability that a state with energy E is occupied f. For the case in which E_F is several kT below the conduction band E_C in a non-degenerate semiconductor, Boltzman statistics may be used and the result is

$$n = N_C \exp\left(\frac{-(E_C - E_F)}{kT}\right),$$

where N_C is the effective density of states in the conduction band given by

$$N_C \equiv 2M_C \left(\frac{2\pi m^e_{dos} kT}{h^2}\right)^{3/2}.$$ M_C is the number of equivalent minima in the conduction band and

$m^e_{dos} = (m^*_1 m^*_2 m^*_3)^{1/3}$ is the density of states effective mass for electrons. Similarly, the number of occupied hole states in the valence band is given by

$$p = N_V \exp\left(\frac{-(E_F - E_V)}{kT}\right) \tag{1}$$

where N_V is the effective density of states in the valence band given by $N_V \equiv 2\left(\frac{2\pi m^h_{dos} kT}{h^2}\right)^{3/2}.$

The gap energy is $E_g = E_C - E_V$. The location of the Fermi level for an intrinsic semiconductor is obtained by equating the above expressions for n and p, and is given by

$$E_F = E_i = \frac{E_C + E_V}{2} + \frac{3kT}{4} \ln\left(\frac{m^h_{dos}}{m^e_{dos}}\right),$$

where i denotes an intrinsic conductor. The Fermi level generally lies very close to mid-gap for an intrinsic semiconductor.

Electrical neutrality in an *intrinsic* semiconductor requires equal densities of conduction band electrons n_o and valence band holes p_o at thermal equilibrium. Then $n_i = n_o = p_o$, where the i denotes intrinsic conduction and o denotes thermal equilibrium. The intrinsic carrier density is given by

$$n_i = \sqrt{np} = (N_V N_C)^{1/2} \exp(-E_i/kT). \tag{2}$$

This expression is known as the Law of Mass-Action. The term $(N_V N_C)^{1/2}$ varies as $T^{3/2}$, so most of the temperature dependence is in the exponential term. E_i may have an intrinsic temperature-dependence as well. The conductivity $\sigma = n_i e^2 <\tau>/m_c^*$, where $<\tau>$ is the average carrier lifetime, will vary as $\sigma = \sigma_0 \exp(-E_i/kT)$, assuming $<\tau>$ is temperature-independent.

B. Carrier Concentration in a Doped Semiconductor—Extrinsic Case

Semiconductors may contain impurities which can significantly affect the transport properties. The simplest way in which impurities can affect conduction is by acting as a dopant, ie. contributing free carriers. A dopant impurity usually differs by ±1 valence from the host semiconductor so that it can either donate (+ case) or accept (– case) an electron. Conduction by such impurity-originated charge carriers is called *extrinsic* conduction. Shallow donor states lie just below the conduction band and acceptor states lie just above the valence band, so that the addition of a small amount of energy E_a equal to the energy difference between the respective band and the impurity state results in ionization of the impurity atom and freeing of the charge carrier. The number of dopant atoms which are thermally ionized in this way (electrically active) is given by[8]

$$N_D^+ = N_D \left(1 - \left[1 + \frac{1}{g} \exp\left(\frac{E_D - E_F}{kT}\right) \right]^{-1} \right) \tag{3}$$

for donors and

$$N_A^- = \frac{N_A}{1 + g\exp\left(\dfrac{E_A - E_F}{kT}\right)} \tag{4}$$

for acceptors, where E_D and E_A are the energies of the respective impurity levels. The constant g in these expressions is the ground-state degeneracy of the respective impurity band, and equals 4 for acceptor levels of Si, Ge, and diamond because the levels are twofold degenerate.

C.   Carrier Concentration in a p-type Compensated Semiconductor

For cases where both donors and acceptor impurities are present, the net difference of the active populations of each determines the number of carriers and the conductivity type (electron or hole). This situation is called *compensation* since the effects of the active minority carrier species counteract the effects of an equal population of the active majority carrier species. The carrier concentrations of a compensated semiconductor are determined by the condition of charge neutrality,

$$n + N_A^- = p + N_D^+. \tag{5}$$

For a p-type compensated system, holes are the majority carrier and electrons the minority carrier. If the minority carrier concentration can be neglected, then $p = N_A^- - N_D^+$. To find the number of holes, first combine this expression for p with that for N_A^- from Equation 4 above to get

$$\frac{(p + N_D^+)}{(N_A - N_D^+ - p)} = \frac{1}{g}\exp\left(\frac{E_F - E_A}{kT}\right).$$

Next assume that p is low enough to avoid complications due to degeneracy and obeys Boltzman statistics so that Equation 1 can be used for $\exp(E_F/kT)$. The density of holes then depends on the temperature according to[9]

$$\frac{p(N_D^+ + p)}{N_A - N_D^+ - p} = \frac{N_V}{g}\exp\left(\frac{-(E_A - E_V)}{kT}\right).$$

Substituting the expression for N_V and defining an acceptor activation energy $E_a = E_A - E_V$ gives

the expression

$$\frac{p(N_D^+ + p)}{N_A - N_D^+ - p} = \frac{2}{g}\left(\frac{2\pi m_0 m_h^* \, kT}{h}\right)^{3/2} \exp\left(\frac{-E_a}{kT}\right).$$

(6)

which can be solved for the hole concentration

$$p = \frac{-(N_D + x) + \sqrt{(N_D + x)^2 + 4(N_A - N_D)x}}{2}, \text{ where}$$

(7)

$$x = \frac{N_V}{g}\exp\left(\frac{-E_a}{kT}\right).$$

At high enough temperatures, the compensating donors are essentially all ionized and $N_D^+ \approx N_D$.

3. MOBILITY OF CHARGE CARRIERS

Transport in semiconductors is affected not only by the number of carriers but by their

mobility μ. The mobility is the drift velocity of carriers in unit electric field and is related to the

relaxation time τ by $\mu = e\tau / m_c^*$. As mentioned above, the effective mass is used to account for

mobility anisotropy along different parts of the Fermi surface. A measurement of the temperature

dependence of the mobility can provide insight into the nature of scattering processes in a material

since it is related to the relaxation time. (See for example, Ioffe.[10]) The net mobility observed

when several scattering mechanisms are present is given by $\mu^{-1} = \sum_i \mu_i^{-1}$. The dominant scattering

mechanism observed is dependent on the detailed characteristics of the sample and the temperature

region of the measurement.

4. TEMPERATURE DEPENDENT RESISTIVITY FOR LIGHTLY DOPED SEMICONDUCTORS

The temperature dependence of the resistivity for a lightly doped semiconductor will exhibit several temperature regions in which different conduction mechanisms dominate. The most general behavior is discussed by Shklovskii and Efros[11] and is shown schematically in Figure 2. Region A corresponds to intrinsic conduction at high temperatures where carriers are thermally excited across the bandgap. Regions B through D correspond to extrinsic conduction mechanisms. Region B exists if impurities are present which have an ionization energy much less than the gap. It is called the *saturation range* because the carrier concentration is essentially independent of temperature since all the impurities are ionized. The resistivity is therefore determined by the mobility, which increases on cooling due to weaker phonon scattering. The resistivity rises upon cooling through region C as carriers are frozen out. At low temperatures, conduction occurs via hopping directly between localized impurity states. The conductivity for regions C through D is often represented by the sum of three activated terms
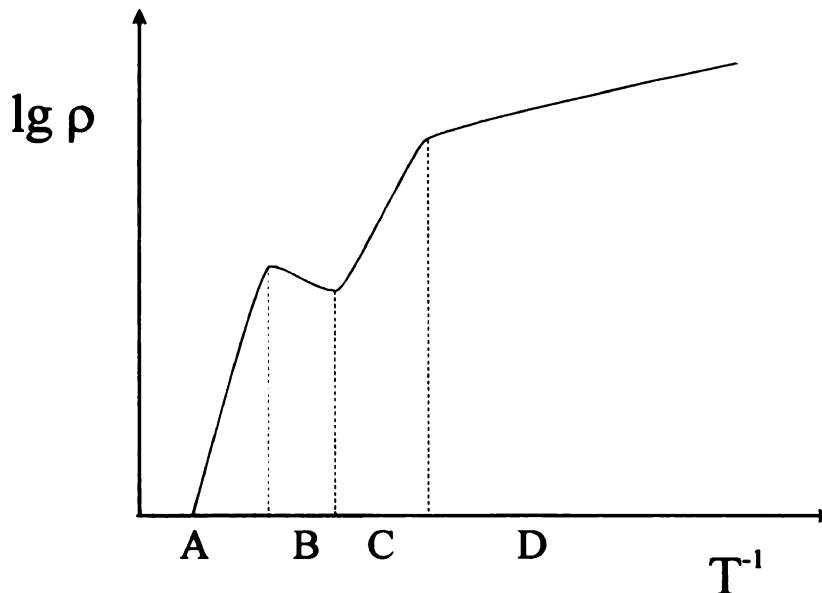
Figure 2 Schematic resistivity temperature dependence of a lightly doped semiconductor showing regions where different conduction mechanisms dominate.[11]

$$\sigma = \sigma_1 \exp\left(-\frac{E_1}{kT}\right) + \sigma_2 \exp\left(-\frac{E_2}{kT}\right) + \sigma_3 \exp\left(-\frac{E_3}{kT}\right). \tag{8}$$

The first term corresponds to region C and E_1 is approximately the impurity ionization energy. The third term corresponds to region D, so long as nearest neighbor hopping dominates, and $E_3 < E_1$. If hopping at low temperature is of the variable range type, then the third term above should be replaced by Mott's law,[12] $\sigma \sim \exp\left(-A/T^{1/4}\right)$, where A is a constant. The second term $\sigma_2 \exp\left(-E_2/kT\right)$ is often neglected, since E_2 is approximately the same as E_1. The E_2 mechanism is believed to be associated with the motion of electrons over singly filled neutral donors, and is only observed when the impurity concentration is high and the compensation is low.

5. ROLE OF STRUCTURAL DEFECTS

Primary defects in crystals can consist of electrons and defect electrons; point imperfections such as vacancies, interstitials, or chemical impurities; dislocations; two-dimensional imperfections such as grain boundaries, twin boundaries, or phase boundaries; and three-dimensional imperfections like voids or impurity clusters. The electronic effects of these defects in semiconductors are discussed in detail by Mataré.[13] The defects of concern in diamond studies are those which are related to structural imperfections.

Prominent electronic effects can occur for defects which significantly disrupt lattice continuity, such as grain boundaries and dislocations. These defects frequently introduce large levels of strain as well as dangling bonds which can trap charge carriers or chemical impurities. Twin boundaries, on the other hand, do not produce free bonds, but only diagonal atomic displacements and introduce very little strain. They therefore have only a little scattering power in addition to secondary effects related to stress.[13]

A schematic of a grain boundary exhibiting dangling bonds is shown in Figure 3.[14] High angle grain boundaries produce a higher density of dangling bonds than low angle grain boundaries,
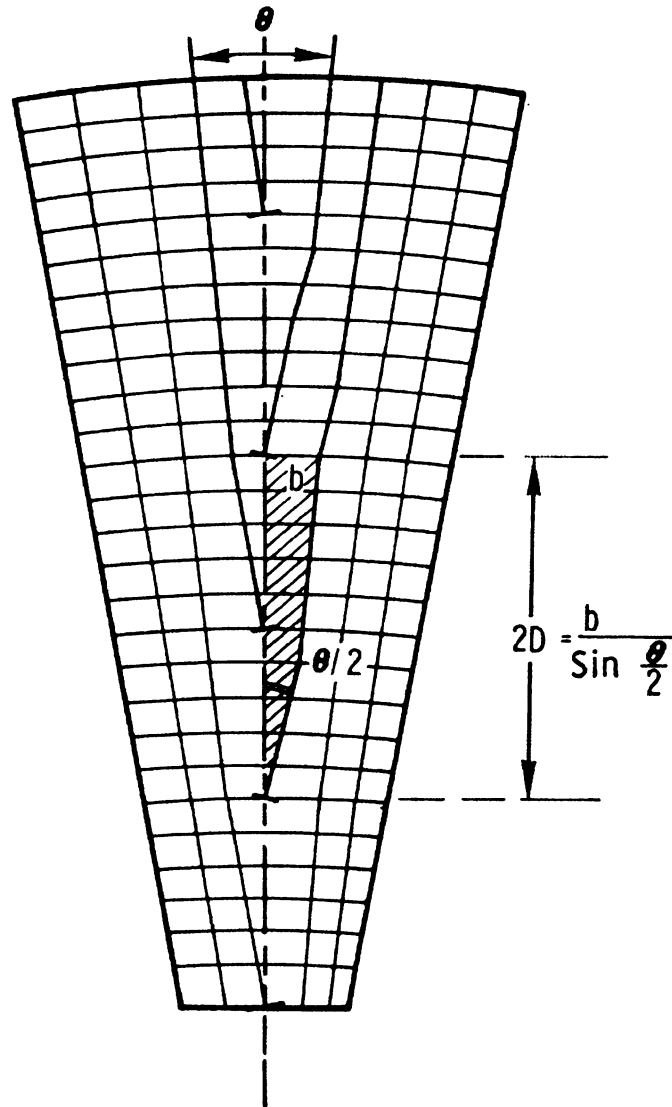
Figure 3 Schematic of a grain boundary of angle θ showing dangling bonds.[14]

as illustrated in Figure 4.[15] In general, such defects with dangling bonds will still appear as coherent structures if the distance between dangling bonds is less than the distance between impurity atoms. Extra states at grain boundaries due to disorder or dangling bonds can deplete nearby crystal regions of charge carriers by trapping. The effect of such space-charge regions can extend several interatomic spacings into the bulk, and can cause anisotropic scattering effects for materials in which the grain boundary defects tend to line up in a single direction.

Models of space-charge effects on transport in poly-Si have been developed by Seager, Pike and co-workers.[16] These models consider trapped charge as creating potential barriers to transverse current flow, as illustrated in Figure 5 for a charged grain boundary in a p-type bicrystal under forward bias.[17] In the diagram U is the applied bias, $e\varsigma$ is the Fermi level (E_F) in the forward biased grain, $e\phi$ is the forward biased barrier, and E_p is the Fermi level in the right grain. The

$$D = \frac{b}{SIN \frac{\phi}{2}}$$

$$D \simeq b$$

$$\theta > 1^0$$

LOW & MEDIUM
ANGLE GRAIN BOUNDARY

$$D = \frac{b}{SIN \frac{\phi}{2}}$$

$$D > b$$

$$\theta < 1^0$$

LINEAGE
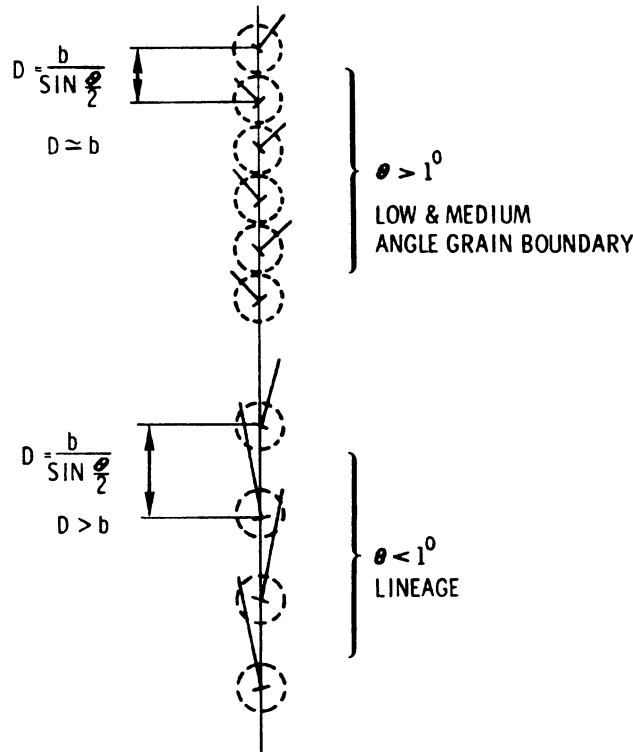
Figure 4 Grain boundaries of low and medium tilt angle θ and the corresponding densities of dangling bonds.[15]
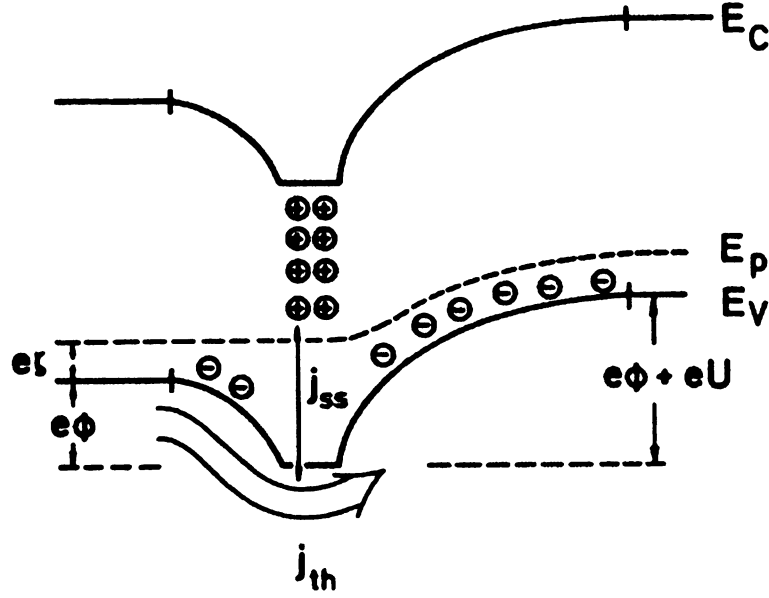
Figure 5 Schematic band diagram for a forward biased charged grain boundary in the "trap transistor model."[17]

positive charge of trapped holes in the grain boundary is compensated by negative acceptors in the space charge region. A majority carrier current j_{th} flows from left to right in the diagram by thermionic emission and a second current j_{ss} exists due to the equilibrium rates of capture and emission of holes from the valence band by states in the grain boundary. For a polycrystalline film of length L and average grain size a, the current due to thermionic emission is given by Werner[17] as

$j_{th} = A^* T^2 \exp(-\beta(\varsigma + \phi))[1 - \exp(-\beta Ua/L)]$, where $\beta = e/kT$, A^* is the effective Richardson constant, and Ua/L is the voltage drop per grain boundary which is presumed small compared to kT. This expression is expanded in terms of the voltage to give a thermally activated conductivity which obeys $\sigma = \dfrac{j_{th}L}{U} = \dfrac{e}{k} A^* Ta \exp[-\beta(\varsigma + \phi)]$. The activation energy $e(\varsigma + \phi)$ is strongly dependent on the doping level.

6. METAL-SEMICONDUCTOR CONTACTS

A. Rectifying Contacts

Metal contacts to a semiconductor can be either Ohmic, rectifying, or in between. When a metal is placed in contact with a semiconductor, the Fermi levels align causing charge carriers to move to alter the potential in each material. The Fermi level of the metal is in its conduction band at the highest occupied state. The energy from E_F to the vacuum level is defined as the metal's work function ϕ_m. For a p-type semiconductor, the Fermi level lies somewhere between the valence and conduction bands, closer to the valence band at temperatures low enough that non-intrinsic conduction by holes dominates. The work function for a semiconductor ϕ_S is defined as the distance from the vacuum level to the bottom of the conduction band. When a metal and p-type semiconductor are placed in contact with no applied voltage, holes flow from the semiconductor into the metal to create a negatively charged region of width W in the semiconductor near the interface. This charged region exists to alter the potential in the semiconductor sufficiently so that the Fermi levels of the two materials align. The semiconductor volume at the interface which is vacated by the holes (majority carriers) is called a "depletion region" or a "space-charge region," and the negative charge in this region is due to minority carriers and ionized acceptors. The change in potential caused by the space-charge region bends the bands in the semiconductor as shown in Figure 6a,[18] creating a potential barrier $e\phi_{Bp}$. Band bending in the metal is negligible because of the much higher carrier density. The barrier impedes hole transport from the semiconductor into the metal, though holes can flow freely from the metal into the semiconductor. Electrons (minority carriers) can flow freely down the potential drop from the semiconductor into the metal, but electrons flowing from the metal into the semiconductor must overcome the potential barrier $(E_C - E_F)$ to enter the conduction band of the semiconductor. At zero applied voltage, the system will be at equilibrium and the net current will be zero across the junction.

If a bias, V_F or V_R, is applied across the junction via Ohmic contacts to the metal and semiconductor, the semiconductor bands will shift down or up in energy relative to the metal as shown in Figure 6b and Figure 6c for forward and reverse bias, respectively. A metal-to-p-type junction is forward biased when the semiconductor is positively biased relative to the metal. When forward biased, the barrier for p-region holes and metal electrons is decreased by the bias voltage, and the majority carrier current in both the metal and semiconductor is increased. When reverse biased, the barrier for p-region holes and metal-region electrons is increased, reducing the majority carrier currents in both materials. The minority carrier currents in each material are unaffected by either forward or reverse bias since the p-region electrons and metal-region holes always see a negative potential barrier at the interface. Contacts which behave as just described are called Schottky diodes and exhibit non-linear I-V characteristics as shown in Figure 7 for an ideal diode, where positive voltage represents forward bias. The I-V behavior for $V \gg kT/q$ is described by the current density J for an ideal forward-biased metal-semiconductor contact[19]

$$J = J_S [\exp(qV/nkT) - 1] \qquad (9)$$

where n is the "ideality factor" given by $n \equiv (q/kT)\partial V/\partial(\ln J)$ and J_S is the saturation current density which depends on the barrier height and the effective mass of the carriers. This expression takes into account both the tunneling current and the thermionic emission current. The barrier height can be determined from the I-V characteristics provided the current density and effective mass are known. For a reverse-biased metal-semiconductor contact, the lowering of the Schottky barrier dominates and the current density is approximately equal to J_S for reversed voltage greater than $3kT/q$. J_S is only weakly dependent on the applied voltage as

$$J_R \cong J_S = A^{**}T^2 \exp\left(\frac{-q\varphi_{Bo}}{kT}\right)\exp\left(+\frac{q\sqrt{q\Lambda/4\pi\varepsilon_s}}{kT}\right) \qquad (10)$$

a. Zero bias
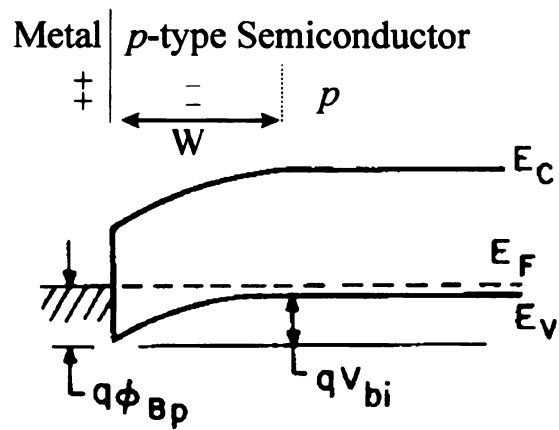
b. Forward bias V_F
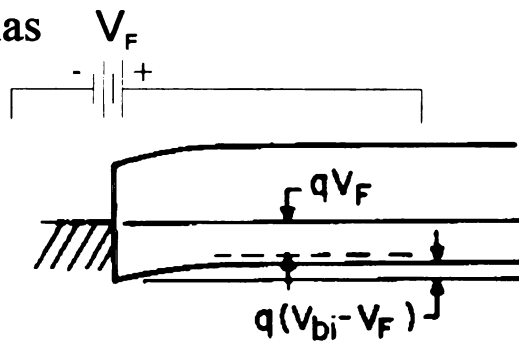
c. Reverse bias V_R
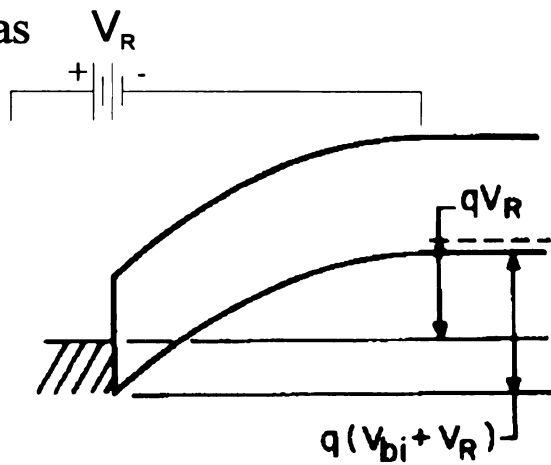
Figure 6 Schematic band diagram for a metal-to-p-type semiconductor contact showing band bending in the semiconductor.[18]
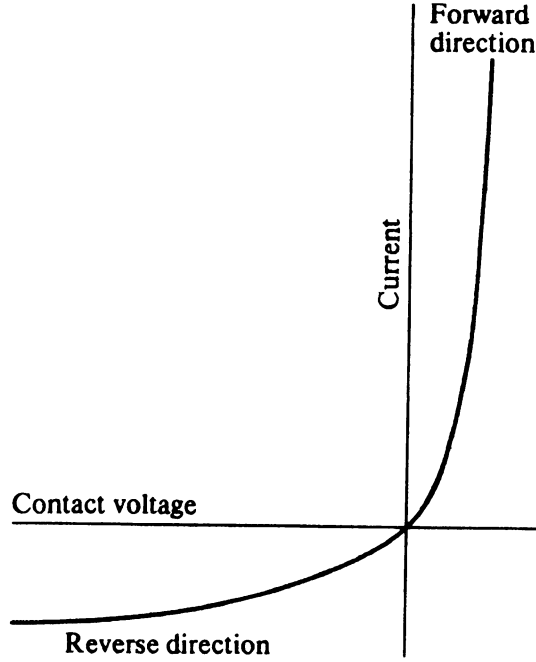
Figure 7 I-V characteristics for an ideal Schottky contact.[20]

where A^{**} is the effective Richardson constant, φ_{Bo} is the zero-field asymptotic barrier height, and

$$\Lambda = \sqrt{\frac{2qN_D}{\varepsilon_s}\left(V + V_{bi} - kT/q\right)}.$$

The reverse bias current density thus depends exponentially on the fourth root of the applied voltage.

B.   Width of Space-charge Layer

The width W of the space-charge region for a metal-to-p-type semiconductor contact, as shown in Figure 6, is obtained by solving Poisson's equation $\nabla^2\phi = -\rho/\varepsilon_s$ in the depletion region $0 \leq x \leq W$ using the abrupt approximation. This approximation assumes that the charge density ρ in the depletion region is approximately the electronic charge q times the ionized acceptor density N_A^-, that the charge is zero outside this region, and that $\partial\phi/\partial x$ is zero for $x > W$. The potential at $x \gg W$ is V_{bi}, where the "built-in potential" V_{bi} is the potential shift required to equalize the Fermi

levels in the metal and semiconductor when their intrinsic Fermi levels are different as shown in Figure 6 above. A more accurate result can be obtained by allowing for the majority-carrier distribution tail by replacing $\rho = qN_A^-$ with $\rho = q[N_A^- + p(x)]$. Solving Laplace's equation with the above boundary conditions gives the width W of the space charge region for a metal-to-p-type semiconductor contact, including the applied bias V, as[2]

$$W = \sqrt{\frac{2\varepsilon_s}{qN_A^-}\left(V_{bi} \mp V - \frac{kT}{q}\right)}$$

(11)

where $\mp V$ is the applied potential for forward/reverse applied bias, q is the electronic charge, and ε_s is the dielectric constant of the semiconductor. The factor kT/q is the correction due to the majority-carrier distribution.[21] N_A^- is strongly temperature dependent according to Equation 4 above. For high temperatures or small activation energy such that $(E_A - E_F) \ll kT$, all acceptors are ionized and $N_A^- \approx N_A$.

C. Ohmic Contacts

An ideal metal-semiconductor contact yields Ohmic behavior when majority carriers provide the charge induced in the semiconductor by aligning the Fermi levels of the metal and semiconductor.[22] Ohmic contacts in the current study are defined as contacts for which the forward and reverse bias current-voltage (I-V) characteristics are linear and symmetrical, as opposed to definitions for device applications which require that the contact resistance is negligible compared to the bulk resistance.[22] For Ohmic contact to a p-type semiconductor, the barrier must be small or narrow enough that holes can easily flow across the junction from the metal to raise the electrostatic potential of the semiconductor relative to the metal. No space-charge region exists in this case since majority carriers are accumulated in the semiconductor, contrary to the case of rectifying

contacts where minority carriers accumulate. Non-linear I-V behavior for a contact arises when carriers must pass a non-negligible barrier either by tunneling or by thermionic emission.

For semiconductors there are essentially four ways to alter the Schottky barrier to produce Ohmic contacts:[23] (1) Match the work function of the contact metal to lower the barrier to a point where thermionic emission of carriers proceeds easily in both directions. (2) Roughen the surface to increase the density of recombination centers at the semiconductor surface so that the surface will act as an sink for majority carriers at the contact. (3) Dope a thin layer at the semiconductor surface with the same type dopant as the bulk semiconductor to narrow the width of the barrier so that carriers can tunnel easily across the barrier. (4) Employ a graded heterojunction to gradually lower the work function across several interfaces in series.

Chapter III

NATURAL AND SYNTHETIC DIAMOND MATERIAL ISSUES

CVD diamond is an inhomogeneous and imperfect material which includes non-diamond phases of carbon, structural defects, and chemical impurities. The inhomogeneities largely determine the observed properties of the material and need to be described prior to discussing their possible effects. The present chapter describes the various stable forms of carbon and their bonding. The classifications of natural diamond are then briefly mentioned and will be referred to throughout the remainder of this work. The focus then falls on the synthesis and morphology of CVD diamond films, especially polycrystalline films, and their known defects. The electronic properties of these defects will be treated in greater detail in the next chapter on the physics of diamond as a semiconductor.

1. CARBON ALLOTROPES

Until 1985, the only two forms of pure ordered carbon thought to exist were diamond and graphite, both of which occur naturally in the earth. Modern technology, however, has provided the means for controlling vapor-phase chemistry under exotic conditions, resulting in the discovery of new allotropes of carbon and new ways of producing known allotropes. The most notable of these advances are the production of diamond films from gas phase precursors using a process known as chemical vapor deposition (CVD) and the discovery and isolation of a new class of closed carbon structures known as the fullerenes. The first isolated fullerene was C_{60}, a soccer ball shaped carbon molecule composed of 60 carbon atoms. These different allotropes of elemental carbon provide a striking example of the role played by bonding in determining material properties.

A.   Bonding in Carbon

Carbon is the sixth element in the periodic table and has four L-shell electrons with which to form bonds. One s-state electron is excited to a p-state so that the electronic distribution changes from $1s^2 2s^2 p^2$ for an isolated carbon atom. For diamond, the outer shell arrangement becomes sp^3 and results in the formation of four tetrahedrally arranged covalent bonds with length 1.54 Å. For graphite, three of the outer shell electrons are arranged as sp^2 and form three co-planar bonds of length 1.415 Å. The fourth electron, however, contributes to both in-plane bonding as well as interplanar bonding, and is sufficiently delocalized enough to contribute to metallic conduction.

The two different kinds of bonding result in very different crystal structures. The sp^3 coordinated carbon forms a diamond lattice as shown in Figure 8,[24] which is a face-centered-cubic (fcc) lattice with a two point basis. The unit cell is shown in Figure 9.[25] One basis point is at 0 and the other is at $(a/4)(\hat{x} + \hat{y} + \hat{z})$, where the edge length a of the cube is 3.567 Å at 0 °C. Each carbon atom is bonded to four nearest neighbors in this structure. The sp^2 coordinated carbon forms
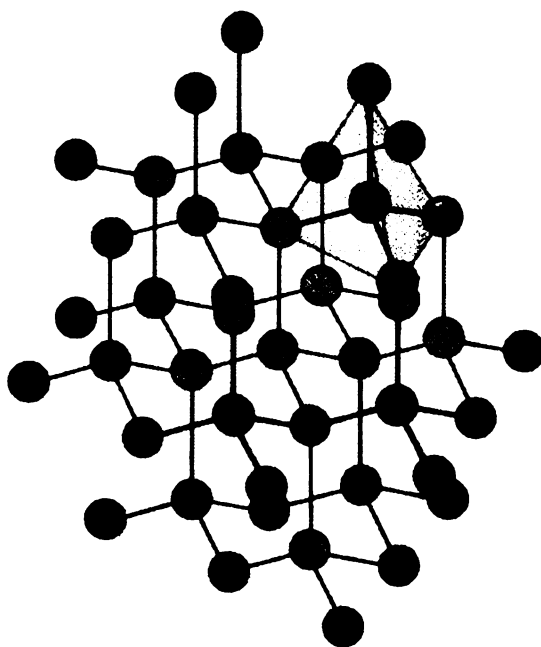
Figure 8   Diamond lattice noting tetrahedrally coordinated bonding for a single carbon atom.[24]
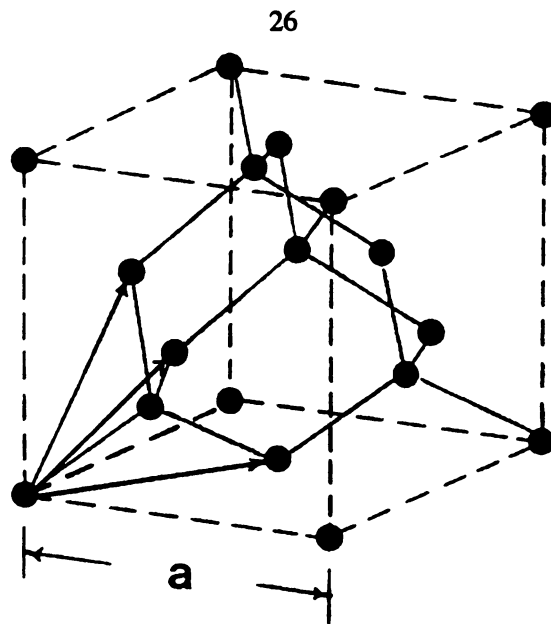
Figure 9 Unit cell for diamond.[25]
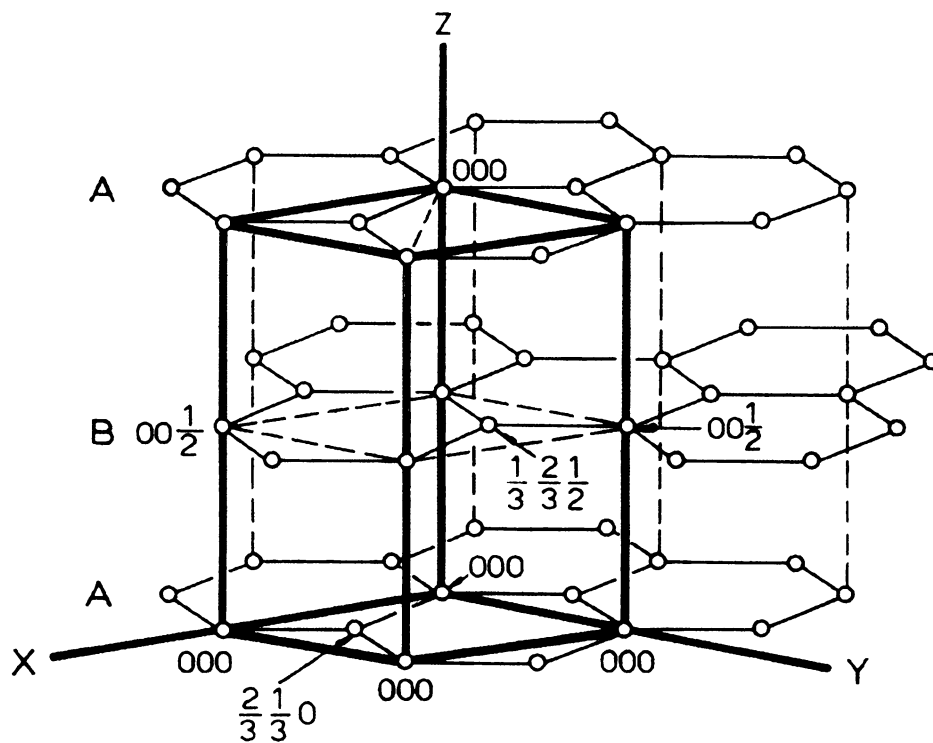
Figure 10 Ideal hexagonal structure of graphite with hexagonal unit cell and crystal axes.[26]

planar sheets of carbon atoms in which each carbon atom is bonded to three other carbon atoms, forming hexagonal rings with interatomic distance of 1.415 Å. The sheets stack on top of each other and are held together by weak intermolecular forces. The material is called a graphite when the sheets show some order in stacking sequence.[26] The interlayer spacing in this case is 3.3539 Å. The ideal hexagonal structure is shown in Figure 10.[26] There also exist several amorphous forms of carbon which are completely either sp^3 or sp^2 coordinated, or are combinations of sp^3 and sp^2 bonded atoms.

It was discovered in 1985[27] that sp^2 carbon can also form various closed structures collectively called "fullerenes" or "fullerites". The name was derived from the resemblance of the C_{60} molecular structure to the geodesic domes of Buckminster Fuller. Many different forms of fullerenes have since been discovered, including C_x, where x = 32, 44, 50, 58, 60, 70, and 120, as well as open-ended and closed-ended nanotubes made from graphite sheets wrapped into cylinders. Figure 11 shows the structure of a C_{60} molecule.[28] The carbon bonds in these structures form networks of hexagons and pentagons. The pentagons slightly distort bond angles from a planar arrangement thereby adding curvature to the graphitic sheets. As determined by Euler's theorem, exactly twelve pentagons are required to close a structure made up of hexagons and pentagons.[29]
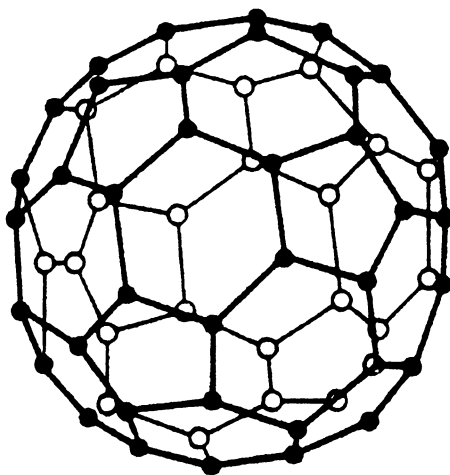
Figure 11 C_{60} molecule.[28]

B. Physical Properties of Different Carbon Allotropes

Of the two infinite network forms of carbon, graphite is the most stable, while diamond is actually a metastable phase. The energy difference between the diamond and graphite structures is small, but there exists a huge energy barrier between them. Transformation of graphite to diamond essentially requires enough energy to break all of the chemical bonds. A phase diagram for carbon was given by Bundy[30] in 1964 and is reproduced in Figure 12. In this diagram the graphite/liquid/vapor triple point is at 0.11 kB and 4,000 K, and the diamond/graphite/liquid triple point is near 130 kB and 4,200 K. Direct transformation of graphite to diamond requires extreme pressures and temperatures. The CVD process allows diamond to form directly from isolated carbon precursors so that the huge energy barrier separating diamond and graphite is avoided from the start. The fullerene molecules are finite structures and do not form spontaneously from the network solids. They are produced only from condensing carbon vapors, which likely explains why they remained undiscovered for so long.

The different allotropes of pure carbon exhibit very different properties. Diamond is a wide bandgap semiconductor, is extremely hard, has a density of 3.53 g/cm^3, and is transparent in the visible part of the spectrum. In contrast, graphite is a semi-metal, shears easily, has a density of 2.25 g/cm^3, and is black in color. The molecular solids formed by fullerenes resemble graphite in bulk appearance.
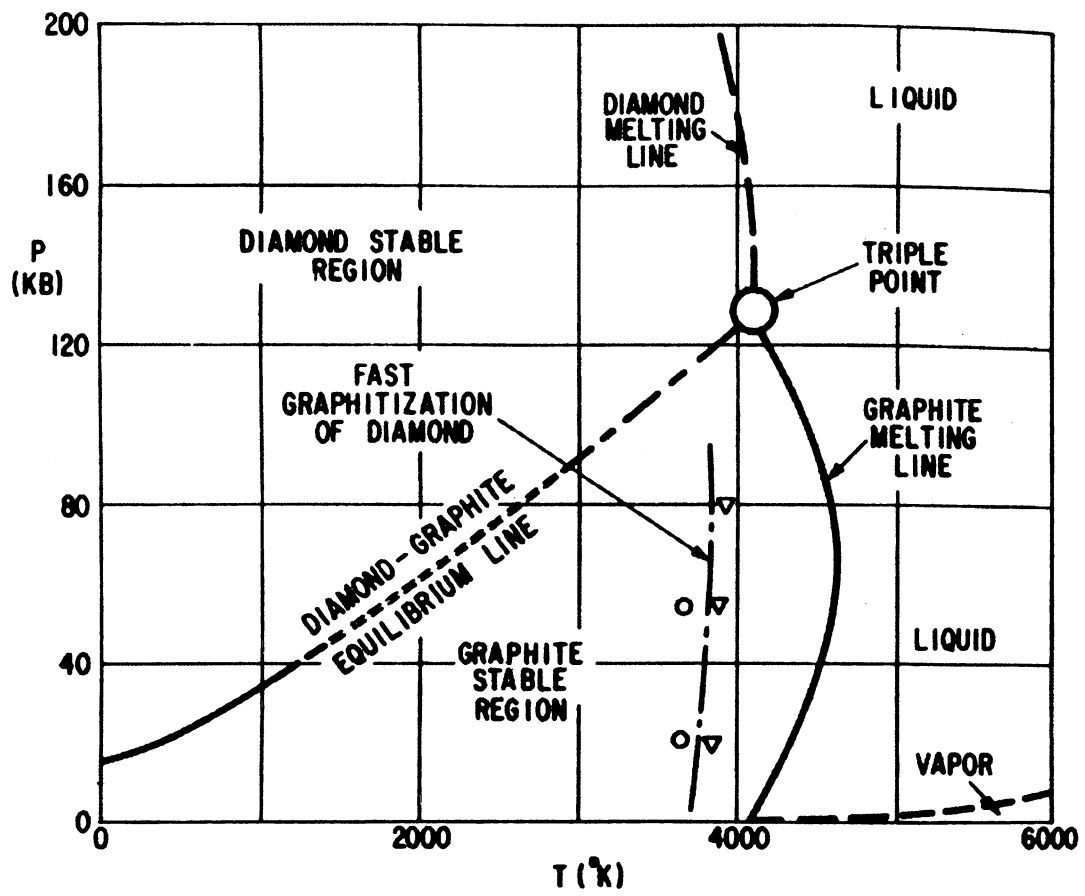
Figure 12 Phase diagram for carbon.[30]

2. CLASSIFICATION OF NATURAL DIAMOND

Natural diamond is formed by crystallization of carbon from solution in molten metals at very high pressure and temperature. Natural diamond is classified as types I, IIa, and IIb according to their absorption spectra, determined by the impurity content. Natural type I diamonds have nitrogen as the primary impurity and are classified by Dyer, *et al.*[31] Type II natural diamonds have boron impurities and were classified by Clark.[32] Type IIa diamonds are transparent and have high resistivity ($\sim 10^{14}$ Ω-cm). Type IIb diamonds typically have boron levels near 10^{16} cm^{-3} (0.5 ppm) which give them a resistivity near 10^8 Ω-cm and a blue color due to increased absorption from orange to near infrared.

3. CVD SYNTHESIS OF SYNTHETIC DIAMOND

Prior to the late 1950's, the only means of synthetically producing diamond was by the brute force technique of using very high pressures and temperatures. In 1991 about 100 tons of diamonds were produced annually by the high pressure technique and were primarily used for abrasives. Between 1950 and 1970 a technique for producing diamond at low pressures gradually emerged from the work of groups in the US and Russia. John Angus at Case Western Reserve University pioneered the US effort and in 1971 was the first to unlock the key to low-pressure diamond deposition by using hydrogen to etch the graphite which is deposited along with diamond. Advances by the Japanese in the early 1970's proved that diamond films could be grown rapidly at sub-atmospheric pressures. By 1985 low-pressure diamond was being researched by many groups and a boom of diamond research had begun. This history is summarized by Geis and Angus.[33]

A. CVD Techniques

The chemical vapor deposition (CVD) process for producing diamond requires a gaseous carbon source such as methane or alcohol, a source of hydrogen, and a method of heating these

gases to temperatures near 2,000 °C in close proximity to a substrate capable of supporting diamond nucleation. Such conditions are accessible using a simple acetylene torch. The products of unrefined deposition methods, however, usually contain large amounts of graphitic (sp^2) carbon in addition to diamond-bonded (sp^3) carbon and often show little or no evidence of crystalline diamond growth. A general picture of diamond CVD growth chemistry was presented by Bachmann et al.[34] who consolidated over 80 deposition experiments from over 25 references onto the C-H-O phase diagram shown in Figure 13. Deposition of diamond occurs only within a narrow window of gas ratios, and non-diamond carbon deposition or no deposition occurs outside that region. Hydrogen and oxygen, if used, etch sp^2 carbon faster than sp^3 carbon and are necessary to remove undesirable sp^2 carbon from the film surface during growth. Carbon-rich gas compositions (high methane concentration) deposit carbon faster, but have reduced sp^2 etching and, hence, a higher graphitic component. Carbon-poor gas compositions allow increased sp^2 etching and, hence, a lower graphitic component and a lower growth rate.

An excellent overview of current deposition techniques and understanding of CVD diamond growth is given by Plano.[35] The most common reactors currently in use are microwave plasma, hot filament, plasma torch, and combustion flame. The plasma torch and combustion flame techniques produce very high growth rates, but low film quality in terms of local uniformity and graphitic carbon content. These techniques also require very high gas flows and have small growth areas 1-2 cm in diameter. They are not popular for producing electronic quality material at this time. The hot filament and microwave plasma CVD techniques, however, are commonly used to produce electronic quality diamond films and are more relevant to this study.

In a hot filament diamond CVD reactor, a filament is located approximately 1 cm above the substrate and is resistively heated above 1,900 °C to thermally dissociate feed gases. This provides the radicals, such as atomic hydrogen, necessary for diamond growth. Feed gases consist of molecular hydrogen and a carbon source gas, typically methane (CH_4), in approximately a 100 to 1
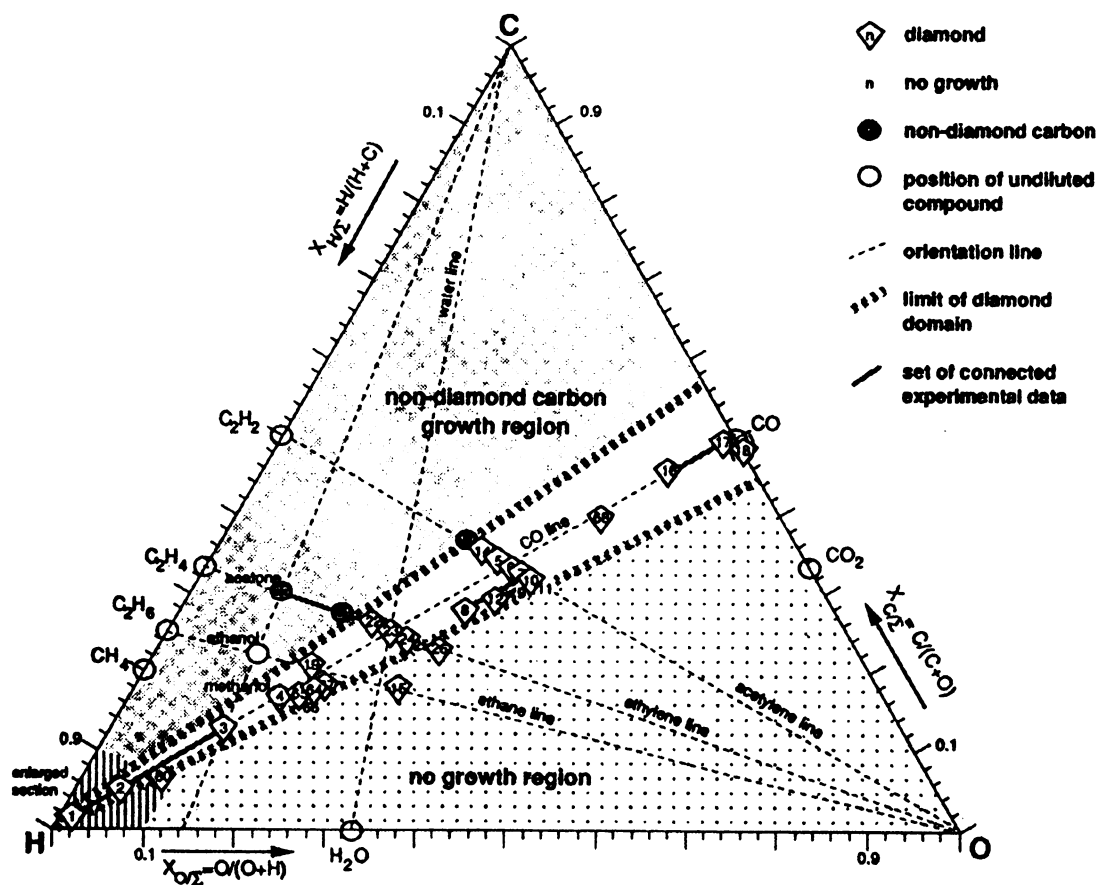
Figure 13 C-H-O diagram for CVD diamond growth.[34]

ratio, respectively. Small amounts of oxygen may also be added. Pressures are typically less than 100 torr. Hot filament CVD has the advantages of lower gas flow rates (~100 sccm total flow), deposition area in excess of 5 cm diameter, and low setup cost. Its disadvantages are that growth rates are slow, typically less than 1 μm/hr, and filaments sag and change shape during their lifetime, causing nonuniform growth conditions. The W, Rh, or Ta filaments also contaminate deposited material.

In microwave plasma assisted diamond deposition the energy required to dissociate feed gases into radicals is provided by a strong, time-varying electric field. This has the advantage that substrate and gas temperatures can be lower than for other techniques because the radicals are ionized by high-energy electrons rather than by direct thermal dissociation. Gas pressures are typically 5 to 90 torr and gas flow rates are low.[36] The deposition rate is highest near the center of the plasma (2-5 μm/hr) and drops off quickly with increasing radial distance. For the 2.45 GHz reactors commercially available the dependable growth region is only a few centimeters in diameter.[35]

B. Doping Techniques

CVD diamond can be intentionally doped by in situ techniques, ion implantation, and diffusion. The only electrically active dopant known for diamond at this time is boron, which acts as an acceptor. In situ doping is accomplished either by adding dopant gases such as diborane (B_2H_6) to the feed gases or by placing solid dopant sources, such as boron powder or B_2O_3, in the chamber to be etched by the plasma. Adding dopants to the feed gases well upstream of the growth region likely produces more uniform doping across a film.[35] Ion-implantation is used to dope natural diamonds and can be used to enhance doping in localized regions to produce Ohmic contacts.[37] Doping by diffusion is slow because high vacancy formation energy and migration

energy result in a large diffusion activation energy of 4.2 eV experimentally and greater than 5.4 eV theoretically.[38] The electrical effects of boron and other impurities are discussed in Chapter IV.

C.   Substrates

Diamond has been grown on diamond substrates (homoepitaxy) as well as several non-diamond substrates (heteroepitaxy) such as Si, β-SiC, nickel, and sapphire.[39]   Non-diamond substrates with low intrinsic nucleation density are treated to enhance nucleation density, usually by abrasion or seeding with diamond powder. Films produced on diamond substrates have perfect registry with the substrate, but films produced on non-diamond substrates are polycrystalline to date. There has been one claim of local heteroepitaxial (100) and (111) diamond growth on silicon (100).[40]   The inability to produce large area single crystal diamond films on economical non-diamond substrates is one of several major problems limiting the development of diamond for microelectronic applications and much effort is directed towards solving it. A surprising step towards this goal is a technique called bias-enhanced nucleation in which a bias of approximately 150 V is applied to the substrate during deposition.[41] The result is large area mosaic diamond films with low angle grain-boundaries ($<$ $\pm5°$ transversal and azimuthal rotation) on non-diamond substrates. The bias is believed to promote subplantation of carbon at the film surface. Momentum and energy transfer play a primary role in the process with thermodynamic processes contributing as well.[42]

4.   MORPHOLOGY OF CVD DIAMOND FILMS

It is currently possible to grow CVD diamond films in three basic morphologies—homoepitaxial single crystal films, well-faceted randomly-oriented polycrystalline films, and highly oriented mosaic films. The morphology of each is strongly dependent on growth conditions,

with homoepitaxial growth being the most forgiving. Boron doping has been reported to improve the crystal quality of CVD films.[43]

A.   Nucleation and Growth

Individual diamond grains in polycrystalline and highly-oriented films nucleate at isolated centers, grow, and eventually coalesce to form continuous films. One study reported that the volume of isolated crystallites increased as $t^{1.5}$ with time.[44] Under optimum growth conditions for polycrystalline diamond growth on silicon substrates in some reactors, nuclei contain a small amount of sp^2 carbon initially with an increased amount (~30%) incorporated in the film and trapped near the interface during grain coalescence.[45] Little sp^2 carbon is incorporated during subsequent growth. A few nm thick layer of β-SiC has also been observed at the diamond-silicon interface for non-optimal growth conditions.[39,46]

B.   Randomly Oriented Polycrystalline Film Texture

A well-faceted polycrystalline film is shown in Figure 14. Reactor-specific growth conditions can be adjusted to alter the relative growth rates of {111} and {100} planes to produce films which exhibit <111> or <100> texture.[47] Film texture is characterized by a parameter α which is the ratio of growth rates on the {100} and {111} planes, V_{100} and V_{111} respectively, defined by $\alpha = \dfrac{V_{100}}{V_{111}} \sqrt{3}$.[48] The parameter α ranges from 1 to 3 for cubo-octahedral crystal shapes ranging from a perfect cube to a perfect octahedron. A film exhibiting strong {111} faceting will have <100> texture. Texture is dependent only on the relative growth rates of crystal planes and is, therefore, independent of substrate orientation. As growth continues after grain coalescence, some grains overgrow others and a cone-like columnar structure results as shown in Figure 15 for a several hundred micron thick film.[49]
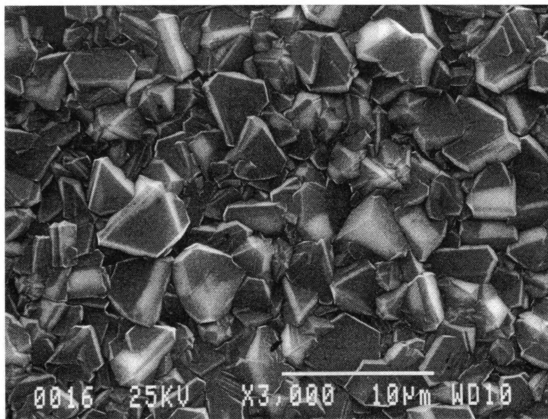
Figure 14 SEM micrograph of a polycrystalline diamond film. (Sample PF, Table 7.)
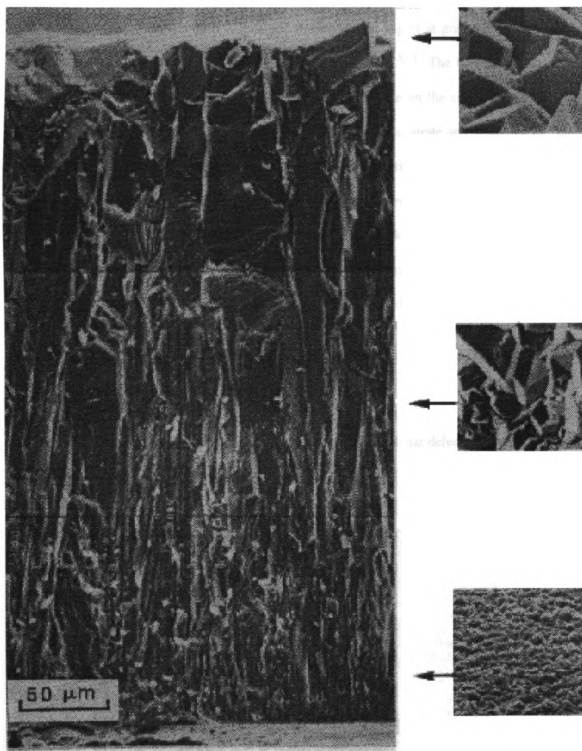
Figure 15 Side-view of thick polycrystalline film showing cone-like grain structure.[49]

C.   Highly Oriented Diamond Films

Polycrystalline films with less than ±5° misorientation angles at grain-boundaries can be grown on Si substrates. The growth process involves three steps.[50,51] The first step is an *in situ* carburization step that creates an epitaxial layer of silicon carbide on the silicon substrate. The second step is a diamond growth step with a bias applied to the substrate and is known as "bias-enhanced nucleation." The bias is believed to result in subplantation of carbon atoms during the initial stages. The third step is a textured growth step which grows out the (100) faces that are parallel to the substrate. The resulting film morphology can look as shown in Figure 16 which shows a thin layer of B-doped diamond grown homoepitaxially on an undoped, highly oriented polycrystalline film that was grown on a Si substrate.[52] The film exhibits strong (100) facets which are aligned to within a few degrees.

D.   Defects

CVD diamond can contain a variety of defects including planar defects, linear defects, and point defects. Prevalence of these defects are reviewed by Zhu[53] of which a brief summary is given

Figure 16 Homoepitaxial layer of B-doped diamond grown on an undoped highly oriented diamond film.[52]

here. Planar defects include stacking faults and microtwins. Stacking faults are commonly a 60°
rotation of adjacent layers about an axis perpendicular to {111} planes. Microtwins are common
within single grains,[39] with multiple macroscopic twinning giving rise to particles shaped as
decahedrons and icosahedrons.[54] Figure 17 shows an icosahedral particle and Figure 18 shows a
heavily twinned particle with 5-fold symmetry characteristic of decahedral particles. Particles such
as these grow from multiply-twinned nucleation sites such as shown in Figure 19. Linear defects
are usually dislocations with axis aligned along the <110> direction on the {100} close-packed
planes. Most dislocations are either 60° dislocations or screw-type. Dislocations are of concern
because they are sources of dangling bonds which can be responsible for dramatic electrical effects.
Twins, stacking faults, and dislocations are found inside grains, in bands within grains, and at grain
boundaries, and their densities are sensitive to deposition conditions.[53] Gross defects in diamond
films, such as grain boundaries, can be delineated using oxidative etch techniques which
preferentially attack graphitic carbon.[55]
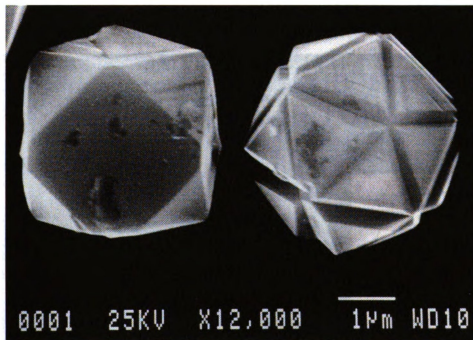
Figure 17 Single crystal next to twinned crystal of icosahedral shape.
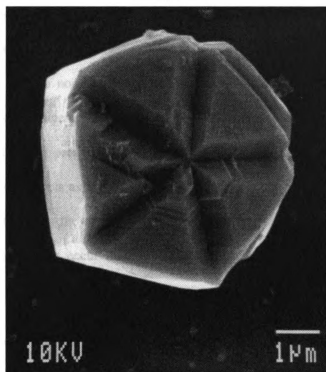
Figure 18 Heavily twinned crystallite exhibiting 5-fold symmetry.
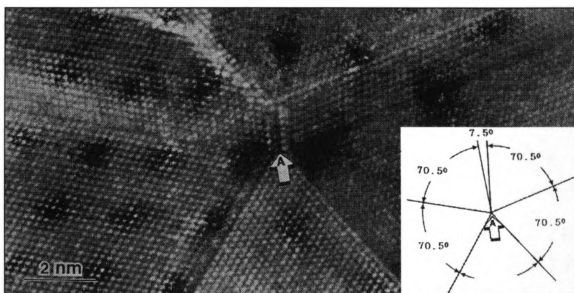
Figure 19 TEM micrograph of a multiply-twinned diamond crystal.[56]

Point defects in diamond include foreign substitutional atoms, self-interstitial atoms, foreign interstitial atoms, and vacancies. These are shown schematically in Figure 20.[53] Substitutional atoms include non-intentional dopants and intentional dopants such as B and N. Hydrogen is the most prominent interstitial impurity in CVD diamond with 5-4,000 ppm levels typical, while N is the most prominent in natural diamond. Other important impurities in CVD diamond include Si with levels as high as 0.2%, O, and Ti. Si, Ta, W, or Ti impurities originate from non-carbon materials in the deposition chamber, such as substrates, filaments, and support structures. Vacancies mostly occur in proximity with grain boundaries, impurities, and other defects.

5. RAMAN SPECTROSCOPY AS A TECHNIQUE FOR CHARACTERIZING DIAMOND FILM QUALITY

Raman spectroscopy is often used to characterize diamond film quality,[57,58,59] though direct quantitative comparison of spectra from different studies or even different samples is very difficult due to variations in effects such as surface scattering. A high, narrow line at 1332 cm^{-1} is characteristic of the highest energy vibrational mode of diamond and is often quoted as an indication of a high quality diamond film. The width of this line for natural diamond samples is typically around 2 cm^{-1}.[57] The Raman scattering efficiency is 50 times greater for graphitic carbon than sp^3 carbon, and appears as a broad band centered near 1580 cm^{-1}. Raman has also been used to analyze stress in heteroepitaxial CVD films[60] and has been used to correlate internal stress in diamond on Si films with N, Si, and graphitic phase impurities.[60]

Foreign Interstitial Atoms
e.g., H, Li

Self-
Interstitial
I

Vacancy
V

Foreign Substitutional Atoms
e.g., N, P, B
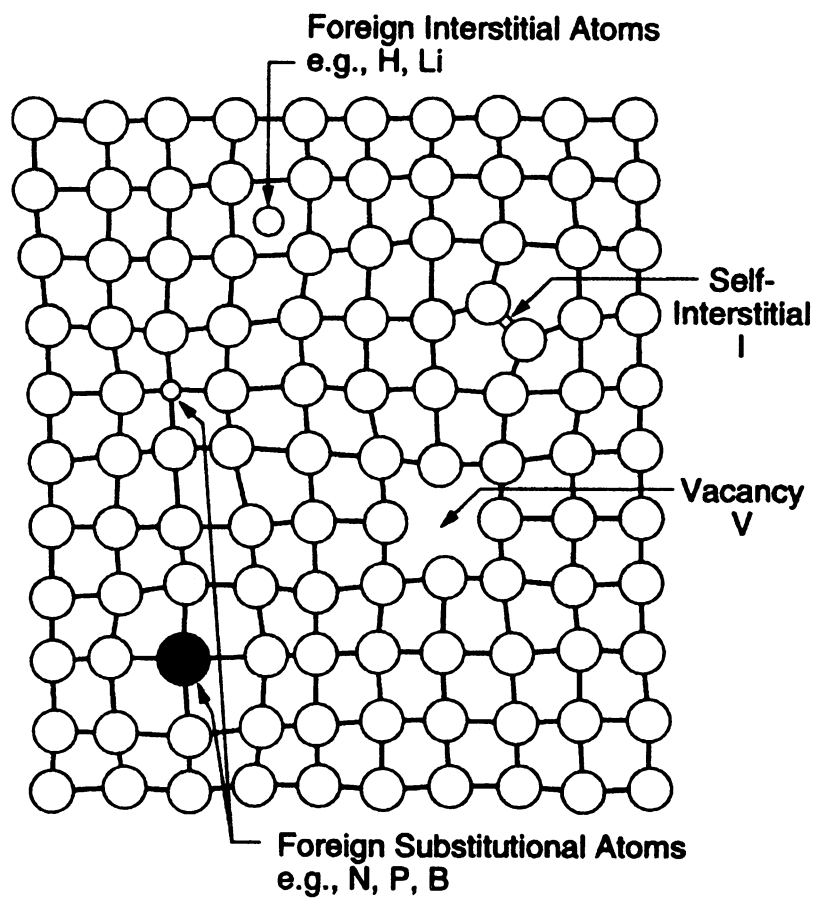
Figure 20 Schematic of point defects in diamond.[53]

Chapter IV

SEMICONDUCTING DIAMOND

The electronic properties of diamond have been studied for many decades, and as a result, much is currently known about the electronic properties of natural single crystal and CVD diamond. This chapter provides the background information necessary to discuss the semiconducting properties of diamond, in general, and introduces the known properties and important issues of doped CVD diamond. The diamond band structure and effective mass of carriers are first described and compared to other group IV elemental solids to emphasize the extreme effects of the C-C bond in diamond. The origin of carriers is then discussed in sections on intrinsic and doped diamond and the reported values for carrier mobilities are reviewed. The electronic transport properties of diamond are then reviewed with emphasis on doped CVD diamond. Studies were excluded which the author believes suffer from insufficient sample characterization or generally terrible quality diamond samples. The chapter concludes by identifying the open questions about the electronic properties of CVD diamond which this thesis attempts to address.

1. BAND STRUCTURE OF DIAMOND

The crystal structure of diamond, which was shown in Figure 8, is also the crystal structure of the group IV elements Si, Ge, and Sn (grey tin). (See Table 1.) The C-C bond length for diamond and the lattice parameter of its fcc structure are given in Table 2 along with the parameter values for Si and Ge, which have the same crystal structure as diamond. The high bond energy and short bond length of diamond are responsible for the large differences in bandgap between diamond and other group IV elements. The Brillouin zone of diamond is shown in Figure 21.[25] The Γ point is $\mathbf{k} = (0,0,0)$ and the X point is $\mathbf{k} = (1,0,0)2\pi/a$. The results of the most recent calculation of the band structure of diamond[25] are presented in Figure 22 along with the band structures of Si and

43

Table 1 Section of the periodic table showing groups III-IV.

III	IV	V	VI
5 **B**	6 **C**	7 **N**	8 **O**
13 **Al**	14 **Si**	15 **P**	16 **S**
31 **Ga**	32 **Ge**	33 **As**	34 **Se**
49 **In**	50 **Sn**	51 **Sb**	52 **Te**
81 **Tl**	82 **Pb**	83 **Bi**	84 **Po**

Ge.[61] The diamond band structure calculation used the Linearized Augmented Plane Wave Method

(LAPW)[62] which uses a muffin-tin approximation for the lattice potential and the Local Density

Approximation (LDA) to approximate the effective exchange-correlation energy. The LAPW

calculation predicts a band gap of 4.15 eV for diamond, which is too small since the LDA

approximation underestimates the fundamental gap. Figure 22 shows that diamond, Si, and Ge all

have four valence bands, three p-like bands and one s-like band. They are also all indirect bandgap

semiconductors since the maximum in their valence bands is in a different location in k-space than

the minima in their conduction bands. The conduction band minimum for diamond is measured to

be at $(0.8,0.0,0.0)2\pi/a$ by neutron diffraction.[63] The measured bandgaps for diamond, Si, and Ge are

also listed in Table 2. The gap for diamond is much larger than the gaps for Si and Ge because the

p-states for diamond are more tightly bound to the nucleus.

Table 2 Selected properties of diamond structure semiconductors.

	Band Gap[64] at 300 K (eV)	Nearest Neighbor Bond Length (Å)	Lattice Parameter[64] at 300 K (Å)	X-X Bond Energy[65] (kJ-mol^{-1})	Thermal Conductivity at 300 K (W-cm^{-1}-°C^{-1})
Diamond	5.47	1.53 [66]	3.56683	347	24-25 [67]
Silicon	1.12	2.35 [68]	5.43095	196	1.5 [64]
Germanium	0.66	2.45 [68]	5.64613	163	0.6 [64]
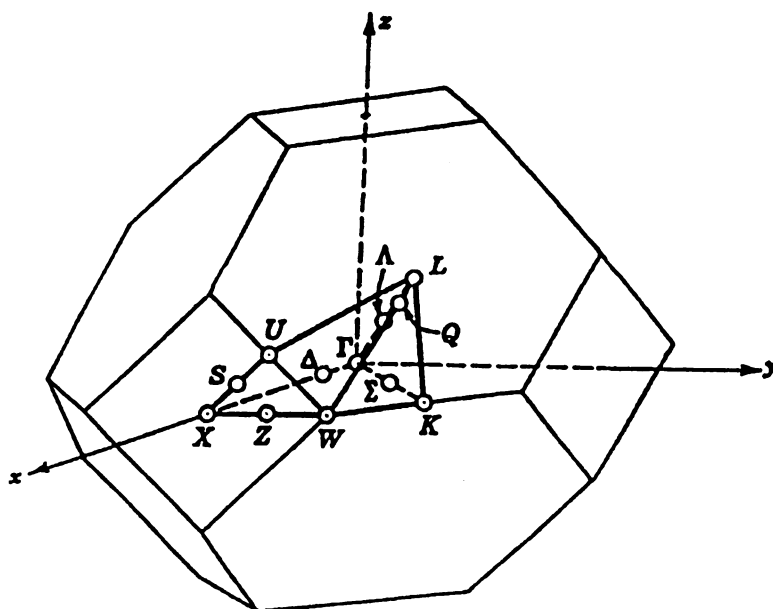
Figure 21 Brillouin zone of diamond.[25]

DIAMOND
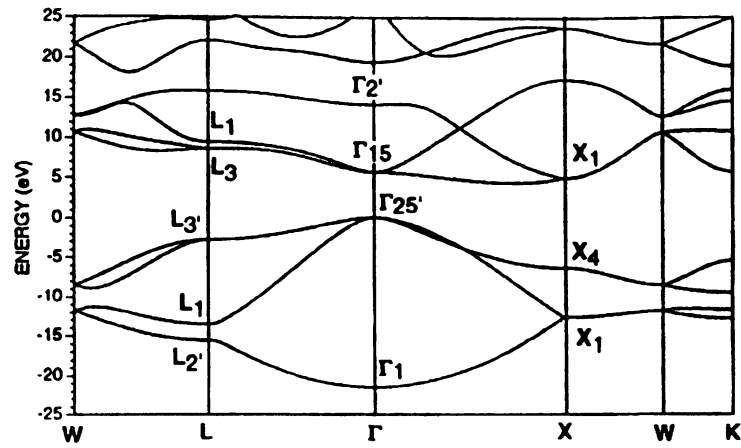
SILICON AND GERMANIUM
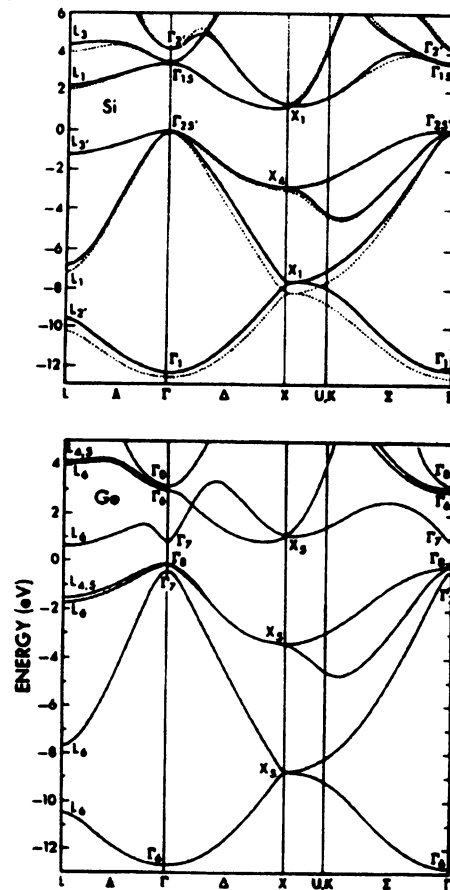
Figure 22 Band structures for diamond,[25] silicon, and germanium.[61]

2. EFFECTIVE MASS OF CARRIERS IN DIAMOND

The values of the hole effective mass for diamond are given in Table 3.[7] There is a significant amount of scatter to the values in the table which includes values from both theory and experiment. The uncertainty in Rauch's values is a factor of 2 and the Reggiani uncertainties are roughly ±10%. The values derived from theoretical calculations by Fong also underestimated the band gap of diamond as 4.15 eV.

The transport properties of electrons in the conduction band of diamond are determined by electrons in the conduction band minima located along the six <100> crystallographic directions. These minima are ellipsoidal in shape, as for silicon, causing the effective mass to have both a longitudinal and transverse effective mass, m_l and m_t, respectively. The conductivity effective mass $m*_c$ accounts for the difference in the mobility and is given by[7] $m_c^{-1} = \frac{1}{3}\left(m_l^{-1} + m_t^{-1} + m_t^{-1}\right)$.

The density of states effective mass for electrons is then given by $m_{dos}^c = (m_l m_t^2)^{1/3}$. Reported values for the electron effective masses are given in Table 4.[7] The conductivity tensor is isotropic

Table 3 Hole effective masses for diamond in units of m_o.[7]

Reference	m_{hh}	m_{lh}	$m*_{dos}$	$m*_c$
Rauch[69] 1962 (exp.)	2.12	0.7	2.38	1.60
Reggiani[70] 1979 (exp.)	1.1	0.3	1.20	0.83
Fong[25] 1993 (theor.)	0.614	0.208	0.69	0.46

Table 4 Electron effective masses for diamond in units of m_o.[7]

Reference	m_l	m_t	$m*_{dos}$	$m*_c$
Nava[71] 1980 (exp.)	1.4	0.36	0.57	0.48
Fong[25] 1993 (theor.)	1.665	0.29	0.52	0.40

and the current and electric field are in the same direction. A parallel discussion of the effects of the ellipsoidal Fermi surfaces for the case of Si is given by Blakemore.[72]

3. DOPED DIAMOND

The earliest experimental investigations of the role of impurities in diamond were performed on natural single crystals. The impurities investigated in diamond so far include B, N, P, Al, and Li. Of these dopants, B, N, and Al occur in natural diamond at appreciable levels. In other studies dopants may be incorporated by ion implantation or diffusion methods. Other group III and group V elements such as Ga, In, As, and Sb are generally present below 5×10^{-4} ppm.[73] The tetrahedral radius of a carbon atom is 0.77 Å which is too small to accommodate dopant species larger than N without significantly distorting the lattice.[53] The current belief supported by experimental evidence is, therefore, that only B and N form substitutional dopants in diamond.[53] Li goes into diamond interstitially and has too high of a diffusivity in the diamond lattice to be a useful dopant. The formation energies of several dopants are given by Kajihara et al.[74]

A. Boron

The B acceptor species activation energy was first measured by Collins and Williams in natural diamonds to be 0.3685 eV.[9] Diamond usually contains compensating species to varying degrees dependent on material characteristics. B is the major impurity in type II diamonds, with the higher resistivity of IIa diamonds ($\sim 10^{14}$ Ω-cm) caused by higher compensation than IIb diamonds ($\sim 10^{8}$ Ω-cm). The B impurity level broadens significantly with increased doping, with states lying above the valence band by as little as 0.002 eV at $\sim 10^{20}$ cm^{-3}.[75,76,77] The Bohr radius of the ground state of the B doping impurity is approximately 3.5 Å, which is very small and prevents sufficient wave function overlap necessary for metallic conduction until above $\sim 10^{20}$ cm^{-3} levels.[78]

B.   Nitrogen

Nitrogen goes into diamond substitutionally and has been associated with a donor level 1.7 eV below the conduction band minimum.[79] This level is too deep in the gap to effect useful n-type doping at moderate temperatures. Nitrogen is the major impurity in type I diamonds and is present in CVD diamond as either an unintentional contaminant or as an intentional dopant species.

C.   Defects in Diamond as Donors and Acceptors

Defects other than intentional dopants can also act to change the population of charge carriers. Disrupted bonds can have either positive or negative core charge and act as donors, acceptors, or carrier traps, depending on the circumstances. They can act as compensating sources or as sources of majority carriers, and sometimes both at the same time within a single material. Dangling bonds at line and surface defects can be particularly influential in depleting nearby areas of carriers to create space-charge regions. These effects are particularly important in determining the transport properties of diamond, and will be discussed in greater detail below with respect to particular defects or conductivity effects in diamond.

4.   MOBILITY IN DIAMOND

An excellent review of scattering mechanisms observed in diamond is given by Han[7] along with the expected mobility temperature dependence for each. Acoustic phonon scattering can be very important in type IIb and IIa natural diamonds giving the electron or hole mobility proportional to $T^{-3/2}$. Ionized impurity scattering can be observed in IIb diamonds and synthetic diamonds and results in a mobility proportional to $T^{+3/2}$. The room temperature carrier mobilities for natural diamond single crystals are listed in Table 5[7] along with the carrier mobilities for Si, GaAs, and several wide bandgap semiconductors for comparison. The high carrier mobility of diamond is

Table 5 Room temperature low-field mobility of diamond and several wide bandgap semiconductors.[7]

Material	Electron Mobility $(cm^2/V-s)$	Hole Mobility $(cm^2/V-s)$
diamond (avg. of literature values)	2150 ± 200	1700 ± 280
Si	1400	600
GaAs	8500	400
GaN	400	
α-SiC	600	40
β-SiC	1000	40

related to its high Debye temperature ($\theta_{Debye} \sim 2,000$ K) and stiffness compared to other wide bandgap materials ($\theta_{Debye} \sim 1,000$ K for SiC[80]).

5. TRANSPORT IN DIAMOND

Carrier densities in single-crystal diamond are dependent on dopant levels as determined by the general principles of semiconductor statistics in Chapter II above. However, the *measured* transport properties of a diamond sample are also strongly affected by surface properties, defects, and electrical contacts. This section surveys current knowledge of transport in diamond and the effects of these other considerations.

A.   Comment on Comparing Published Results

Caution must be exercised when comparing reports of transport effects in diamond films, especially polycrystalline diamond films, due to lack of standardized procedures for preparing and characterizing material. A special session at the 1995 Applied Diamond Conference held at the National Institute of Standards (NIST) in Gaithersburg, Maryland, addressed this problem as it applies to thermal conductivity measurements. Electrical transport is significantly dependent on

effects associated with defect levels, electrical contacts, annealing, surface treatments prior to measurement, film thickness, grain size, doping level, compensation level, etc., which typically vary widely from study to study. Studies should ideally include characterization of all of these details and standards should be established for comparison, though the resources of individual research groups and the brevity of published journal articles is rarely accommodating in this regard. The one glimmer of hope is that reported results appear to be more consistent as film quality generally improves in terms of lower graphitic content. A list of characterization techniques and the optimal results for evaluating film quality is given by Plano.[35]

B.   Conduction Mechanisms in Boron-Doped Single-Crystal Diamond

A general picture of electronic transport in single crystal boron-doped diamond has emerged in which valence band conduction dominates at high temperatures and variable-range hopping conduction dominates at low temperatures. In general, the over-all conductivity σ is often modeled by a sum of three activated terms[81]

$$\sigma = \sigma_1 e^{-E_1/kT} + \sigma_2 e^{-E_2/kT} + \sigma_3 e^{-E_3/kT} \qquad (12)$$

The first term represents activated valence band conduction with the activation energy E_1 roughly equal to the acceptor ionization energy E_a. The second term represents conduction within a band formed by the interaction of closely spaced acceptors which lies between the normal band of acceptors and the valence band, and is known as impurity band conduction. Its observation is possible only when the impurity concentration is high and the compensation is very low, and is usually not seen in CVD diamond. The third term represents hopping conduction between nearest neighbor occupied and unoccupied acceptors.

The hopping conductivity is proportional to the probability of a carrier hopping to another site which is the product of a thermally activated term $\exp(-\Delta E/kT)$ and a tunneling term

$\exp(-2\alpha R)$. Here ΔE is the energy difference between two states, α^{-1} is the decay length of the localized wave function, and R is the hopping distance. The conductivity is thus proportional to $\exp[-(\Delta E / kT + 2\alpha R)]$. When $\Delta E / kT \ll 2\alpha R$, the conductivity is a maximum when R is a minimum and nearest-neighbor hopping occurs. This leads to a constant activation energy $\sigma = \sigma_3 \exp(-E_3/kT)$. When $\Delta E / kT \sim 2\alpha R$, the hopping conductivity is a maximum when the sum $\Delta E/kT + 2\alpha R$ is a minimum. This leads to variable range hopping and the hopping conductivity is given by Mott's Law $\sigma = \sigma_0 \exp(-A / T^{1/4})$, where $A \propto N(E_F)^{-1}$.[82]

A cross-over from valence band conduction at high temperatures to variable-range hopping conduction at low temperatures has been reported by Massarani et al.[78] for synthetic boron-doped diamonds and also by Visser et al.[83] for homoepitaxial boron-doped diamond. Both of these studies demonstrated that nearest-neighbor hopping was not a reasonable possibility for a contributing conduction mechanism in their samples at low temperatures. In contrast, Malta et al.[1] showed a transition to nearest-neighbor hopping at low temperatures in homoepitaxial films. The differences in hopping mechanism reported in these studies may be consistent with the expected picture in which lower compensation levels decrease the density of available hopping sites near an occupied acceptor site, and thereby increase the average distance between available hopping sites, shifting the dominant hopping mechanism from variable range to nearest neighbor. Massarani et al. report compensation ratios N_D/N_A over 40% for their samples; Malta et al. report values generally below 20%; and Visser et al. report values less than 0.3%, which seems anomalously small for homoepitaxial films produced by hot-filament CVD.

Hopping is particularly important in a wide bandgap semiconductor with deep impurity states, like diamond, since very few dopants are ionized at room temperature to contribute to valence band conduction, allowing hopping mechanisms to dominate to relatively high temperatures (~ 200 K) compared to smaller gap systems like Ge for which the cross-over temperature is of order

1 K.[78] For diamond, the small Bohr radius of an ionized acceptor means that the impurity band will not broaden sufficiently to produce metallic conduction until $> 10^{20}$ cm^{-3} impurity concentration, so that large impurity concentration ranges may be studied.

C. Surface Effects

Diamond conductivity can be very dependent on its surface properties. Diamond fresh from a reactor is often hydrogen terminated or coated with surface graphite. Landstrass[84] observed increased resistivity of undoped as-deposited films, both polycrystalline and epitaxial on IIa substrates, when annealed in air at temperatures as low as 100 °C. The type IIa homoepitaxial film on type IIa diamond changed from 10^5 Ω-cm as-deposited to greater than 10^{15} Ω-cm with two hours annealing in nitrogen at 750 °C and exhibited trap-limited conduction. The effect was reversible with exposure to hydrogen plasma and so was attributed to passivation of traps by absorbed hydrogen. Albin and Watkins[85] performed a similar study with similar results. These reports did not distinguish between surface and bulk effects, however, but still illustrate how conductivity measurements can be affected by hydrogen. Mackey et al.[86] used polarized light to distinguish between surface and bulk effects in the conductivity of a clean diamond (110) surface exposed to hydrogen or oxygen under UHV conditions. Mackey reports conductivity changes as entirely due to surface effects and measured the surface resistivity of bare (110) diamond ($< 1.7 \times 10^7$ Ω/□) as less than that of fully hydrogenated diamond ($\sim 6.0 \times 10^7$ Ω/□), which is less than that of fully oxidized diamond ($> 10^{12}$ Ω/□). They also noted that adsorbed hydrogen could be removed by annealing in vacuo at 1,273 K or higher. The diamond surface also undergoes a 2x1 surface reconstruction under such conditions. Diamond surfaces can be oxygenated by exposure to an oxygen plasma and by boiling in saturated solution of chromic acid (CrO_3) in sulfuric acid (H_2SO_4), a popular surface graphite etch. The oxygen is stable on the diamond surface even after annealing at 900 °C for one hour.[87] The hydrogenated diamond (111) surface can also exhibit negative

electron affinity (NEA). A review of this interesting surface effect and the other diamond surfaces which exhibit it is given by Pate.[88]

D.   Role of Structural Defects in Diamond

The most important of the lattice defects in diamond are point imperfections and grain boundaries. Many of the point imperfections create high energy optical effects which will not be discussed here. Twin boundaries typically do not produce measurable changes in electronic properties since they do not represent inhomogeneity in bond coordination (ie. sp^2 or sp^3) or chemical species, but their appearance may be associated with other major defects.[13] Grain boundaries, however, can significantly affect carrier transport because they are sources of bonding inhomogeneities such as dangling bonds, impurity segregation, voids, and mixed carbon phases. Grain boundary effects in polycrystalline silicon have been successfully modeled by the "trap transistor model"[89,16] discussed in Chapter II, though the exact role of grain boundaries and other such planar defects in determining diamond transport properties is to date unknown.

There is now strong evidence showing that transport in polycrystalline diamond films is dominated by grain boundary effects. Though many studies casually suggest grain boundary effects as being responsible for their observations, only a few studies demonstrate that this is actually the case. Electrical transport properties have been noted to approach those of natural diamond with increased film thickness as grain size increases,[90] and has been similarly been observed for the thermal conductivity[49] and the luminescence signal.[91] The most significant evidence so far is presented in a series of studies[1,51,92] represented by Malta et al.[1] This study compares the mobility and conductivity of simultaneously grown homoepitaxial, highly oriented, and polycrystalline B-doped films at several doping levels and shows a decrease in the Hall mobility by one to two orders of magnitude for polycrystalline films from that of homoepitaxial films for a given growth run. Highly oriented films also showed a marked decrease in mobility, though not as severe,

suggesting that even low-angle grain boundaries (< 5°) significantly affect transport. No clear mechanism for the reduction in mobility was demonstrated, however, and no correlation was observed with grain-boundary trapping theories developed for silicon and other semiconductors. The Hall mobility data from Malta et al.[1] are reproduced in Figure 23 and the measured doping characteristics are listed in Table 6. For doping levels from roughly 10^{17} cm^{-3} to 10^{18} cm^{-3}, all samples displayed a cross-over from valence band conduction at high temperatures to variable-range hopping at low temperatures, as evidenced by a knee in the resistivity shown in Figure 25 and a corresponding minimum in the hole concentration shown in Figure 24. Polycrystalline films, however, exhibited higher cross-over temperature to hopping conduction and roughly 0.07 eV lower activation energy for valence band conduction than simultaneously grown homoepitaxial films. This was attributed to 3-5 times higher compensation ratios observed for the polycrystalline films, which allows the hopping mechanism to dominate to higher temperatures by effectively reducing the distance between available hopping sites. The higher compensation of polycrystalline films and also a 2-4 times higher observed boron incorporation were speculated to be due to higher impurity incorporation for the (111) facets of the polycrystalline films compared to (100) facets of the homoepitaxial films as well as impurity segregation at grain boundaries and defects. Great care was taken in these studies to eliminate the possibility of spurious results caused by effects due to surface graphite, adsorbed hydrogen, or current leakage through the substrate. These authors have recently reported development of an undisclosed method for controlling the compensation level in their films and have shown an increase in mobility of <110> fiber-textured polycrystalline films from 50 to 70 cm^2/V-s with a decrease in compensation level.[93]
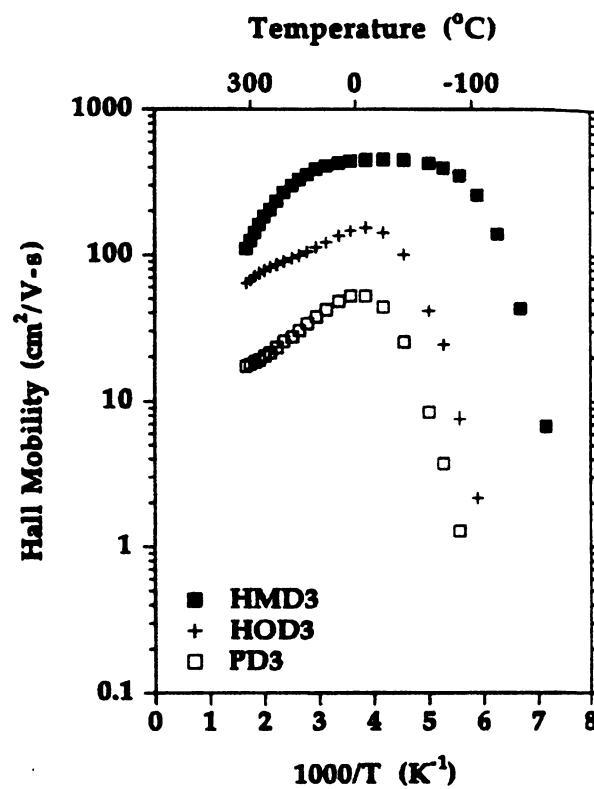
Figure 23 Hall mobility data from Malta *et al.*[1] Samples are listed in Table 6.
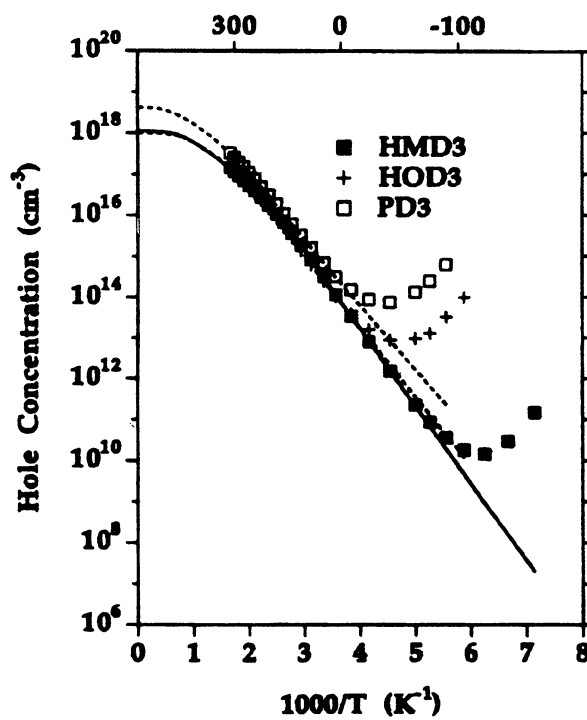
Figure 24 Carrier concentration data from Malta *et al.*[1] Samples are listed in Table 6.
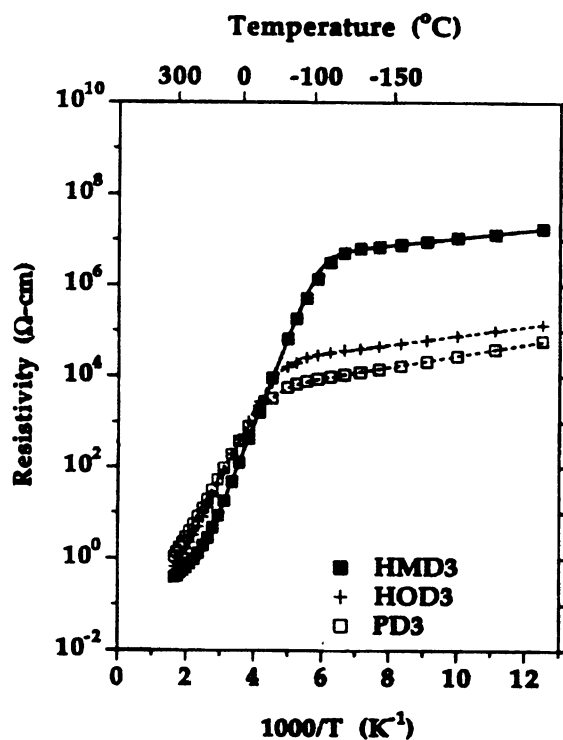
Figure 25 Resistivity data from Malta *et al.*[1] Samples are listed in Table 6.

Table 6 Doping characteristics of simultaneously deposited diamond film samples from Malta *et al.*[1]

Sample	N_B[†] (10^{18} cm^{-3})	N_a[‡] (10^{18} cm^{-3})	N_d[‡] (10^{18} cm^{-3})	k (N_d/N_a)	E_a[‡] (eV)
HMD3 (Homoepitaxial Film)	2	1.1	0.030	0.03	0.351
HOD3 (Highly Oriented Film)	6	1.1	0.15	0.13	0.312
PD3 (Polycrystalline Film)	7	4.8	0.63	0.13	0.285

[†]Measured by secondary ion mass spectrometry (SIMS).

[‡]Obtained from fit to carrier concentration p as in Equation 6. Fits shown in Figure 24.

Further evidence linking grain boundaries to electronic properties was given by Zhang *et al.*,[94] who combined electron energy loss spectroscopy (EELS) with high resolution electron microscopy (HREM) to observe extra states in the bandgap of *undoped* diamond due to grain boundaries. They present evidence for non-tetracoordinated carbon atoms and π-bonding in the grain boundaries. This kind of bonding could be delocalized, but it would depend on the local electronic structure. Their observations also suggest that grain boundary structural differences between diamond and Si cannot be explained by geometrical grain boundary theories, but that they are likely due to differences in bonding nature between diamond and Si.

Han *et al.* [95] used depth resolved Raman spectroscopy to identify regions of high and low defect density on an epitaxial film grown on a IIa diamond for transient photoconductivity measurements. This study observed that the combined electron-hole mobility and carrier lifetime appeared to be unaffected by a large density of line defects in the epilayer, and speculated that the transport properties were dominated by point defects such as impurities. Another study used an electrolytic decoration scheme on *undoped* polycrystalline films and noted electrochemical deposition of silver at grain boundaries, indicating current flow through grain boundaries in the highly resistive films.[96] This study also measured the frequency-dependent conductivity and showed consistency with a model of hopping transport in the 2-dimensional grain boundary paths.

E.   Ohmic Contacts to Diamond

As is typical for metal-semiconductor contacts, direct contact between a clean metal and a clean diamond surface will in general yield a rectifying contact due to the formation of a Schottky barrier at the metal/semiconductor interface. Altering this barrier to produce Ohmic contacts is difficult for wide band-gap semiconductors. It has been the subject of much diamond related research, however, since stable Ohmic contacts play an important role in transport measurements[97] and are crucial for certain device applications, as are high quality Schottky barrier contacts.

The current understanding of Ohmic and rectifying contacts to diamond is reviewed by Tachibana and Glass.[98] In essence, all four methods of reducing barrier effects noted in Chapter II.6 have been attempted for diamond. Attempts to find a metal with a suitable work function to lower the barrier have met with limited success for diamond since the Fermi level appears to be strongly pinned at the diamond surface and depends on the bonding and geometry of the interface, making the barrier height independent of the metal work function.[99,100] Surface roughening by techniques such as mechanical abrasion and Ar-sputtering prior to metallization have produced Ohmic contacts which can be electrically noisy and become unstable at high temperatures as the damage is annealed.[98,101]

Thermally stable Ohmic contacts to diamond have been fabricated by highly doping the surface layer with boron. For natural and CVD diamond this is facilitated by ion-implantation with boron followed by a high temperature anneal (~1,200 °C) and surface graphite etch to remove surface damage caused by the implanting process.[37,102] For CVD materials *in situ* doping can also be used.[103] These highly doped layers are then metallized, usually with a carbide-forming metal such as Ti (20 nm) followed by a protective layer of Au, and then annealed.

A second popular method for forming Ohmic contacts to diamond uses a thermally activated solid state reaction to encourage carbide formation between a carbide forming contact metal and the diamond surface.[104,105,106] In the implantation method above, deposition of about 20 nm of carbide forming metal (Ti, Mo, Ta) is followed by > 100 nm of Au and then annealing at temperatures in excess of 400 °C. Some of the best reported results use annealing temperatures above 600 °C for an hour or more. Over-annealing can reportedly lead to phase separation of the diamond, carbide layer, carbide-forming metal layer, and Au overlayer, so that rectifying characteristics result.[98] The degree to which the contacts are Ohmic and the specific contact resistance are sensitive to the doping level of the diamond and the surface termination (oxygen or hydrogen termination).[107]

Ohmic contact to polycrystalline CVD diamond is generally much easier to achieve and has been effected in numerous reports using carbide-forming-metal/Au contacts as well as bare metals such as Al. This is likely due to a large number of defect states at or near the surface of grain boundaries. It is the opinion of this author that any reported electrical transport measurement on diamond which depends on a claim of Ohmic contacts to *single crystal* natural or homoepitaxial diamond in which either a solid state reaction or ion implantation method such as described above was NOT used, should be viewed as suspect. It can often be inferred from such reports that very low-quality diamond material was used (very high graphitic content) or that side effects such as surface conduction through a damaged layer may be present.

6. INTERESTING QUESTIONS

The studies mentioned above clearly point to defects as playing a key role in determining the electronic properties of polycrystalline diamond films. The boundaries between grains misoriented by as little as a few degrees have been linked to significant reduction in carrier mobility, though no working model of the scattering mechanism exists. Trap-transistor models developed to model carrier trapping at grain-boundaries in smaller gap semiconductors like Si, Ge, and GaAs do not seem to apply to doped diamond,[1] and evidence suggests that grain-boundaries in undoped polycrystalline films can even act as low resistance paths for current flow.[96] The development of proper models for defects such as grain-boundaries is further hampered in diamond because details of impurity segregation, amounts of graphitic sp^2 bonded carbon, dopant incorporation, and dangling bonds at grain-boundaries are still unclear. This is partly because of the wide variation in properties of materials studied in the literature. Other questions pertinent to electronic properties are identifying sources of compensation, which are present in all diamond, and finding n-type dopants which are energetically accessible at reasonable temperatures.

The answers to questions regarding electronic properties of defects are strongly dependent on the detailed structure and chemistry of regions such as grain-boundaries, and are therefore likely to be strongly dependent on growth conditions, substrate material, impurities, and pre-measurement treatments. As mentioned earlier, a clear picture of the role of grain-boundaries can only emerge from experiments on samples rigorously characterized at the microscopic level and possessing isolated defect properties. The proper experiments must peer directly into a defect region to link local electrical properties to the local chemistry and structure.

Chapter V

EXPERIMENT

1. CHAPTER OVERVIEW

This chapter presents the details of how samples were grown, electrically contacted, and measured. It begins by describing the substrate preparation for each sample prior to diamond growth. Polycrystalline films, homoepitaxial films, and low nucleation density microcrystallite films were all prepared differently. The growth processes are explained, and the processes for forming electrical contacts to each sample are then described. A significant section is devoted to describing the lithographic process for forming electrical contacts to microcrystallites, since the development of this process was a major technical challenge for this study. The final section of this chapter describes resistivity measurements for all of the samples, and Hall-effect measurements for the large area homoepitaxial and polycrystalline film samples.

2. SUBSTRATE PREPARATION FOR DIAMOND GROWTH

The studied boron-doped diamond samples consisted of a homoepitaxial film, a polycrystalline film, and isolated microcrystal structures, all grown by chemical vapor deposition under identical conditions. The polycrystalline and microcrystal films were grown on p-type silicon wafers with a 4 μm oxide layer. Nucleation on such substrates is inherently very low ($\sim 10^4$ cm^{-2})[108] due to the high surface energy of diamond relative to that of Si,[35] so substrate preparation techniques were used to enhance and control nucleation densities to produce either continuous polycrystalline films or discontinuous films with isolated grain structure densities of order 10^6 cm^{-2}. Diamond nucleation enhancement was accomplished by either direct placement of diamond seeds on the substrate using diamond-seeded photoresist, or by scratch-treatment with diamond powder. Nucleation enhancement was not necessary for homoepitaxial films, though a selected growth

62

region was defined with an SiO_2 mask. The SiO_2 masks were created in a Veeco deposition system by DC sputtering of Si in a partial oxygen atmosphere through a mechanical mask. Chemical vapor deposition of boron-doped diamond on prepared substrates was accomplished by both hot-filament and microwave-plasma techniques. The photoresist seeding method of nucleation was used for all films deposited using the hot filament technique and the scratch-treatment was used for all samples grown by microwave plasma-assisted deposition.

A.   Nucleation by the Diamond-Seeded Photoresist Technique

Diamond-seeded photoresist was prepared in the following way.[108] Ultra pure diamond particles,[109] 0.1 µm in diameter, were baked at 100 °C for 60 minutes in a hot-plate oven to remove adsorbed water. The diamond powder was added to photoresist thinner in a dropper bottle and agitated in an ultrasonic bath for 15 minutes to break up clusters of particles and to distribute particles evenly throughout the thin liquid. A magnetic stir bar 8 x 1.5 mm was added to the dropper bottle and the solution stirred for 15 minutes. Shipley 1813 photoresist was then added to the mixture. Each time the seeded photoresist was used the diamond seeds were redistributed throughout the mixture by a 30 minute ultrasonic agitation, a 10 minute magnetic stir, and a 45 minute rest period which allowed large clumps of diamond seeds to settle to the bottom of the bottle. The seeded photoresist was spin-applied to substrates at 4,000 rpm for 30 seconds. Substrates were then placed in a partially covered petri dish and baked in a 90 °C pre-heated oven for 30 minutes. Though not necessary for samples for this experiment, the photoresist may then be patterned to produce selected regions of diamond nucleation if desired. Preliminary attempts to pattern Hall-bar samples revealed that soft contact masks, such as a photographic film negative, were unsuitable for photolithographic patterning of diamond-seeded photoresist because the diamond seeds impregnate the soft mask, rendering it useless for further exposures. Projection lithography likely produces repeatable results of desired quality. The photoresist is presumably

etched off by the hydrogen plasma during diamond deposition[108] and the seeds grow on the substrate.

Continuous films roughly 2 μm thick were obtained using a seeding mixture of approximately 275.8 mg of dried diamond powder, 5.52 ml of thinner, and 14.48 ml of photoresist prepared as noted above. Very low-nucleation density films were desired, however, to produce isolated diamond grain structures. An initial attempt at a desirable low-nucleation density seeding mixture consisting of 0.890 mg dried diamond powder, 5.2 ml thinner, and 13.6 ml of photoresist produced a nucleation density of approximately 2×10^6 cm^{-2} as observed on a grown diamond film. A lower nucleation density mixture was produced by adding approximately 1 ml of the above solution (after sufficient agitation and stirring) to 5.1 ml of thinner, agitating and stirring, and then adding 13.4 ml of photoresist. This lower seed density mixture produced a nucleation density of 1×10^5 cm^{-2} on grown films, which allowed for sufficient isolation of single and multi-crystallite structures.

B.   Nucleation by Diamond Powder Abrasion Techniques ("Scratch Treatment")

The general technique of scratch-treating silicon substrates to control nucleation densities involves abrading the substrate with micron-sized diamond particles and subsequent debris removal by thorough cleaning with alcohol or acetone. Scratch-treatments are now likely the most popular technique for nucleation enhancement. Sufficient nucleation density to produce continuous thin diamond films has previously been reported using a slurry of 0.18 g of 5-10 μm diamond particles in 20 ml of ethanol.[110] Patterned films can be produced using a protective mask of deposited SiO$_2$ either during abrasion or during diamond growth. In the current experiment, low and high nucleation densities were successfully obtained on oxidized silicon substrates by scratching with 0.1 μm diameter diamond powder by both direct mechanical abrasion and by ultrasonic activation of abrasive diamond particles. Direct mechanical abrasion was accomplished by rubbing substrates

with cotton swabs dipped in diamond powder. Low nucleation densities were difficult to control using this procedure due to the subjective nature of the rubbing process.

Substrates nucleated using the ultrasonic treatment were placed in a slurry of 0.1512 g diamond powder and 10.0 ml isopropyl alcohol and then agitated in an ultrasonic bath for several minutes. Diamond particle debris was then removed by rinsing in a stream of fresh acetone for 60 seconds before ultrasonic scrubbing in fresh acetone for 5 minutes. Substrates were then rinsed again in fresh acetone, isopropyl alcohol, de-ionized water, and blown dry with nitrogen. The assumption in this method is that nucleation density is controlled by varying the time of exposure to the slurry while in the ultrasonic bath. As a point of reference, one substrate treated for 10 minutes in the ultrasonic bath produced a continuous film at 6 μm thickness and another substrate treated similarly for 2 minutes and grown at the same time produced a nearly continuous film. Effects of a 5 minute ultrasonic treatment in slurry on oxidized silicon substrates was not observable either with an optical microscope or an SEM. As reliable, convenient, high quality SiO_2 deposition was not available for creating patterned abrasion masks, the possibility of using patterned PMMA films as protective masks was explored. Preliminary tests indicated that a 2 μm thick PMMA film was robust enough to withstand even 20 minutes in the slurry, with pattern edge deterioration becoming evident at around 30 minutes exposure. PMMA masks were found to be unreliable, however, due to problems with the film cracking off in large plates during the treatment. PMMA adhesion was improved in one test by using an Al under-layer. For this sample, a continuous Al film was first patterned identically to the PMMA mask using a wet-etch in NaOH through the PMMA mask prior to the ultrasonic treatment. It is uncertain whether or not PMMA films can adequately protect the substrate against abrasion in masked-off regions since one of the films for which the protection mask appeared to be intact upon removal from the ultrasonic bath actually produced essentially a continuous film when grown to a thickness of 6 μm. Effects of unwanted nucleation in previously masked regions during debris and mask removal in acetone may be significant. Further tests are

necessary before ruling out the possibility of PMMA masks for ultrasonic abrasion treatment patterning.

C. Nucleation Techniques Compared

Each nucleation technique has advantages and disadvantages for the current study. The *photoresist seeding* technique has the advantages that it can produce isolated crystallite structures with nearly all the same grain size and shape and that the nucleation density is very uniform. Uniform crystallite shapes and sizes are desirable as they reduce the amount of effort required to design custom lithographic contact structures. Crystallite orientations relative to the substrate are random, however. Figure 26 shows an ideal growth morphology of a well-faceted, regularly shaped, desirably oriented crystallite grown on photoresist-seeded substrates in a hot-filament reactor. *Scratch-treatments* have the advantage that nucleation occurs from structures created on the silicon substrate rather than from a diamond seed[111] which may itself be defective from the start. A single crystallite orientation relative to the substrate may dominate if bias-enhanced nucleation is used.[112] Regularly shaped crystallites with top facets parallel to the substrate tend to have a flat plate-like structure as shown in Figure 27. Scratch-treatment nucleation also avoids questions of the contamination effects from photoresist etched during diamond deposition and can be much simpler for nucleating large, unpatterned wafers.
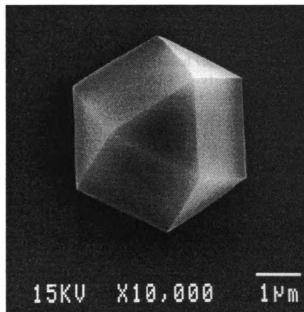
Figure 26 Well-formed microcrystallite by seeded photoresist and hot filament CVD.
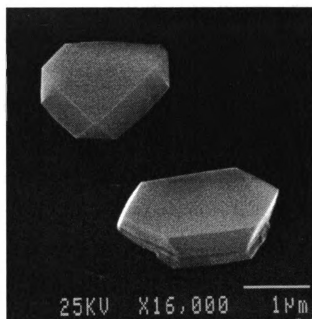
Figure 27 Well-formed microcrystallites by scratch nucleation and microwave plasma CVD viewed 50° from vertical.

3. DIAMOND GROWTH

Boron-doped diamond was grown by chemical vapor deposition on prepared substrates by the author using a hot-filament reactor.[113] Samples were also custom-grown under contract by a microwave plasma-assisted technique at Kobe Steel USA.[114]

A. Hot-filament CVD

In the hot-filament reactor technique, prepared substrates were placed on a Si wafer table about 8 mm beneath a tantalum filament. The filament had several windings of Ta wire which hung by hooks from the top of the vacuum chamber and spanned approximately 12x12 cm^2. It had a resistance of roughly 5 Ω and was operated near 21 A current. Gas flows consisted of 400 sccm H_2 and 4 sccm CH_4 with a total chamber pressure of 50 torr. Filament temperature during diamond deposition was roughly 2,300 °C as measured by an optical pyrometer. The filament did not fill the entire field of view of the optical pyrometer, however, so this measurement was a lower limit of the actual temperature and was only used to provide a rough reference point of filament temperature from run to run. The substrate table temperature was kept near 750 °C during deposition by raising or lowering the filament temperature and was monitored with a thermocouple held in contact with the Si wafer table by the light spring force of its leads. The substrate table temperature was kept below the 1,000 °C decalibration temperature for the thermocouple. Boron-doping was accomplished by placing boron powder into small holes in graphite holders and distributing them around on the substrate table. The heated solid boron sublimes during deposition and is incorporated into the diamond film. Doping levels are controlled only very roughly to high, medium, and low doping by varying the number and placement of the boron holders. Diamond deposition rates in this chamber were typically near 0.25 μm/hr.

Deposition conditions in the hot-filament chamber were not easily repeatable as variables could not be accurately monitored and the characteristics of the apparatus varied with time. Filaments tended to sag unevenly when heated to growth temperatures, creating an uneven heat distribution across the face of the wafer table. Filaments also tended to burn out after roughly six, six-hour deposition runs, then to be replaced by a new filament with a slightly different shape. Thermocouple readings changed by several hundred degrees over their roughly 5 month lifetime in the reactor. Inconsistent contact between the thermocouple and the wafer table, inconsistent aiming of the optical pyrometer, inaccurate optical pyrometer readings, small variation in gas ratios, variable substrate-filament distance, and variable boron-holder placement all contributed to the lack of deposition process control and repeatability. To make matters worse, contaminants such as Ti, Ni, and Cr were likely present in the chamber from growth runs by other researchers interested in non-electronic diamond applications. Contaminants from the Ta filament were also likely present in deposited films, though this was not directly measured. An attempt to minimize these effects consisted of keeping the pyrometer aim, thermocouple contact position on the wafer table, and substrate-filament distance as consistent as possible during the life of a filament. Short growth runs were made to check the facet quality of deposited material for a given set of conditions prior to performing several sequential growth runs for useable material using the same conditions as accurately as possible.

B.   Microwave Plasma Enhanced CVD

Diamond deposition by the microwave plasma technique done by Kobe Steel made use of either scratch nucleated substrates or single-crystal diamond substrates with an SiO_2 mask. Seeded photoresist was avoided to prevent contaminating their well-characterized boron-doped diamond deposition system with photoresist. The available growth area was a relatively small 1x2 cm^2. Boron-doping was accomplished by adding diborane gas (B_2H_6) to the gas stream.[115]

Bias-enhanced nucleation was also used. This system was dedicated to producing boron-doped diamond and produced consistently high quality films with controllable doping levels. Growth parameters can be found in Reference 115.

4. ELECTRICAL CONTACTS TO ISOLATED MICROCRYSTALLITE STRUCTURES—LITHOGRAPHIC CONTACT PROCESS

A. Diamond Crystallite Structures of Interest

The diamond structures of interest to this study are isolated three-dimensional crystallites as shown in Figure 28. Crystallites are well-faceted with generally random location and orientation, though some registry with the substrate may be evident in the bias-enhanced nucleation substrates. Most crystallites exhibit very complicated shapes due to obvious multiple defects such as grain boundaries, twins, and dislocations. Of particular interest are crystallites which appear to be single crystals or which appear to contain a single identifiable defect. Figure 26 showed an SEM micrograph of a nearly ideal micron-sized single crystal and Figure 29 shows a nearly ideal bicrystal. Bicrystals such as this form at random when two crystallites nucleate near enough to each other to coalesce during growth. The resulting grain boundary should be similar to those found between grains in a polycrystalline film since they are generated by the same process. The electronic properties of these microstructures are also to be compared to the properties of homoepitaxial and polycrystalline films.
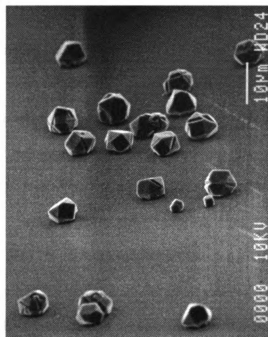
Figure 28 Isolated microcrystallites viewed 50° from vertical.
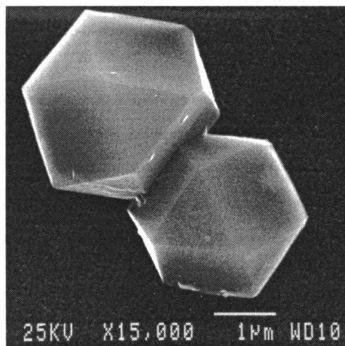
Figure 29 Micron sized bicrystal.

B.   Contact Geometry Considerations

The obvious difficulty in forming electrical contacts to structures such as these microcrystals is that they are too small to allow multiprobe electrical contacts by macroscopic techniques such as wire-bonding, metallic probes, or metallization through mechanical masks. Typical photo-lithographic techniques used are also unsuitable. The general steps in lithography are illustrated in Figure 30. A thin polymer layer known as "resist" is spin-applied to a substrate and cured (Figure 30a). Selected regions of the resist are exposed to a stimulus and thereby chemically altered (Figure 30b). In photolithography the stimulus is UV light and in electron-beam lithography the stimulus is high energy electrons from an electron beam, such as in a scanning electron microscope (SEM). These exposed regions are chemically removed by selective solvents in a process called "developing." (Figure 30c) The remaining resist forms a mask to deposition of metal by processes such as thermal evaporation or sputtering (Figure 30d). The resist mask with its metal overlayer is then chemically removed, or "lifted off." The metal remaining on the substrate forms the desired pattern (Figure 30e). This technology is inherently planar and does not lend itself directly to forming contacts to 3-dimensional structures that are taller than the resist thickness and have steep sides.

Most microcrystals also exhibit significant undercuts as can be seen in Figure 31. These undercuts will cause shadowing during metallization and result in discontinuous electrical leads. Variable crystallite morphologies also demand that a contact technique be flexible enough to accommodate many geometries with a minimum of effort. Conventional photolithography is, therefore, undesirable as it would require that a separate photo mask be processed for each new crystallite shape.

a. Apply resist.

b. Patterned exposure.
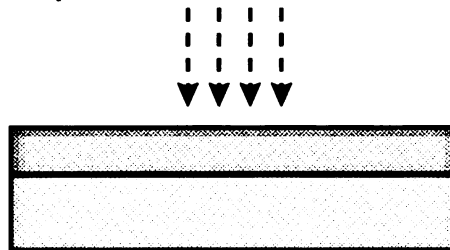
c. Develop.

d. Metallize.
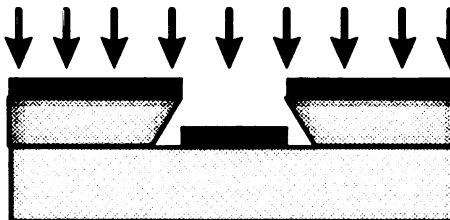
e. Lift-off resist.

Figure 30 Steps in generic lithography.
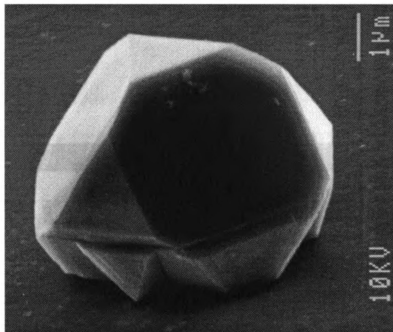
Figure 31 Diamond crystallite with undercut, viewed at 50° from normal incidence.

A process for contacting diamond microcrystals was therefore developed which addresses these concerns. The process involves multiple lithographic steps, a planarization step, and a high temperature anneal. The general concepts of the technique are outlined in Figure 32. Electron-beam lithography is used to create Ti/Au contact pads on the top facets of a crystallite, as shown in Figure 32a. The entire substrate is then annealed at high temperature to effect a solid state reaction between the Ti layer and the carbon in the diamond to create Ohmic contacts.[1,105] A thick layer of polyimide is then spin-applied, partially cured, and back-etched isotropically to produce a planarized surface profile as shown in Figure 32b. Electron-beam lithography is used again to create submicron Au electrical leads, precisely aligned to contact the Ti/Au contact pads, which expand out to form macroscopic regions for wire-lead attachments. Figure 32c and d show the final product from a side view and a top view, respectively.
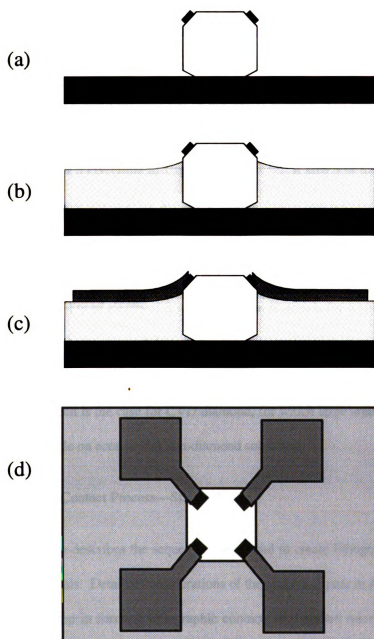
Figure 32 Steps for lithographic contacts to 3D microcrystals.

This scheme for forming electrical contacts to micron-sized crystallite structures solves the problems mentioned above. Electron-beam lithography is employed because it allows precise positioning of submicron contacts and leads onto micron-sized crystal facets and offers the advantage that custom electrode patterns can be easily and quickly designed for each new crystal size and shape. Ohmic contact is restricted to the small area of the annealed Ti/Au contact pads so that the region of the current contacts can be accurately defined. The polyimide layer facilitates use of essentially planar resist technology to form the submicron Au leads which must connect the Ti/Au pads on top of a crystallite to large pads far away. It also acts to bury crystallite undercuts and ensures that contacts and leads avoid the diamond-substrate interface region where additional complications may exist, such as a thin silicon-carbide layer[39,46] or multiple crystallite defects. This technique can be modified slightly to accommodate the chemistry of materials other than diamond to realize the possibility of electrical measurements on materials for which large single crystals are difficult or impossible to grow. Additionally, microdevices which require single crystal materials can be fabricated using microcrystallites, and thereby circumvent the necessity for large area single crystal material. Such is the case for CVD diamond, for which large area single crystal material is currently unattainable on economical non-diamond substrates.

C.   Lithographic Contact Process—Start to Finish

This section describes the sequential steps used to create lithographic contacts to B-doped diamond microcrystals. Detailed considerations of the process appear in Appendix A.

The first step in forming lithographic contacts to diamond microcrystals is to ensure that the diamond surface is free of non-diamond contaminants, including non-diamond carbon phases and metals. An electrochemical etch developed by Marchywka et al.[116] was used to remove surface graphite and to oxygen-terminate the surface to prevent spurious bulk resistivity measurements caused by lower resistivity surface layers.[117] For the etch the sample was mounted in

a teflon holder, centered between two platinum-mesh electrodes and facing the cathode. The etch solution consisted of DI water and enough chromic acid (CrO_3) to produce 100 to 150 mA current at > 150 V dc bias. Electrodes extended about 2 cm below the solution surface and were separated by about 2 cm. Samples were etched in this configuration at 165 V bias for > 10 minutes and then rinsed well in DI. Graphite electrodes were also tried, but they tended to etch quickly and crumble, thereby freeing particulates into the solution. Some of these particulates collected on the sample and were very difficult to remove, even with ultrasonic scrubbing in solvents. Reports of further refinement of the etching technique indicate that addition of chromic acid is not necessary.[117] Following the electrochemical etch, the samples underwent a de-metal etch[118] consisting of 8 parts DI, 2 parts H_2O_2 (30% solution), and 1 part HCl at room temperature for 15 minutes.

The next step was to identify interesting diamond structures on the substrate. Samples were coated with 25 nm of Al, deposited at normal incidence, to act as protection against hydrocarbon contamination, and then observed in a SEM at 25 kV accelerating voltage using about 3 pA beam current. The substrate was oriented in the SEM with a flat edge parallel to the SEM cross-hair lines. Well-faceted crystallites of interest were photographed at roughly 15,000 magnification to record both their detailed structure and orientation and at 100 magnification to record their position on the substrate relative to unique crystallite patterns nearby. SEM exposure was minimized by blanking the beam when not actually viewing crystallites. The protective Al film was later removed using a 15 minute etch in NaOH solution, roughly 0.4 g NaOH in 100 ml DI, and rinsed well in DI.

Sacrificial alignment marks were then applied near each crystallite using e-beam lithography. To do this, e-beam resist (950K PMMA, 7.5% solids) was first spin-applied to the substrate at 3,400 rpm for 30 seconds and then baked at 145 °C for 35 minutes in a covered petri dish. After cooling, silver-paint reference marks were made near each crystallite for rough location in the SEM. Crystallites were located for alignment purposes during beam writing by scanning a

40x40 µm alignment window with 0.25 µm dot spacing using about 3 pA beam current. Alignment marks were written at 45° to the reference orientation for each crystallite. Following e-beam exposure, samples were developed for 70 sec in one part MIBK to 3 parts isopropyl alcohol at room temperature and immediately rinsed in isopropyl alcohol, DI and then blown dry with nitrogen gas. This will be referred to as standard PMMA developing. The sacrificial alignment marks were then metallized at normal incidence with 100 nm Al followed by 100 nm of Au. The PMMA was then dissolved away in acetone, leaving the alignment marks behind.

A permanent set of alignment marks was then fabricated by a similar sequence of steps except that the sacrificial alignment marks were used for crystallite location and alignment to prevent the crystallite itself from being exposed to the alignment scan. The permanent alignment marks were metallized with 15 nm of Ti and 200 nm of Au. Following lift-off, the entire substrate was coated with a protective coating of 30 nm of Al at normal incidence. Each crystallite was then photographed in the SEM to record the alignment mark offset. Figure 33 shows an SEM photo of a
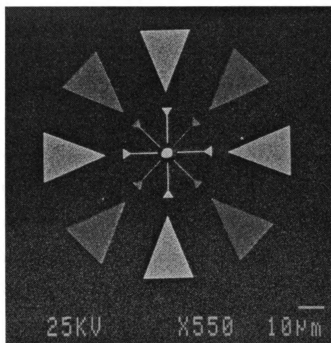
Figure 33 Isolated crystallite with both sacrificial and permanent alignment marks.

single isolated crystallite with both sets of alignment marks. The contrast difference between the sacrificial and permanent marks is attributed to differences in SEM signal created by the different metal thickness and content of each set of marks. The sacrificial alignment marks, the Al coating, and any alignment scan dot artifacts from sacrificial alignment mark fabrication were then removed by a 30 minute etch in NaOH solution.

Thick PMMA was again applied as above and custom-designed submicron contacts pads written onto the top facets of each crystallite structure. The alignment mark offset obtained from the SEM photographs was used to ensure $\leq$ 0.2 μm alignment error on the crystallite facets. After developing the PMMA, the contact pads were metallized with 17 nm Ti at 2.3 nm/sec and 100 nm Au at 2.3 nm/sec, deposited at normal incidence without breaking vacuum. Following resist lift-off, the entire substrate was annealed in a UHV chamber to effect a solid-state reaction between the Ti and the diamond at the contact pads. The best anneal parameters were for 60 minutes at over 650 °C at pressures less than or of order 10^{-6} torr. This annealing process is believed to alter the metal-semiconductor contact chemistry in such a way as to produce Ohmic contact.[98]

The samples were then coated with 30 nm of Al at $\geq$ 60° to the substrate normal while rotating, so that the top and sides of the crystallites were coated. Each crystallite was then photographed at normal incidence and at four other distinct viewing orientations to record the 3D geometry of the crystallite and the contact pads. Such a series of photos is shown in Figure 34. These photos are later used to reconstruct the detailed crystallite and contact pad geometry when modeling the current distribution as discussed in the analysis section below (Section IV.3.C.ii.b). The protective Al coating was removed with a 10 minute etch in NaOH and rinsed well in DI.

The next step was to create a polyimide layer to planarize the substrate topography for the application of electrical leads to the contact pads. This was done by first spinning on adhesion-promoter solution at 5,000 rpm for 60 sec and then baking the substrate dry for 1 minute at 140 °C in an uncovered petri dish. After cooling, polyimide was spin-applied at 5,000 rpm for 60 sec and

θ = 0°

θ = 50°, φ = 90°   θ = 50°, φ = 0°

θ = 50°, φ = 180°   θ = 50°, φ = 270°
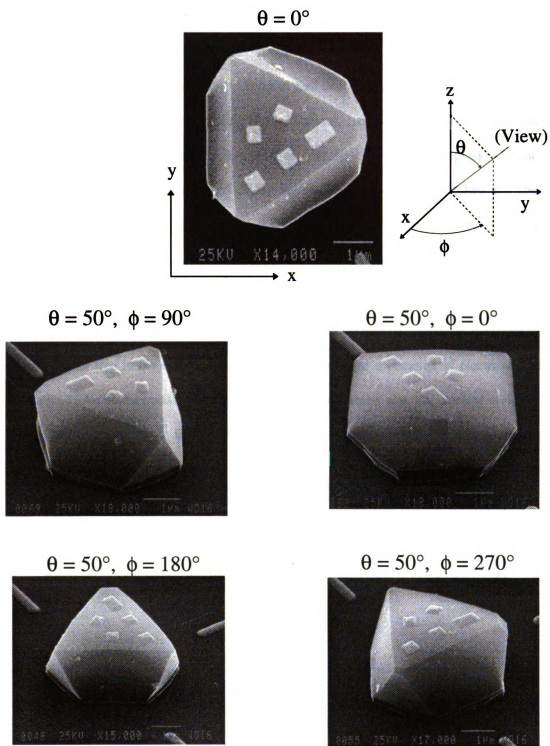
Figure 34 Series of photos documenting microcrystallite geometry. (Sample MC-A.)

then lightly cured under an infrared lamp for 3.5 hours. The polyimide layer was then back-etched isotropically in diluted photoresist developer to lower the level of the planarized landscape to just below the tops of the diamond crystallites. It was crucial in this step to ensure that crystallite undercuts were sufficiently buried under polyimide and that the top facets of the crystallite were etched clean of polyimide where contact pads are located. It was not possible to calibrate the etching process well enough to ensure this level of coverage, so the etch progress was checked periodically in an SEM after rinsing and drying the sample. Samples were etched and checked repeatedly until crystallite coverage appeared as shown in Figure 35 when crystallites were viewed at a 50° angle from the substrate normal. The etching process is described in greater detail in Section 1 of Appendix A. After a final rinse with DI, the substrate was then baked for 10 minutes in a 140 °C preheated oven to further cure the polyimide.

The final step in the contact fabrication process was the application of electrical leads to the annealed Ti/Au contact pads. A thinner layer of PMMA resist was spin-applied at 4,000 rpm for 30 sec and baked as usual. Electrical lead patterns were written which overlapped the contact
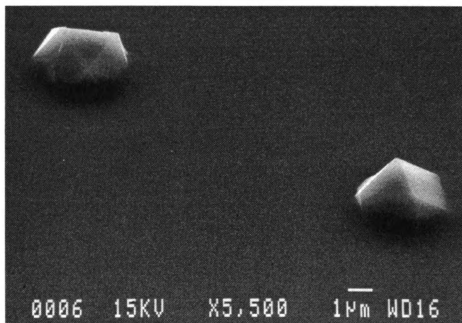
Figure 35 Microcrystallites with a back-etched polyimide planarization layer.

pads on each crystallite and expanded out to form macroscopic pad regions 400 μm x 400 μm. Alignment to ≤ 0.2 μm was accomplished using the alignment marks. The PMMA was developed in standard fashion and 200 nm Au deposited at normal incidence by thermal evaporation. The contact process was finished following PMMA lift-off.

A crystallite with contacts produced using this process is shown in Figure 36. The Au leads can be seen overlapping submicron annealed Ti/Au contact pads on top of the crystallite. Some of the lower leads to this sample have jagged edges where poor lift-off resulted from proximity exposure to regions with thin resist. The leads expand to form the macroscopic Au-pads outside the region shown in the photo. Fine Au wires are attached to these pads using silver-paint to electrically contact the sample. Figure 37 presents a side view of a contacted microcrystallite which shows how the lithographic Au leads taper up the polyimide profile at the edge of the crystallite and contact Ti/Au pads on the top facet. The two Au leads at the back of the picture have been destroyed near the crystallite by static discharge during measurement.
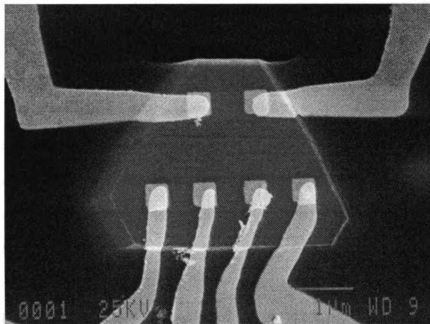
Figure 36 Planarized microcrystallite with Ti/Au pads and Au contact leads. (Viewed normal to substrate.)
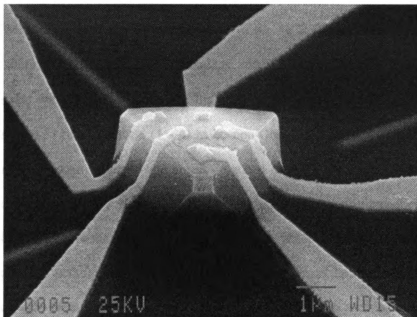
Figure 37 50° side view of a contacted crystallite (MC-A) showing Au leads conformal to the tapered polyimide profile. Au leads contact Ti/Au pads on the crystallite's top facet. (See also Figure 42.)

5.   FABRICATION OF ELECTRICAL CONTACTS TO HOMOEPITAXIAL AND POLYCRYSTALLINE FILMS

Electrical contacts were also formed on homoepitaxial and polycrystalline films of boron-doped diamond. No submicron lithography or polyimide layers were necessary for these films, though contacts were defined using e-beam lithography as a matter of convenience.   The homoepitaxial film was first etched off in buffered hydrofluoric acid to remove the SiO_2 edge mask which defined the boron-doped diamond growth region. It was then electrochemically etched to remove surface graphite in the same fashion as was done for the low-nucleation density crystallite samples, and then also de-metal etched.   The initial gray tint to the otherwise optically clear substrate lightened noticeably during the graphite etch, when compared to an unetched, identically grown sample of the same initial color. PMMA was spin-applied at 4,000 rpm and baked for 30 minutes at 140 °C. Square contact patterns 300x300 μm^2 were written near the corners of the 3x3 mm^2 region of boron-doped diamond.   After standard PMMA developing, the substrate

underwent a short reactive-ion etch (RIE) using an oxygen plasma to clean the diamond surface and remove any PMMA residue in the contact regions. 15 nm of Ti followed by 180 nm of Au was deposited by thermal evaporation without breaking vacuum. The resist was lifted off and the diamond substrate with contacts annealed in high vacuum at 650 °C for one hour. Subsequent measurements showed these contacts (1 - 4) to be non-Ohmic. Oxygen RIE has been noted to oxygen-terminate diamond surfaces and result in metal-diamond contacts exhibiting Schottky barrier characteristics. Following measurement, these contacts were removed using aquaregia (2 HCl: 1 HNO$_3$) to remove the Au and an HF solution (50 ml DI: 3 ml HCl: 1 ml HF) to remove the Ti. New contacts were fabricated in exactly the same locations as the first contacts (1 - 4) using the same lithography steps above, but skipping the RIE process. Two additional new contacts (5 and 6) were also fashioned adjacent to two of the old contacts on "virgin" diamond surface. These contacts were annealed as before and were noted to yield Ohmic contacts to the doped diamond. The oxygen RIE process appeared to be the cause of the non-Ohmic behavior of the first contacts. The final contact geometry with the second set of contacts is shown in Figure 38.

The polycrystalline film was not subjected to a graphite etch for fear of removing significant amounts of material from the grain-boundaries. The film was subjected to a de-metal etch, followed by a quick SiO$_2$ etch in buffered HF to clean the edges of material which might short the film to the low resistance silicon wafer under the 4 μm SiO$_2$ layer. Ti/Au contact pads were fabricated in the same fashion as the second set of pads on the homoepitaxial sample and annealed identically. These contacts showed Ohmic behavior both before and after the annealing process. The sample configuration was that of a thin, square film with contacts in each corner.
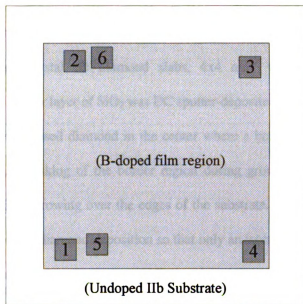
Figure 38 Geometry of the homoepitaxial film showing contact pad positions.

6.   ELECTRONIC TRANSPORT MEASUREMENTS OF CVD DIAMOND SAMPLES

A.   Sample Descriptions

Early samples were seeded by the diamond-seeded photoresist method and grown by the hot-filament technique. These methods were used initially because nucleation densities are very controllable with the photoresist seeding method and because the hot filament CVD diamond reactor was available for use on the MSU campus. Use of the hot-filament reactor was discontinued, however, as it was considered unsuitable for producing diamond films with controllable levels of intentional dopants. Boron-doped diamond samples used to characterize the electronic properties of diamond were all grown at Kobe Steel using the microwave-plasma assisted technique. Except for homoepitaxial samples, substrates were p-type silicon wafers with a 4 μm oxidation layer seeded using the scratch technique. As the ultrasonic scratch treatment was not yet calibrated to produce low-nucleation density seeding, samples with isolated microcrystal structures were seeded using the light mechanical abrasion technique. One continuous polycrystalline film

sample grown on similar oxidized silicon was seeded using a 10 minute ultrasonic abrasion treatment in the diamond slurry formula mentioned above. In addition, two (100) oriented, insulating, natural single-crystal IIb diamond slabs, 4x4 mm^2 were used as substrates for homoepitaxial films. A border layer of SiO_2 was DC sputter-deposited on top of each slab leaving a 3x3 mm^2 square area of exposed diamond in the center where a boron-doped diamond layer was grown homoepitaxially. Masking of the border region during growth was necessary to prevent boron-doped diamond from growing over the edges of the substrate. The SiO_2 border was etched off in buffered HF following diamond deposition so that only an isolated 3x3 mm^2 region of boron-doped diamond film remained in the center. All samples measured were grown under contract during the same deposition run at Kobe Steel USA, Inc., except for the polycrystalline film which was grown in a separate run under identical conditions as the other samples, but with doubled growth time. As determined by surface profilometry, the (100) homoepitaxial film had an average thickness of 1.86 μm and varied by ± 0.05 μm across the film. The polycrystalline film had an average thickness of 6.22 μm as measured at one film edge. Surface profile scans could not be made at the other edges to check film uniformity because a high density of stray diamond crystallites near the other edges prevented clear referencing of the film height to the substrate. Isolated single crystallites ranged in size and shape, with the most favorable shape being flat platelets up to 6 μm in diameter and roughly 1.5 μm high, as shown in Figure 27.

The samples measured in this study are listed in Table 7 along with descriptions of their physical characteristics. SEM micrographs of the two microcrystals that were measured are shown in Figure 40 and Figure 39. The numerical labels on the Ti/Au contact pads are used to identify lead geometry for multiprobe measurements, and will be referred to throughout the next chapter. MC-B has a visible planar defect running from left to right across the center of the top face and down the right face as shown in Figure 39. This defect is parallel to (111) planes and is considered a twin.

Table 7 Measured boron-doped CVD diamond samples for this study.

Sample Label	Description	Growth Run[†]
MC-A	Isolated microcrystal with no visible defects. Grown on oxidized Si substrate. Crystal dimensions: ~ 4 μm diameter, ~ 2 μm tall. Sample photos in Figure 34, Figure 40, and Figure 42.	1
MC-B	Isolated microcrystal with one visible twin defect. Grown on oxidized Si substrate. Crystal dimensions: ~ 4 μm diameter, ~ 2 μm tall. Sample photo in Figure 39.	1
HF-1	Homoepitaxial film on single-crystal (100) natural diamond substrate with 1st set of contacts 1, 2, 3, 4. Sample dimensions: 3.0 mm x 3.0 mm x 1.86 μm Contact dimensions: 0.3 mm x 0.3 mm (See HF-2 for contact geometry.)	1
HF-2	HF-1 with 2nd set of contacts: 1, 2, 3, & 4 reapplied, plus additional contacts 5 and 6. Geometry shown in Figure 38. Contact dimensions: 0.3 mm x 0.3 mm	1
PF-1	Unannealed polycrystalline film grown on scratch-treated oxidized Si substrate. Square film sample with one contact in each corner. Sample dimensions: 3.8 mm x 3.8 mm x 6.22 μm Contact dimensions: 0.3 mm x 0.3 mm	2
PF-2	PF-1 after annealing contacts.	2

[†]All diamond samples measured were grown under contract by microwave plasma enhanced CVD at Kobe Steel USA, Inc. CVD Runs 1 and 2 were under identical reactor conditions, except that Run 2 was for twice the growth time of Run 1.
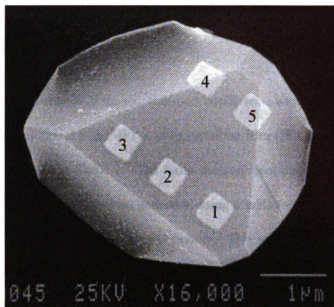
Figure 39 SEM micrograph of sample MC-B showing Ti/Au contact pad labels 1-5. (Viewed normal to substrate.)
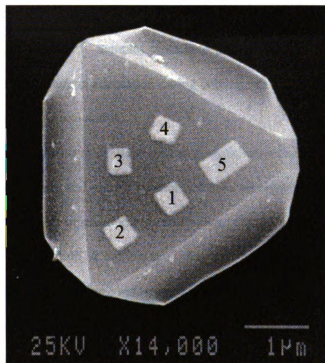
Figure 40 SEM micrograph of sample MC-A showing Ti/Au contact pad labels 1-5. (Viewed normal to substrate.)

B.   Transport Measurements

i.   I-V and Resistance

Four-probe measurements of the d.c. transport coefficients were conducted as a function of temperature for a homoepitaxial film (HF), a polycrystalline film (PF), and for two microcrystals (MC-A and MC-B) as listed in Table 7. The basic measurement circuit is shown in Figure 41. Voltage ramps for I-V characteristics were generated using a mHz frequency triangle wave from a Hewlett Packard 3325A Synthesizer/Function Generator. This voltage was dropped across a load resistor R in series with the current leads of the sample, I_1 and I_2. Current through the sample was obtained by measuring the voltage drop across R using a Hewlett Packard 3457A multimeter and using Ohm's law. The voltage drop across the sample's voltage leads V_1 and V_2 was similarly measured with a second HP3457A multimeter. These two voltages were recorded by a computer interfaced to the two multimeters. The HP3457A multimeters had an input impedance of 10 GΩ for voltage ranges up to 3V. Temperature was measured using a type-K thermocouple with a reference junction held at 0 °C.[119] Samples were held under less than 10^{-6} torr vacuum during measurement to prevent moisture condensation during cooling runs down to 190 K and to prevent oxidation during heating runs up to 450 K.

Four-probe measurements at constant applied potential were facilitated by replacing the HP 3325A with a dc power supply and voltage divider and then monitoring the applied voltage at the current leads with a third high input-impedance voltmeter. Four-probe measurements at constant current were made with the HP3457A multimeter in the four-wire resistance mode. In this case the current was determined by the resistance range setting of the multimeter, eg. 100 nA for the 30 MΩ range. Measurements at constant voltage applied across the current contacts were preferred when monitoring the temperature-dependent resistance for a given multiprobe lead configuration. Measurements at constant sample current were preferred when comparing resistances for different
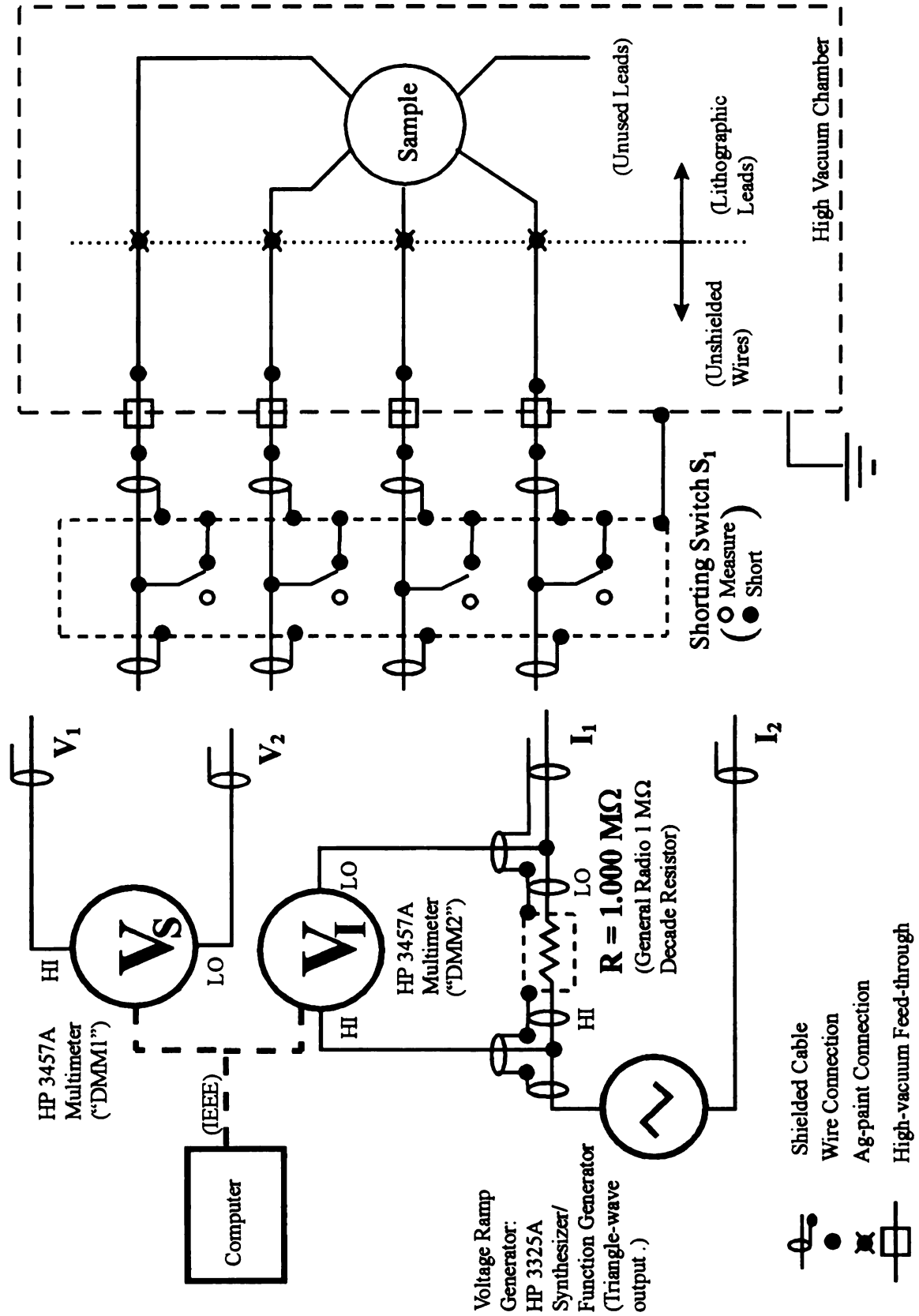
Figure 41 I-V measurement circuit.

contact configurations at a specified fixed temperature as it kept contact resistances more constant in the case of non-linear contact I-V characteristics.

ii.   Hall Response

Measurements of the Hall response for the homoepitaxial film and the polycrystalline film were conducted in a Quantum Design Magnetic Property Measurement System (MPMS) to take advantage of its 5 Tesla magnetic field capabilities and temperature control from liquid helium temperatures up to 380 K. Measurements at constant current in this system were done using a Keithley 224 Programmable Current Source and a Keithley 182 Sensitive Digital Voltmeter with an input impedance of greater than 10 $G\Omega$. Hall measurements were not conducted on microcrystals since no samples survived transfer from the vacuum system in which resistivities were measured to the Quantum Design system in which Hall measurements were to be made.

iii.   Electrical Fragility of Submicron Leads

Submicron leads to microcrystals were particularly fragile electrically, and unintentional static discharge frequently overloaded the portion of the leads where they taper up the crystallite edges. Figure 42 shows a crystallite with three blown leads. The ends of the metal leads appear melted and entire sections are missing. In many cases blown leads could be repaired lithographically provided the Ti/Au contact pads were not destroyed. A shorting switch S_1 (Figure 41) was available to short all leads simultaneously to ground to help protect the leads from static discharge and voltage spikes when changing lead configurations or drive settings. Drive voltages were also smoothly reduced to zero before shorting or unshorting the sample leads. Connection to the multimeter V_S or drive circuit was not broken during the shorting process since the switch was not make-before-break.
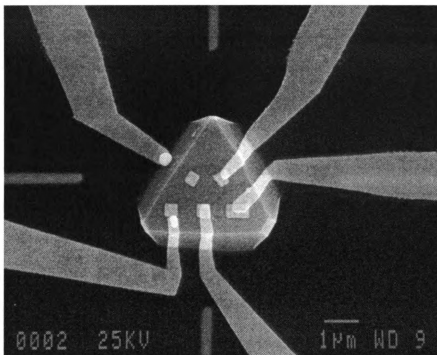
Figure 42 Microcrystallite MC-A with blown leads. (See Figure 37 for a side view.)

The current and voltage ranges of I-V measurements were limited by either the requirement of maintaining a high voltmeter to sample impedance ratio ($\geq$ 100:1) or by intentionally limiting current to prevent sample failure as in the case of microcrystals. Lead cross-sections were suspected to be much smaller where leads tapered up the sides of crystallites or overlapped Ti/Au contact pads compared to where they extended over level terrain, so current densities were kept far below the 10^6 A/cm^2 limit typical for metallic leads. Leads to one crystallite were destroyed at 20 μA current, so measuring currents in microcrystals were afterwards kept below 10 μA, severely restricting I-V ranges.

iv.   Effects of Adsorbed Gases on Microcrystal Resistance

The measured resistance of lithographically contacted microcrystal samples was much lower when they were exposed to air. The low resistance persisted even after samples were held

under 10^{-6} torr vacuum for over 48 hours. The four-terminal resistance changed dramatically upon heating to over 100 °C while held under less than 10^{-6} torr vacuum, as shown in Figure 43. The figure shows the four-terminal resistance for MC-A measured in the $I_{23}V_{14}$ configuration while under vacuum as the temperature is cycled from room temperature down to -90 °C, raised to > 155 °C , held slightly above that temperature (155 °C < T < 165 °C) for 3 hours, and then cooled back to room temperature. The arrows in the figure indicate the direction of the temperature change for the data sets. The sample had not been heated in vacuum prior these measurements. The temperature dependence of the resistance does not change from room temperature down to -90 °C and back. When heated above room temperature, the temperature dependence changes in an irregular fashion and depends on the heating rate, which was non-uniform for this temperature scan. After annealing at > 155 °C for 3 hours, the sample was cooled back to room temperature during which the resistance temperature dependence was proportional to $\exp(E_o/kT)$, where the activation energy E_o = 0.306 eV. The sample was annealed twice more without breaking vacuum and the activation energy increased to E_o = 0.317 eV after the first additional annealing at 160 °C for 1 hour, and changed only slightly to E_o = 0.323 eV after the second additional annealing at > 150 °C for 2.5 hours. This resistance change upon heating in vacuum is interpreted as due to desorption of a surface layer which has lower resistivity than the diamond. As a result, all resistance data for microcrystallites presented in this work was taken after first baking the crystallites at less than 10^{-6} torr at greater than 150 °C for over 5.5 hours to ensure that such low resistance surface layers did not affect the results.

In an attempt to identify the gas which is responsible for these low resistance adsorbed layers, the temperature and four-terminal resistance of a vacuum-baked microcrystallite (MC-B) was monitored while venting the vacuum chamber. The results are shown in Figure 44. The resistance was constant during the first 6 minutes while the crystallite was under less than 10^{-6} torr vacuum and roughly at thermal equilibrium. No change in resistance or temperature occurred while
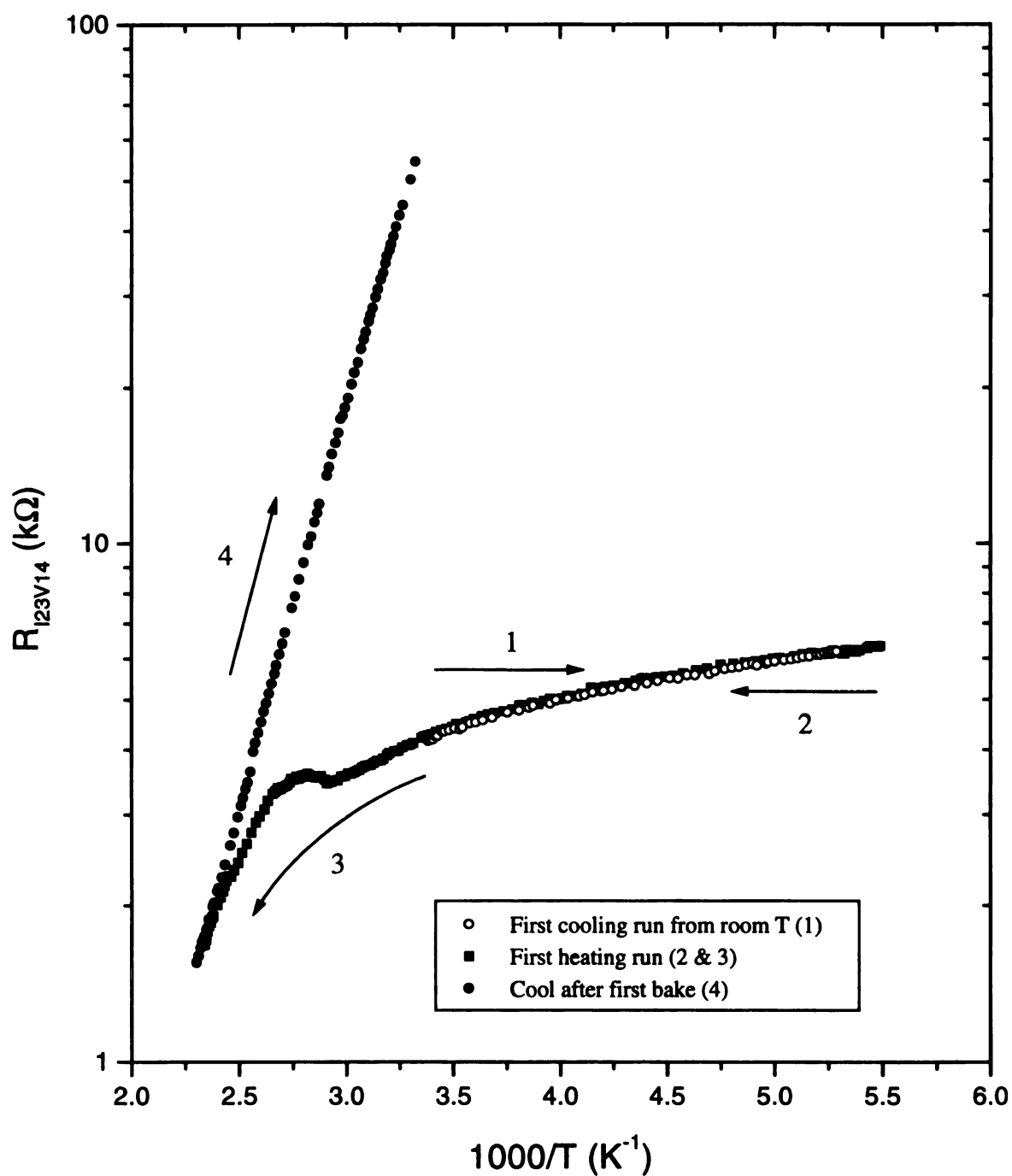
Figure 43 Change in four-probe resistance upon heating under vacuum for a lithographically contacted microcrystal (MC-A).
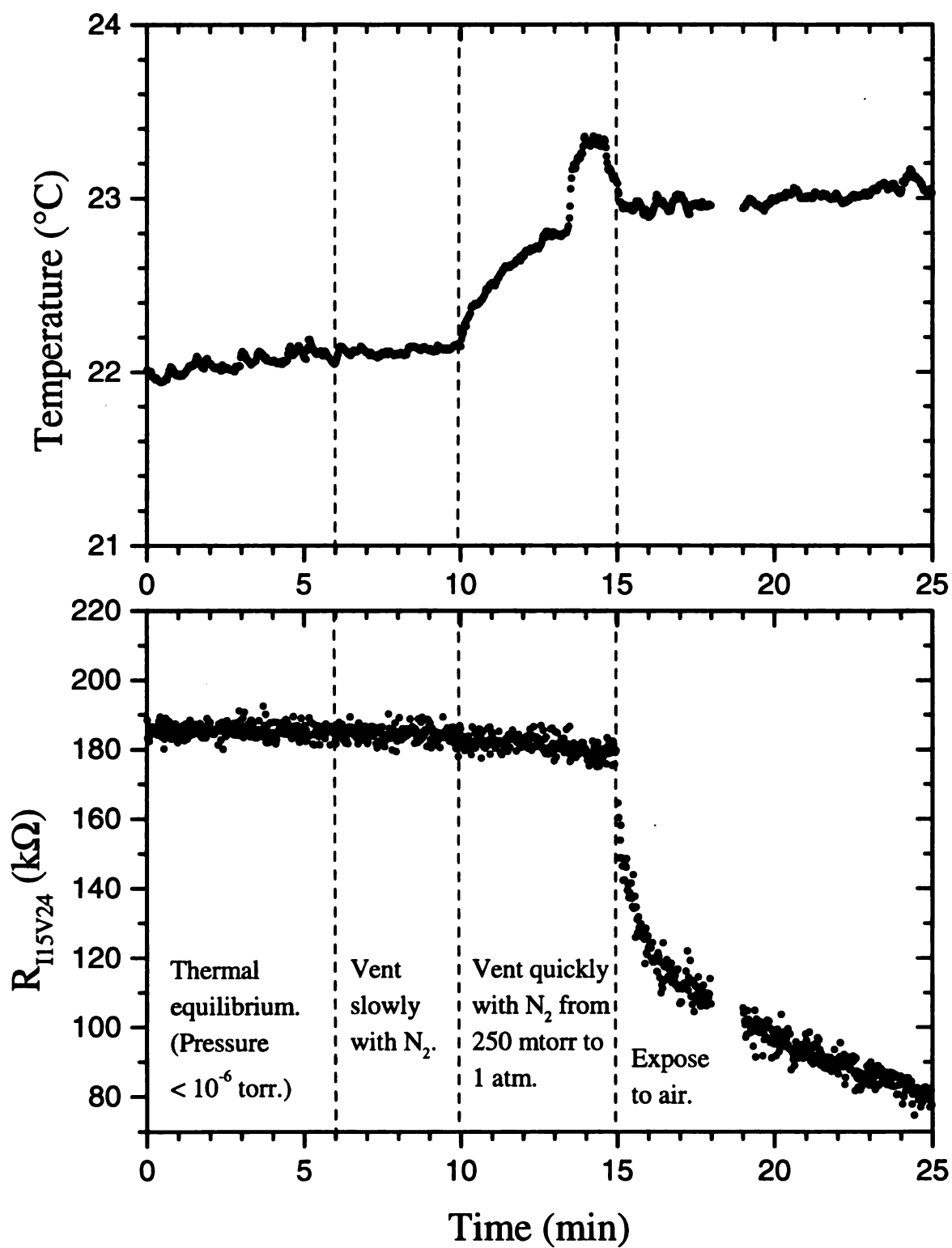
Figure 44 Change in four-terminal resistance and temperature of a vacuum-baked microcrystallite (MC-B) during exposure to N_2 and air.

dry N_2 gas was slowly let into the vacuum chamber from Time = 6 min until Time = 10 min. The

vent rate was increased from Time = 10 min until Time = 15 min, resulting in a very small decrease

in resistance of about 8 kΩ which correlates with a small increase in temperature. This small

resistance change is due to the strong temperature-dependence of the bulk diamond. At Time =

15 min, the vacuum chamber contained 1 atm of N_2. The bell jar was removed at Time = 15 min to

suddenly expose the crystallite to air, and the resistance dropped dramatically by 30% in the first

minute of air exposure with essentially no corresponding change in sample temperature. The

resistance of the HF sample did not change with vacuum annealing or sudden exposure to air

following the bake. It was therefore concluded that adsorbed gases other than N_2 form a low

resistivity surface layer on lithographically contacted diamond microcrystallite devices, and that this

layer can be removed by baking the sample in high vacuum for over 5.5 hours at 150 °C or higher.

It is not known for certain whether this adsorbed surface layer forms on the diamond, on the

polyimide surface between Au leads and pads, or both, though it is unlikely that it forms on the

diamond since the homoepitaxial film exhibited no such effect.

C.   Sample Characterization with Raman Spectroscopy

The homoepitaxial and polycrystalline diamond films were also characterized by Raman

spectroscopy using a Kaiser Optical Systems, Inc. Raman system. The system uses the 532 nm line

from a CW frequency doubled Nd:YAG laser operating in a backscattering configuration, dispersed

via a holographic transmission grating, and imaged onto a CCD array with spectral resolution of

5 cm^{-1}. Though the maximum laser output was 100 mW, the spectra were taken at less than 10% of

this power focused over a spot area of less than 1 mm^2. Spectra were also taken at higher power to

check for optically induced damage in the samples. The Raman spectra for the polycrystalline film

and the homoepitaxial film are shown in Figure 45. Both films show prominent peaks near

1332 cm^{-1} which is the signature of the highest vibrational mode of crystalline diamond. Presence
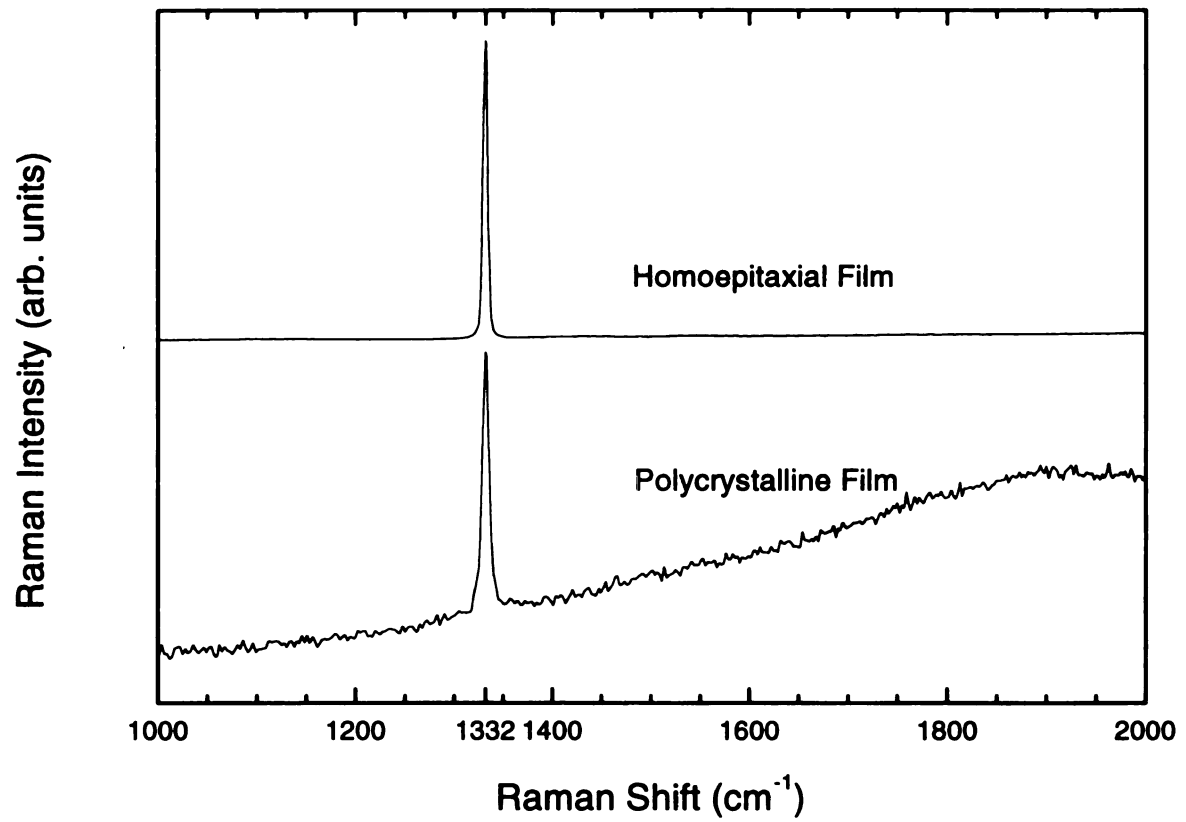
Figure 45 Raman spectra for homoepitaxial and polycrystalline diamond/oxidized Si
boron-doped CVD films.

of a broad hump between 1350 cm^{-1} and 1580 cm^{-1} is characteristic of polycrystalline graphite or amorphous carbon with graphitic bonding, and is absent in both films to within the noise level of the measurements.[57] Raman scattering associated with sp^2 carbon is much stronger than that associated with sp^3 carbon, so even small amounts of sp^2 carbon, if present, show up prominently in the spectra. Modeling the ratio of sp^2 to sp^3 carbon present in the films from the Raman spectra is non-trivial and requires considerable effort in calibration using other carbon sources of known bonding composition.[58] A meaningful analysis of the full width at half maximum of the diamond peaks was not attempted since the width of the peak in natural diamond[59] is 2.3 cm^{-1}, which is below the resolution of the spectra presented here. The stress in the films was similarly not analyzed from the diamond peak shift from 1332 cm^{-1}, since such shifts are only about 2 cm^{-1} for net stresses of order -2.21 GPa which are typical for diamond films on non-diamond substrates.[60,120] The absolute intensities of these two spectra cannot be compared directly. It should be noted that even if the laser probed to a depth greater than the 1.8 μm thick boron-doped CVD layer to include signal from the single crystal natural diamond substrate, the lack of any graphitic signature in the homoepitaxial spectra indicates that the homoepitaxial film is of excellent crystalline quality.

Chapter VI

RESULTS AND DISCUSSION

1. CHAPTER OVERVIEW

The data taken as described in the preceding chapter were analyzed to characterize the metal-diamond contacts and to obtain the temperature dependent transport parameters for the diamond samples. The temperature dependence of the transport parameters is compared to that predicted by standard semiconductor models, and the results are used to build a picture of the transport properties of grains and grain-boundaries in B-doped CVD diamond.

In the first section of this chapter, the current-voltage (I-V) behavior of the electrical contacts are characterized and their influence on the transport measurements is considered. The second section analyzes the resistance of the diamond film samples to obtain the resistivity. The van der Pauw method for the resistivity of thin film (2D) samples is used for the large area homoepitaxial and polycrystalline films, but cannot be used for the 3D microcrystal geometries. A method is therefore developed for obtaining the geometrical factors which relate resistance to resistivity for arbitrarily shaped crystallites. The resistivities for the diamond microcrystals and the large area films are then presented and compared. The resistance and resistivity data for the microcrystallites is the first data ever presented for nominally single-crystal heteroepitaxial CVD diamond, and represents the first electrical transport measurements ever performed on individual micron-sized single-crystal semiconductors.

The Hall-effect measurements on the large area films are analyzed in Sections 3-4 to obtain the Hall coefficient, carrier concentration, and Hall mobility for those samples. The temperature dependence of the above mentioned transport parameters is then fit to the model presented in Chapter II for a compensated, lightly doped semiconductor. To the extent that the data is available, the results are compared for the three basic film morphologies represented by the samples and

conclusions are drawn regarding electrical transport in polycrystalline CVD diamond films. The results are also compared to a parallel study by Malta *et al.*,[1] which presents similar measurements on large area film samples produced using the same technique as that used for the samples of this study.

2. ELECTRICAL CONTACT CHARACTERIZATION

The electrical contacts to each sample were characterized by I-V (current-voltage) curves and contact resistance. The contact resistances were obtained from analysis discussed in the next section, Section IV.3. Resistivity, so their discussion will be reserved for that section. The polycrystalline sample PF displayed Ohmic behavior at room temperature for all contact geometries both before annealing (PF-1) and after annealing (PF-2) over ranges of several volts and roughly 20 μA. The annealed Ti/Au contacts to nominally single-crystal diamond surfaces, however, generally displayed slightly non-Ohmic I-V characteristics at room temperature. The room temperature I-V characteristics of contacts to the homoepitaxial sample (HF-1 and HF-2) and to the two microcrystals (MC-A and MC-B) were not unambiguously either linear or non-linear for any given sample. The degree of non-linear behavior was different for each contact, despite the fact that all contacts for a given sample were fabricated under identical processing conditions.

A. Four-terminal I-V Characteristics–Bulk Effects

Contact resistance effects can be separated from bulk sample effects by observing differences between two-terminal, three-terminal, and four-terminal I-V measurements. Four-terminal I-V measurements sample only the bulk sample resistance and are independent of contact resistances since no current flows through the voltage contacts. Four-terminal I-V curves for HF-1 and HF-2 were linear over the temperature range of resistance measurements, roughly 200 K to 440 K. Four-terminal I-V curves for microcrystal MC-B were linear below approximately 0.2 V for
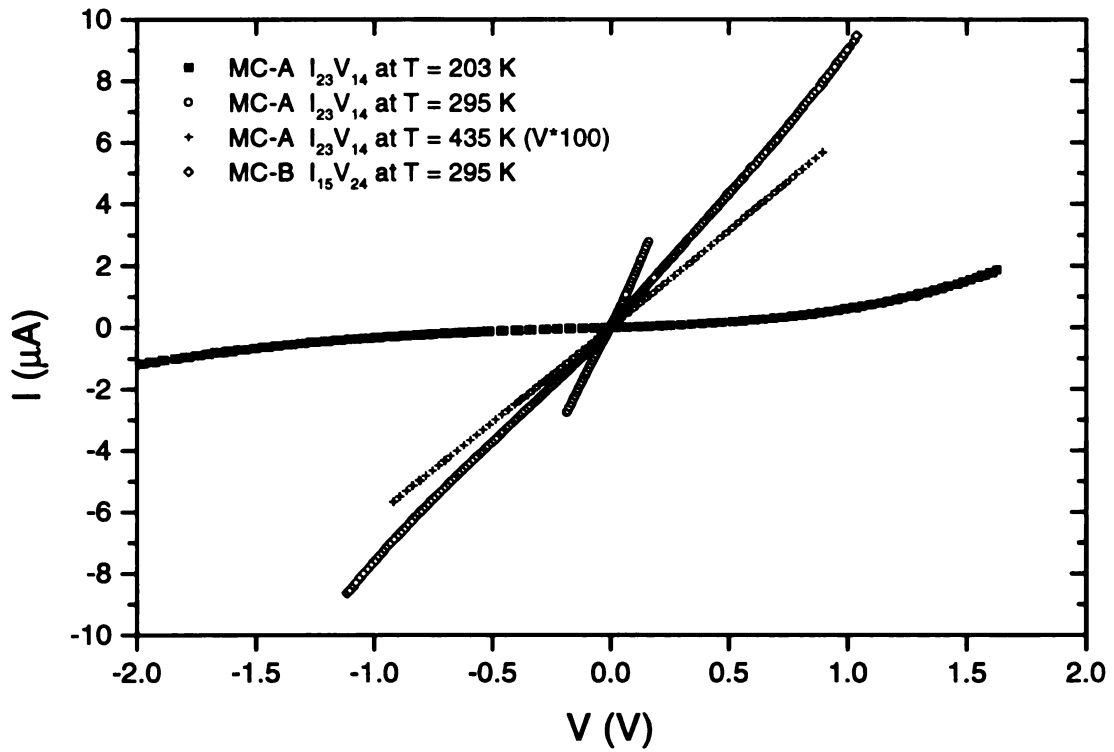
Figure 46 Four-terminal I-V curves for diamond microcrystal samples.

all temperatures, with linearity above 0.2 V improving with increasing temperature. The four-terminal I-V curves for microcrystal MC-A, however, were highly non-linear below room temperature and linear below a few tenths of a volt for temperatures above room temperature. Figure 46 shows four-terminal I-V measurements for MC-B in the $I_{15}V_{24}$ measurement configuration at 295 K and for MC-A in the $I_{23}V_{14}$ measurement configuration for temperatures at 203 K, 295 K, and 435 K.

B.   Non-Ohmic Effects in Four-Terminal Measurements

The non-Ohmic behavior observed in low-temperature four-terminal resistance measurements on microcrystals is likely due to several concurrent effects related to the submicron

contact separations. This section describes two of these effects: hot carrier effects at high electric fields and large space-charge regions associated with metal-semiconductor contacts.

i.   Hot Carrier Effects at High Electric Fields

The electric field between closely spaced contacts can be very high even if the applied voltages for I-V measurements are kept below a few volts. This is because the magnitude of the electric field E scales roughly as the voltage V divided by the contact separation d, at least for geometries similar to that of a parallel-plate capacitor. Hence, 1 V applied across 1 μm results in a field strength of $\sim 10^4$ V/cm, which is a field magnitude where many semiconductors begin to show non-Ohmic behavior.

At low electric fields the drift velocity v_d of carriers is proportional to the electric field E by the drift mobility μ according to $v_d = \mu E$. The mobility is independent of the field in this case. In thermal equilibrium the carriers emit and absorb phonons with zero net energy exchange. At low fields, the carriers gain energy from the field and emit it as phonons, with more phonons emitted than absorbed. At high applied fields, however, the carriers can gain energy since they cannot emit energy via optical phonons as fast as they gain it from the electric field. The result is that the carriers are more energetic, or hotter, than the crystal temperature. In Si and Ge the effective temperature of the carriers T_e is related to the lattice temperature T by[121]

$$\frac{T_e}{T} = \frac{1}{2}\left\{1 + \left[1 + \frac{3\pi}{8}\left(\frac{\mu_o E}{C_s}\right)^2\right]^{1/2}\right\}$$

where C_s is the speed of sound in the semiconductor and μ_o is the low field mobility. The drift velocity is

$$v_d = \mu_o E \sqrt{\frac{T}{T_e}}$$

The mobility deviates from a constant value at low fields when the product $\mu_o E$ is comparable to C_s, and the drift velocity simplifies to[121]

$$v_d \cong \mu_o E \left[1 - \frac{3\pi}{64} \left(\frac{\mu_o E}{C_s} \right)^2 \right].$$

(13)

The drift mobility can be obtained from the Hall mobility from $\mu_o = r\mu_H$. For diamond we assume a value of 1 for the Hall factor r so that $\mu_o = \mu_H$. Using the room temperature value of the Hall mobility for holes in homoepitaxial doped diamond from Malta et al.,[1] namely $\mu_H = 427$ cm^2/V-s, and an average speed of sound in diamond at room temperature[122] as ~ 1.5×10^6 cm/s, the condition $\mu_o E \sim C_s$ is satisfied at applied fields $E \sim 3.5 \times 10^3$ V/cm, or 0.35 V/μm. Thus, we should expect to see "warm" carrier effects in diamond microcrystals with contact separations ~ 0.4 μm for applied voltages above about a tenth of a volt.

ii.   Space-Charge Limited Currents

As presented previously in Chapter II, a region of space-charge exists in a semiconductor just inside of a metal-semiconductor contact if the potential barrier at the interface is non-negligible. Such a space charge region could span the entire distance between contacts for micron-sized samples with submicron contact separations. To estimate the space-charge width associated with the annealed Ti/diamond contacts in this study, we start with Equation 9 for the dependence of the space-charge width on the applied voltage. For moderately doped diamond most acceptors are *not* ionized at room temperature, as demonstrated by Malta et al.[115] who showed that the room-temperature hole density for homoepitaxial boron-doped diamond is 3.1×10^{14} cm^{-3} for an acceptor concentration $N_A = 1.1 \times 10^{18}$ cm^{-3} and boron concentration $N_B = 2 \times 10^{18}$ cm^{-3}. This low ionized acceptor concentration is traced to the fact that the boron acceptor ionization energy 0.35 eV is large compared to kT (~ 0.026 eV). An accurate determination of the ionized acceptor density at

lower temperatures requires knowledge of the Fermi level E_F.[123] An estimate for N_A^- can be taken as the effective hole concentration if low compensation is assumed. To estimate the width of the space-charge layer at an annealed Ti/diamond contact at zero applied bias at room temperature, we use Malta's value for the hole concentration, a dielectric constant[124] for diamond of 5.7, and use the actual Schottky barrier height as an upper bound for the built-in potential V_{bi}. The Schottky barrier height for most metals on doped diamond ranges from roughly 1 to 2 eV[100] and is believed to be relatively independent of metal work function due to pinning of the Fermi level by surface states. A value of 1 eV will therefore serve as an upper bound for the barrier of an annealed Ti/diamond contact in which the carbide formed by the annealing process has significantly reduced the Schottky barrier effect. For these values the width of the space-charge region in the diamond is approximately 1.4 μm at room temperature and increases in width at lower temperature because fewer acceptors are ionized. This shows that space-charge regions in B-doped diamond may extend appreciable distances into the diamond at non-Ohmic metal-diamond contacts. It is of special concern for samples with submicron contact separations, such as the lithographically contacted microcrystals of this study which have contacts separated by as little as 0.4 μm in some cases. It should be emphasized that the 1.4 μm value calculated above is likely an extreme upper bound for the actual width of an annealed Ti/diamond contact, since such contacts have been reported to yield Ohmic behavior in many cases,[104,105,106] and therefore must have a barrier much less than 1 V. According to Equation 9 for W, the width at zero bias decreases roughly as $\sqrt{V_{bi}}$ so that a Schottky barrier of 0.01 eV yields a corresponding space-charge width of 0.14 μm for this example. For a four-terminal measurement, variation of the space-charge width with applied voltage acts to change the volume of host semiconductor which has majority carriers to conduct current.

iii.   Minority Carrier Injection at Point-Contacts

High current densities exist at point contacts to semiconductors, and can give rise to minority carrier injection if the contacts are rectifying. This increases the carrier density near the contact and can affect I-V characteristics. A discussion of these effects is given by Shockley.[3]

C.   Two-terminal I-V Characteristics–Combined Contact and Bulk Effects

Non-linear effects in two and three-terminal I-V curves which include contact resistances were attributed to rectifying contacts as well as contributions from non-linear bulk effects described above. Figure 47 shows a two-terminal I-V curve for MC-B in the $I_{15}V_{15}$ measurement configuration at 295 K, which was typical of most two-terminal measurements. Figure 47 also shows the two-terminal I-V curves for MC-A at three different temperatures for measurement
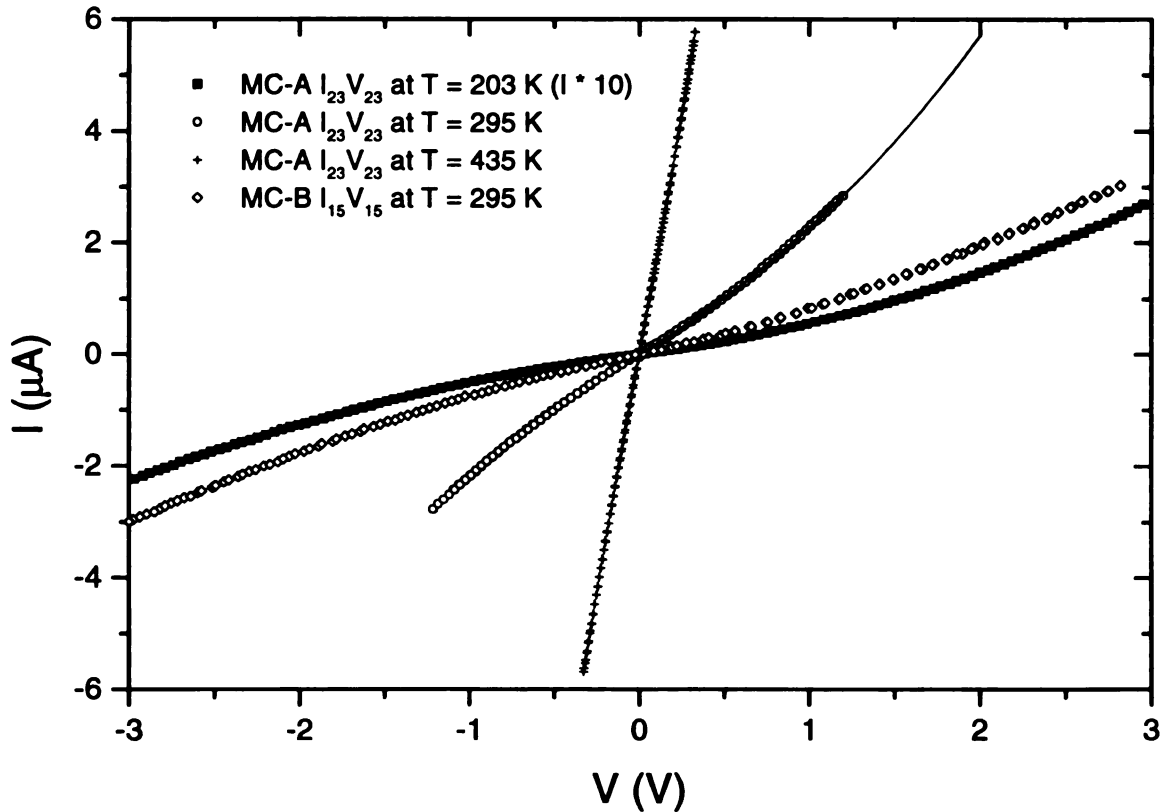
Figure 47 Two-terminal I-V curves for diamond microcrystal samples MC-A and MC-B.

configuration $I_{23}V_{23}$, corresponding to the four-terminal current contacts shown in Figure 46 above. For these curves the current depends exponentially on the voltage as might be expected for the current density J for an ideal forward-biased metal-semiconductor contact given previously by Equation 7. A fit to Equation 7 is shown for the 295 K data for MC-A in Figure 47 to illustrate the voltage dependence, and very good agreement is observed. It should be noted, however, that the I-V curves for two-terminal measurements are not expected to conform to Equation 7 exactly since two-terminal measurements entail back-to-back metal-semiconductor contacts. One contact is forward biased while the other is reverse biased. The reverse-bias current density depends exponentially on the fourth root of the voltage,[125] so that the two-terminal voltage dependence is dominated by the forward-biased contact. This can be seen from the I-V characteristics of a single contact as illustrated in Figure 7 above. The barrier height could not be determined for contacts to the samples in this study because the actual current density was unknown due to large uncertainty in the effective contact pad area as discussed in the next section. It should be noted that contact linearity for HF-2 was improved from HF-1, perhaps because the oxygen RIE step was eliminated for the HF-2 contacts and contact surfaces were acid cleaned in separate solutions of aquaregia and buffered HF just prior to metallization.

3. RESISTIVITY

A. Multiprobe Resistance Contributions

For an arbitrarily shaped 3D object with four Ohmic contacts 1-4, there are 36 possible multiprobe resistances which can be measured from two, three, and four-terminal configurations. With two current contacts i and j, and two voltage contacts l and m, where $i, j, l, m = [1,4]$, the resistances are given by $R^{ij}_{lm} = V_{lm}/I_{ij}$. For example, the two-terminal resistances are R^{ij}_{ij} with $i \neq j$, and a three-terminal resistance might be R^{ij}_{im} with $i \neq j \neq m$. A matrix can be formed from these 36

resistances where each resistance has coordinates (I_{ij}, V_{kl}). Such matrices are shown in Table 8 for sample HF-2 and in Table 9 for sample MC-B for resistances measured near room temperature. Arranging the indices properly places the two-terminal resistances (bold) along the main diagonal, the four-terminal resistances (underlined) along the diagonals of the upper right and lower left submatrices, and the three-terminal resistances in the remaining positions. Arranged this way, the elements are expected to be symmetric about the main diagonal.[126]

For a material with isotropic bulk resistivity and four Ohmic contacts, the resistances in the matrix are assumed to be represented by the four contact resistances in series with a resistance due to the voltage drop across the volume of the diamond. Two-terminal resistances contain two contact resistances and a bulk resistance. The four-terminal resistances, however, contain only a resistance due to the bulk, since the voltage drop between the voltage contacts does not include the voltage drop across the two current contacts (ie. no current flows through the voltage contacts for a four-terminal resistance measurement.) Since all 36 resistances are made up of linear combinations of the four unknown contact resistances and a bulk resistance which is directly proportional to the resistivity, it can be shown[126] that only 6 of the 36 matrix elements are independent. There are, however, several such sets of 6 independent elements, and all the other elements in the matrix can be reconstructed from any such set. The most convenient independent set from an experimental point of view are the six two-terminal measurements. *This means that, assuming the bulk and contact resistances can be added in series, all four contact resistances and the bulk resistance of a 3D object can be obtained from the 6 possible two-terminal resistance measurements without performing a four-terminal measurement!* This analysis can be extended to higher dimensional systems or systems with greater than four contacts.

Such resistance tables were constructed from constant temperature measurements for the two microcrystallite samples as well as for the homoepitaxial film sample. Asymmetries in the resistance tables are attributed to non-Ohmic or asymmetric I-V characteristics for the contacts,

Table 8 Multiprobe resistance matrix (kΩ) for contacts 3, 4, 5, and 6 for HF-2 at 296.0 K. (See Figure 38 for contact geometry.)

$V_{kl} \backslash I_{ij}$	I_{56}	I_{53}	I_{54}	I_{34}	I_{64}	I_{63}
V_{56}	**149.20**	76.14	55.23	<u>-20.87</u>	-90.63	-70.40
V_{53}	76.30	**162.20**	66.07	-92.50	<u>-9.90</u>	83.03
V_{54}	53.51	66.30	**141.10**	72.08	83.11	<u>10.97</u>
V_{34}	<u>-20.90</u>	-93.36	72.65	**168.60**	93.12	-72.20
V_{64}	-91.58	<u>-9.91</u>	83.69	92.53	**177.80**	81.17
V_{63}	-70.91	83.66	<u>10.98</u>	-72.00	80.85	**156.80**

Table 9 Multiprobe resistance matrix (kΩ) for contacts 1, 2, 4, and 5 for MC-B at 293.1 K. (See Figure 39 for contact geometry.)

$V_{kl} \backslash I_{ij}$	I_{12}	I_{14}	I_{15}	I_{45}	I_{25}	I_{24}
V_{12}	**849**	392	370	<u>-20</u>	-471	-450
V_{14}	386	**4293**	389	-4207	<u>192</u>	3255
V_{15}	369	587	**1543**	920	1126	<u>221</u>
V_{45}	<u>-18</u>	-3032	917	**4846**	943	-3026
V_{25}	-451	<u>203</u>	1114	935	**1644**	663
V_{24}	-423	3240	<u>212</u>	-4190	654	**3996**

which had a resistance comparable to that due to the bulk diamond. The resistances in Table 8 for HF-2 where the contacts were Ohmic are very symmetric about the diagonal. The resistances in Table 9 for MC-B where the contacts exhibited non-linear I-V behavior, however, show some asymmetry about the diagonal except for the four-terminal measurements which are independent of contact resistance contributions.

B.   Film Resistivity from the van der Pauw Method

The temperature-dependent resistivities of the film samples, HF and PF, were obtained from four-terminal resistances using the van der Pauw technique for thin samples (thickness << lateral dimensions).[127] The van der Pauw method is applicable only for flat three-dimensional samples since its derivation is based on the technique of conformal mapping of two-dimensional fields. For a sample with four contacts labeled consecutively counter-clockwise, the resistivity ρ is given by

$$\rho = Cd \left[\frac{R_{12,34} + R_{23,41}}{2} \right] f$$

where d is the sample thickness, f is a function of the ratio $R_{12,34}/R_{23,41}$, and the four-terminal resistances are $R_{ij,kl} = |V_{kl}|/I_{ij}$ for current leads i and j and voltage probes k and l.[128] The constant C is a geometrical factor given by $C = 2\pi/\ln(2)$ for thin samples with contacts near the edge. C should increase from this value for samples with contacts which extend inward from the film edge. A geometrical factor correction of +6% was estimated for the measurements on HF-2 to correct for the fact that two of the contact pads (5 and 6) were located more than $0.3r_o$ inward from the film corners, where r_o is the radial distance from the center of the film to a corner.[129] The American Society for Testing Materials standard F 76 dictates standardized techniques for van der Pauw measurements on semiconductor samples.[130]

C.   Microcrystallite Resistivity

i.   Resistance

The temperature-dependent four-terminal resistances for configuration $I_{23}V_{14}$ for MC-A and for configuration $I_{15}V_{24}$ for MC-B are shown in Figure 48 on a semi-log plot. This is the first such data for isolated diamond microcrystallites. Both crystallites show a change of several orders of magnitude in resistance within 100 degrees of room temperature and both exhibit nearly the same slope. The resistances were also > 1 MΩ at temperatures below -50 °C.

ii.   Resistivity of 3D Samples from Multiprobe Resistance Measurements

a.   Overview

The van der Pauw method cannot be used to interpret the resistance measurements on microcrystallite samples since they have aspect ratios near 1. In this case, obtaining the resistivity of microcrystallites from multiprobe resistance measurements requires a more extensive analysis to obtain the geometrical factors which relate each measured bulk resistance value to the resistivity of the crystallite. Geometrical factors for three dimensional objects can be calculated analytically, such as for the standard long cylindrical resistor where $R = \rho(l/A)$, but the calculations become unwieldy for all but the most elementary geometries. A numerical technique for calculating the geometrical factors for multiprobe resistance measurements on arbitrarily shaped objects with uniform resistivity was therefore developed in collaboration with Mike Thorpe[131], Sangil Hyun[132], and Roy Day[133] for interpreting the microcrystallite data. The analysis includes reconstructing the 3D crystallite and contact geometry, finite element analysis to model the current flow and obtain the geometrical factors for measurement geometries, and fitting to obtain the bulk resistivity and, optionally, the contact resistances.
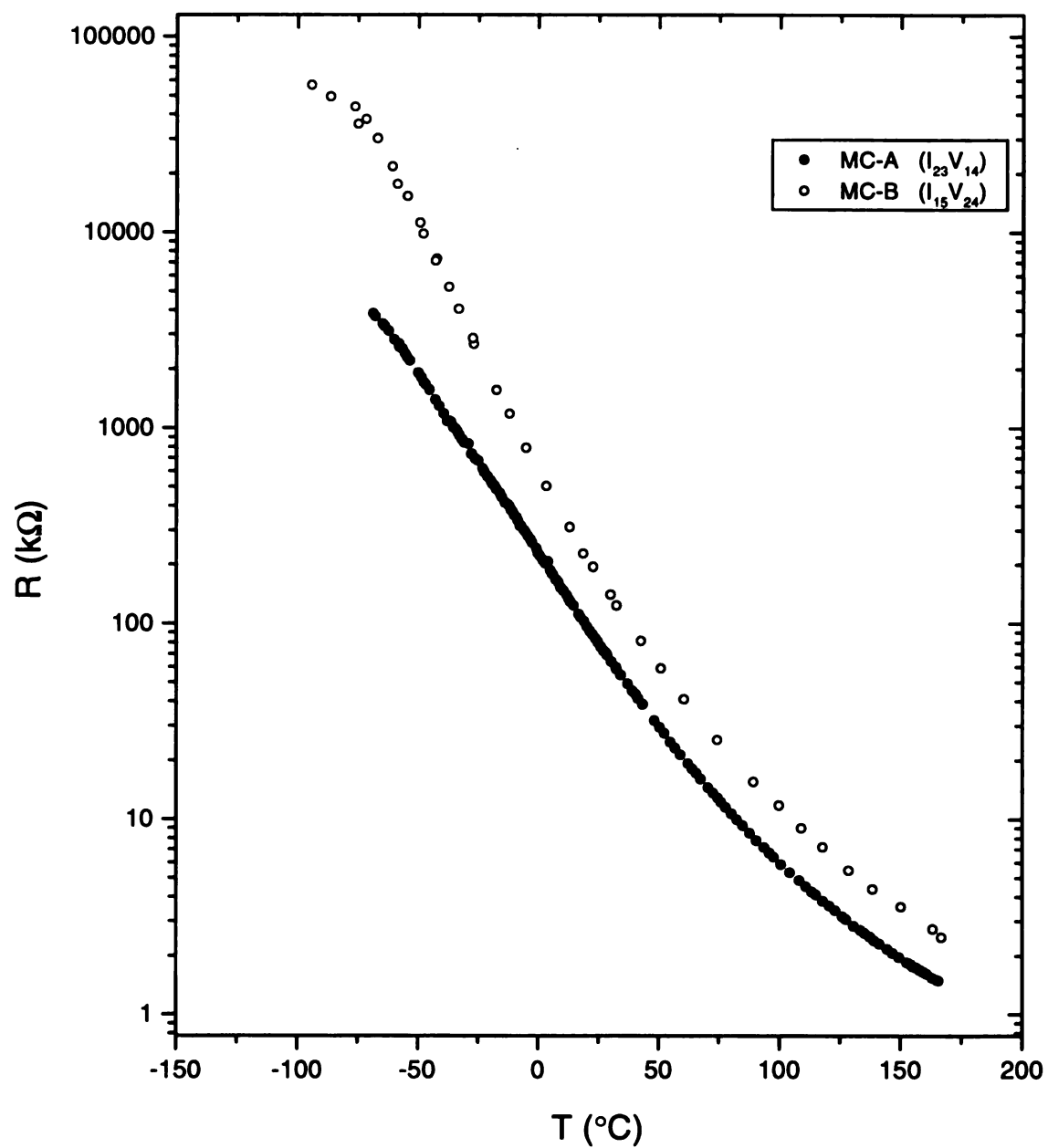
Figure 48 Four-terminal resistance vs. temperature for microcrystals.

b. Geometry Reconstruction

For each crystallite a three dimensional image was reconstructed from SEM photographs of the crystallite from five different viewing directions—one from straight down $\theta = 0°$ (normal incidence to substrate) and four views at $\theta = 50°$ with azimuthal views of $\phi = 0°$, 90°, 180°, and 270°. A set of such micrographs appears in Figure 34. These photos over-sampled the 3D geometry of the crystallite, but provided better accuracy for the reconstruction since all major crystallite facets were recorded at least once at less than a 45° angle. The SEM micrographs were digitized using a scanner attached to a PC and the vertex coordinates of each facet and contact pad corner measured in arbitrary units using the computer cursor while viewing the image using Corel "PHOTO-PAINT." Facets were assumed to contact the substrate smoothly, ignoring slight undercuts. This introduced little error since the crystallite bottoms have low current density compared to the crystallite tops on which the contacts create a high current density. The arbitrary length units were converted to actual lengths by means of the SEM scale bar in the image. The scale, coordinates, and viewing angles for each photo were input into a minimization routine[134] which returned the coordinates for the optimized 3D geometry of the crystallite and contact pads. The routine minimizes the total χ^2 given by

$$\chi^2 = \lambda_l \chi^2_{lengths} + \lambda_f \chi^2_{facets} + \lambda_a \chi^2_{angles}$$

where λ_l, λ_f, and λ_a are weighting factors and χ_{facets} and χ_{angles} are given by

$$\chi^2_{facets} = \sum_i \left[\alpha x_i + \beta y_i + \gamma z_i - \delta \right]^2$$

$$\chi^2_{angles} = \sum_j \left[\Theta_j^{calculated} - \Theta_j^{theory} \right]^2$$

$$\Theta^{calculated} = \cos^{-1}(\hat{n}_1 \cdot \hat{n}_2)$$

Here (α, β, γ) are the direction cosines of the facet normals n_i and Θ^{theory} are the ideal angles between known facets (eg. (111) and (100) facets form a 54.7° angle). The dominant degrees of

freedom are in the vertex coordinates $\bar{x}$, though the weighting factors can be changed to emphasize a particularly well-known aspect of the geometry. Typically λ_l is the largest since the vertices of each facet edge length are measured directly from the photographs. The minimization forces the facets to be planar and reconstructs the crystallite shape first. The contact pads are then reconstructed with the constraint that they must lie on the surface of the reconstructed crystallite. For well-shaped crystallites with observably flat facets such as shown in Figure 26, the reconstructed angles between facets agreed with the ideal angles to within 1°.

c.   Finite Element Analysis for Current Density and Geometrical Factors

Finite element analysis (FEA) is used to model the current flow and obtain the geometrical factors for independent contact configurations on the reconstructed geometry.[135] Commercially available FEA software[136] was used to create a 3D mesh which divided the crystallite into several thousand four-sided pyramidal volume elements defined by four mesh vertices. An arbitrary height coordinate was added to the otherwise 2D contact pads so that they could also be defined as pyramidal volume elements, each with one side in contact with the crystallite surface. Usually 5 to 10 such volume elements were used to define each contact pad. The number of total volume elements used was typically greater than 3,000 and was essentially limited by available computer memory. Increasing the total number of volume elements increases the accuracy of the result by shrinking the mesh size, but the results for typical crystallite geometries did not change significantly when more than 3,000 volume elements were used. Figure 49 shows sample MC-B with such a mesh. The FEA packages are designed to solve for heat flow in an isotropic 3D object. This is equivalent to the problem of current flow in an isotropic medium. Poisson's equation $\nabla^2 \Phi(x, y, z) = 0$ is solved within each volume element subject to the boundary conditions that (1) no current flows into or out of the sample boundary, and (2) the contact pads are perfect conductors at constant potential. The conductivity is also normalized to 1 for the calculation since
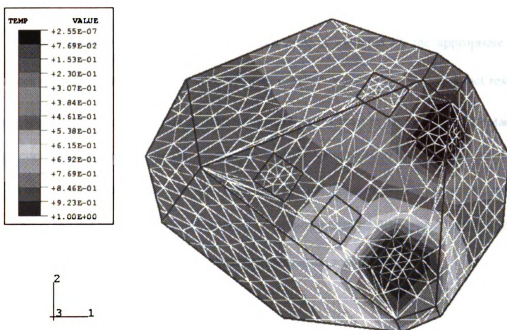
Figure 49 Calculated potential distribution on the surface of microcrystallite MC-B for the I_{15} geometry. The mesh used for finite element analysis is also shown.[137]

the length scale of the geometry is arbitrary. The potential of each contact pad is determined by its role in the multiprobe measurement being modeled. For example, for a four-terminal resistance measurement using current contacts 1 and 3 and voltage probes 2 and 4, contact 1 could be set at 1 V, contact 3 at 0 V, and contacts 2 and 4 allowed to float. The potential distribution on the surface of a crystallite as modeled for such a geometry is depicted in Figure 49. The output of the FEA is the value of the potential at each mesh node and, more importantly, the value of the multiprobe resistance normalized to unit conductivity for the measurement geometry under consideration. The entries of the 36 element table formed by these normalized resistances are the geometrical factors G_{ij} mentioned above for each measurement geometry. In reality, the calculation need be performed for only the six two-terminal geometry elements since the other 30 elements of the table can be reconstructed from these as mentioned above.

d.   Obtaining the Resistivity and Contact Resistances

Each resistance in the measured resistance table is modeled by the appropriate contact resistances r_{ci} and bulk resistances $R_{ij} = G_{ij}\rho$ in series $R_{ij}^{theory} = \rho G_{ij} + r_{ci} + r_{cj}$. Contact resistances are only included for measurements in which a contact pad is used as both a current contact and a voltage contact, since the voltage drop across the contact contributes to the total measured voltage drop. For a sample with four contacts there are six independent resistance equations with 5 unknowns: ρ and the four contact resistances. The unknowns can be determined by minimizing the χ^2 for the measured resistances and the theoretical resistances according to

$$\chi^2 = \sum_{i,j} \left(R_{ij}^{meas} - R_{ij}^{theory} \right)^2$$

The preferred method, however, was to use the four-terminal measurements alone to provide the most accurate value for the bulk resistivity since they are independent of the contact resistances. This resistivity value was then held fixed while the contact resistances were optimized using the six equations obtained from the two-terminal geometries. The resistivities obtained directly from each of the six four-terminal equations $R_{ij} = G_{ij}\rho$ without using minimization typically agreed to better than 0.05% of the mean value when the sample temperature was held stable to 0.25 °C while the resistance values were measured. The discrepancies were of order 2% for temperature drift of at most a degree. Asymmetric non-Ohmic contacts can be modeled similarly by measuring resistance values for both forward and reverse current sense to build two resistance tables with double the number of contact resistances to include r_{ci} and r_{ci}'.

This geometrical analysis was performed for both microcrystallite samples and for the homoepitaxial film. Results for the homoepitaxial film were checked against van der Pauw results and found to agree to within 5.5%. An example of a table of calculated *geometrical factors* for the resistance due to sample appears in Table 10 for microcrystal MC-B. It should be emphasized that

these geometrical factors are independent of the contact resistances, and their calculation assumes that the contacts do not affect the resistivity of the bulk sample.

The geometrical factors in this table were obtained from data taken at a single temperature, though they remain valid for all temperatures as long as the sample resistivity remains isotropic and the contacts do not introduce appreciable effects such as large space-charge regions. The temperature-dependent sample resistivity can therefore be obtained by scaling data from a four-terminal resistance vs. temperature measurement by the appropriate geometrical factor obtained from data recorded at a single temperature. The temperature-dependent resistivities of the microcrystals were obtained in this manner. For this study, however, the geometrical factor of interest was obtained by dividing the measured resistance by the resistivity obtained from all six four-terminal measurements, rather than using the calculated geometrical factor obtained directly from FEA. To obtain the temperature-dependent resistivity of microcrystal MC-A, the temperature dependence of $R_{23,14}$ was measured over -80 °C < T < 170 °C and then scaled by the geometrical factor 1435 cm^{-1} obtained from resistance table data taken at 162 °C. Similarly, for MC-B the temperature dependence of $R_{15,24}$ was recorded over roughly the same temperature range and scaled by the geometrical factor 3304 cm^{-1} obtained from analysis of multiprobe resistance measurements at 20.5 °C. The four-terminal resistance geometries used for these measurements were chosen so as to maximize sensitivity to longitudinal resistance. Resistance data for MC-A was taken at higher temperature than for MC-B because the MC-A contacts were more Ohmic at the higher temperature than at room temperature.

Table 10 Geometrical factors (μm^{-1}) for bulk resistance of microcrystallite MC-B. Contact number labels correspond to those shown in Figure 40. (Contact 3 was not used.)

$V_{kl} \setminus I_{ij}$	I_{12}	I_{14}	I_{15}	I_{45}	I_{25}	I_{24}
V_{12}	**1.08249**	0.63363	0.60485	<u>-0.02869</u>	-0.47766	-0.44888
V_{14}	0.63358	**1.41784**	0.94397	-0.47366	<u>0.31035</u>	0.78431
V_{15}	0.60489	0.94400	**1.41123**	0.46707	0.80637	<u>0.33913</u>
V_{45}	<u>-0.02869</u>	-0.47384	0.46726	**0.94073**	0.49602	-0.44518
V_{25}	-0.47759	<u>0.31036</u>	0.80638	0.49577	**1.28403**	0.78801
V_{24}	-0.44891	0.78421	<u>0.33912</u>	-0.44497	0.78801	**1.23320**

D.   Contact Resistance Results

Contact resistances were obtained by the geometrical analysis described above for the two MC samples and the HF sample. The analysis for the contact resistances for MC-A was very difficult and exhibited much uncertainty as a result of asymmetric non-Ohmic behavior and lack of data to fill a full resistance matrix for both forward and reverse current sense. The contact resistances were in the range of 10 to 1,000 kΩ. The analysis was much improved for MC-B, however, due to complete data and more linear I-V characteristics. The contact resistances for contacts 1, 2, 4, and 5 to MC-B had room-temperature resistances of approximately 150 kΩ, 300 kΩ, 3,000 kΩ, and 700 kΩ, respectively, but showed variation for forward and reverse current. The room-temperature contact resistances for contacts 3, 4, 5, and 6 to HF-2 were identical to within ±0.3 kΩ for forward and reverse current due to their highly linear I-V characteristics, and had values of 64.1 kΩ, 57.6 kΩ, 35.7 kΩ, and 52.5 kΩ. The contact resistance for annealed Ti/Au

contacts to B-doped diamond in this study does not scale with the inverse of the contact area. The microcrystal contacts had areas of 0.18 μm^2 and the contacts to HF-2 had areas of 9×10^{-4} cm^{-2}. The areal resistivity is the product of the contact resistance and the area $\rho_a = R * area$. The resulting areal resistivity for microcrystal contacts was therefore on the order of 2×10^{-3} Ω-cm^2 and that for the homoepitaxial film was on the order of 50 Ω-cm^2. Since the areal contact resistivity is not constant and independent of contact area, it was concluded that electrical contact occurs non-uniformly across a contact, and perhaps only at isolated spots within the physical contact area. This is a common feature of large area metal-metal contacts. The error introduced in the above geometrical analysis by assuming isotropic areal contact resistivity for such pin-point contacts is small for small contacts spaced far apart, but can be appreciable for contacts for which the contact dimensions are of the same size as the contact separation. A signature for such error would be inconsistency among the bulk resistivity values of an isotropic sample obtained by the geometrical analysis from each of the four-terminal resistances. The error introduced by this concern in the analysis for the MC samples and the HF sample is deemed small since the resistivity values for each sample obtained from the geometrical analysis of the six four-terminal measurements for each sample showed agreement to within a few percent.

E.   Resistivity Results

Figure 50 shows the temperature-dependent resistivities for the film samples as obtained by van der Pauw analysis and for the two microcrystallite samples as obtained by the geometrical analysis described above. In the figure legend, HF-1 and HF-2 refer to the homoepitaxial film data acquired using the first and second set of contacts, respectively. PF-1 and PF-2 refer to the polycrystalline film data before and after annealing the contacts. MC-A and MC-B refer to data for the two microcrystals. The data has been plotted on a semi-log plot vs. 1000/T because the resistivity covers several orders of magnitude. Exponential temperature dependence, such as for

thermally activated processes $\propto \exp(E/kT)$, thus appears as straight lines. The error bars for each curve due to random uncertainties are smaller than the data markers, roughly $\pm 5\%$ or less, except for the PF data for which the uncertainty is of order $\pm 13\%$ due to a large uncertainty in the film thickness.

All samples display a change in resistivity by several orders of magnitude over the temperature range shown. The temperature dependence of the resistivity for the microcrystal samples is qualitatively identical to that of the resistance shown in Figure 48, since the resistivity is just the four-terminal resistance scaled by the appropriate geometrical factor. The data for microcrystal MC-A shows very broad curvature below room temperature and also above about 360 K, though the sign of the concavity is different in the two regions. The data near and just below room temperature approximately fall along a straight line in Figure 50. The data for MC-B in Figure 50 shows obvious low temperature curvature only below about 250 K, and only slight curvature of the opposite sign above 360 K. The data for the intermediate temperature region falls along a straight line.

The data for HF-1 and HF-2 overlap in Figure 50, even though they were taken in different temperature-control systems. Below room temperature the data for this sample appear to follow a straight-line on this plot, while slight curvature is apparent above about 285 K where the resistivity is below 10 Ω-cm. The PF-1 and PF-2 data also overlap, indicating that the polycrystalline film resistivity was unaffected by the contact annealing treatment. This is evidence against claims[84,85] of the resistivity of CVD diamond being affected by hydrogen passivation of traps in the bulk diamond. These data show very broad curvature above and below room temperature with a different sign of the concavity in the two temperature regions. The data follow a straight line in Figure 50 from roughly 260 K to 360 K, which is between the regions of obvious curvature.

The resistivities of the two microcrystals are nearly the same despite their differences in geometry, suggesting that the current modeling analysis is correct and that the visible twin defect in
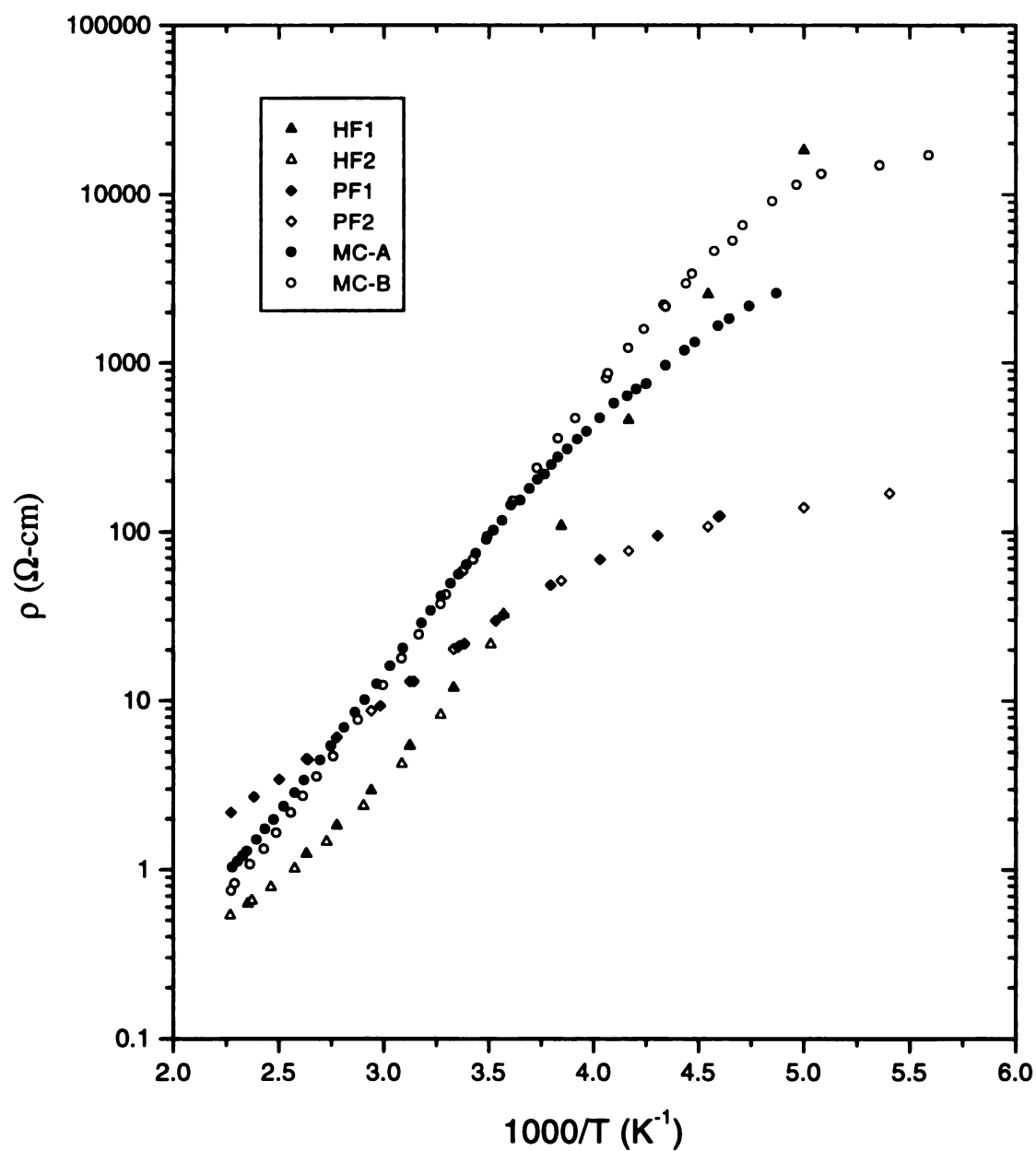
Figure 50 Resistivity vs. inverse temperature for diamond samples grown under identical conditions.

MC-B does not dramatically affect the crystallite resistivity by, for example, depleting a large number of carriers. Also, the microcrystallite resistivities are generally higher than that of the homoepitaxial and polycrystalline films near room temperature.

Near room temperature, the microcrystals and the homoepitaxial film exhibit similar resistivity slope on the semi-log plot, while the polycrystalline film resistivity exhibits a noticeably smaller slope. The two microcrystals and the polycrystalline film show curvature on this plot at low temperature, while the homoepitaxial film shows no sign of low temperature curvature down to 200 K. Of the two substrate types represented by the four samples, the samples grown on oxidized Si show less curvature to higher temperatures in the data of Figure 50 than the one sample grown homoepitaxially on diamond. This most dramatic difference is between the nominally single-crystal samples: the microcrystals show an onset of high temperature curvature above roughly 360 K, and the homoepitaxial film shows onset above about 285 K.

4.   HALL COEFFICIENT FOR DIAMOND FILM SAMPLES

The Hall coefficients for the homoepitaxial and polycrystalline films were obtained from Hall-effect measurements using the van der Pauw method.[127,128] Hall effect measurements were
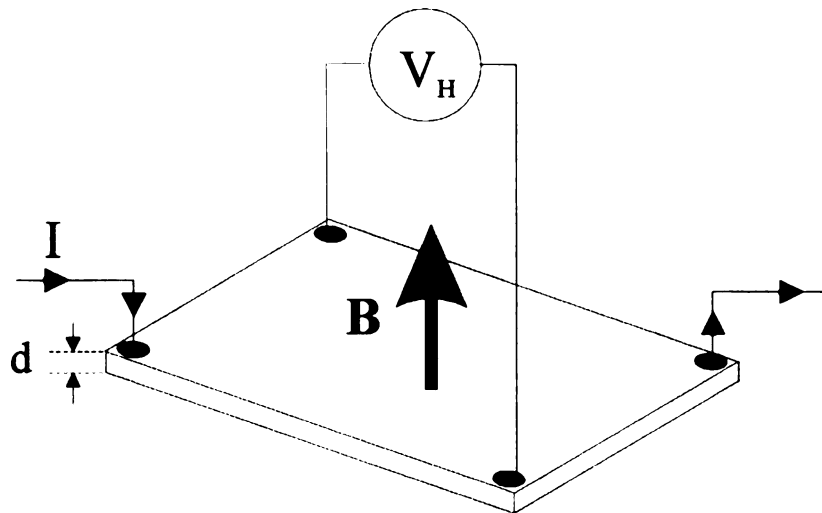
Figure 51 Geometry for Hall-effect measurements on thin square samples of thickness d.

conducted by placing the film samples in a magnetic field perpendicular to the film surface and measuring the voltage difference between contact probes located transverse to the current flow as shown schematically in Figure 51. For symmetrical specimens, this voltage is particularly sensitive to the transverse misalignment of the voltage probes since any misalignment allows sampling of the voltage drop parallel to the current flow. Thermal emf's can also cause offset voltages of a few μV. These effects were compensated for by recording the Hall effect voltage as the voltage change caused by turning the magnetic field B on at constant sample current and temperature. Another method used was to record the Hall effect voltage as half the voltage change for measurements in

+B and -B, or $V_H = \dfrac{[V(+B)+V(-B)]}{2}$. Discrepancies between the two methods for the samples

measured were less than 1%. The van der Pauw method gives the Hall coefficient R_H as

$R_H = \dfrac{d}{IB}(\Delta V)$, where ΔV is the voltage change just described, I is the measurement current, d is

the sample thickness, and B is the magnetic field. For an isotropic material, ΔV is typically measured for the two transverse geometries possible for a four-terminal measurement and the Hall coefficient taken as the average of the Hall coefficient for the two experiments. This was the method used for this study. The American Society for Testing and Materials further recommends conducting measurements in positive and negative current sense and calibrating the voltage drop using a standard resistor, resulting in 10 measurements.[130] Discrepancies between measurements taken in positive and negative current sense were negligible for these samples, and the Hall coefficients calculated for both transverse geometries typically differed by less than 5% for PF-2 and less than 1% for HF-1. A linear Hall response to magnetic fields was confirmed up to 1 Tesla for HF-1 at 200 K and at 380 K and for PF-2 at 220 K. Hall effect measurements at zero and ±1 Tesla magnetic fields were used to calculate the Hall coefficients.

The temperature dependence of the Hall coefficient for HF-1 and PF-2 are shown in Figure 52. The HF-1 data drops by four orders of magnitude from 200 K to 380 K. The PF-2 data shows a
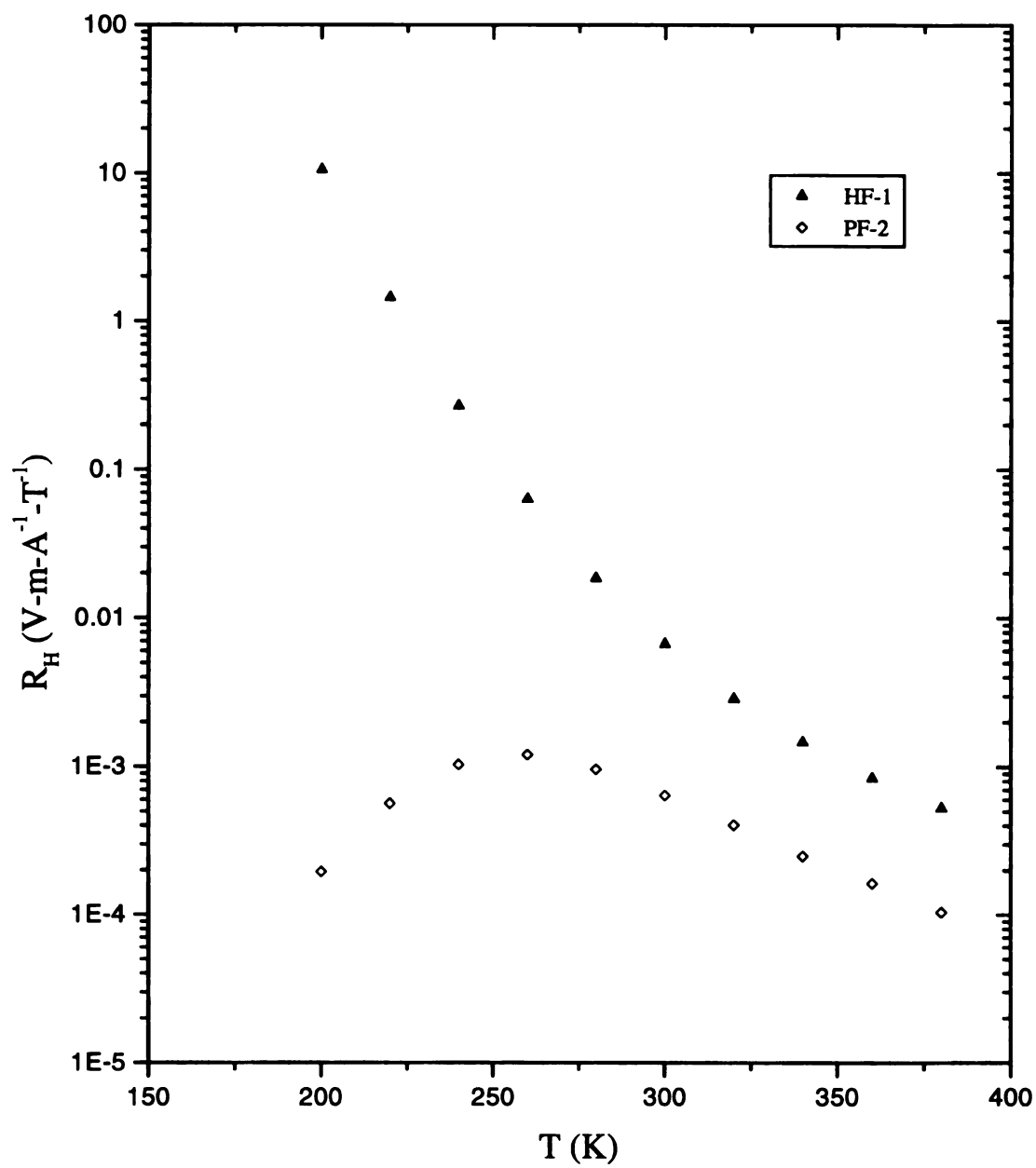
Figure 52 Hall coefficient for HF-1 and PF-2 obtained by the van der Pauw method.

maximum around 260 K with a sharp drop below that temperature. Above 260 K the HF-1 and PF-2 data have approximately the same temperature dependence, though the absolute magnitudes of the Hall coefficient differ by a factor of 10.

5. CARRIER CONCENTRATION FOR DIAMOND FILM SAMPLES

In general, the Hall coefficient is related to the carrier concentrations p (holes) and n (electrons) by

$$R_H = r_H \frac{1}{q} \frac{p - b^2 n}{q(p + bn)^2}$$

where q is the electronic charge, $b \equiv \mu_n/\mu_p$ is the ratio of the drift mobilities for electrons and holes, and $r_H \equiv < \tau^2 >/< \tau >^2$ for τ the mean free time between carrier collisions. The factor r_H is known as the Hall scattering factor and is equal to $3\pi/8 = 1.18$ for phonon scattering and $315\pi/512 = 1.93$ for ionized impurity scattering.[138] The carrier concentration and type can be obtained from the Hall coefficient as long as one type of carrier dominates. A positive Hall coefficient indicates p-type carriers (holes) dominate. For the case $p \gg n$,

$$R_H = r_H \left(\frac{+1}{qp} \right)$$

The Hall coefficient was positive for both HF and PF, indicating that p-type conductivity dominated in the boron-doped diamond, as expected. Assuming that $p \gg n$, the hole concentrations for PF-2 and HF-1 were calculated from the Hall coefficients using the above expression. A value of $r_H = 1$ was used since the nature of the carrier scattering is unknown. The carrier concentrations are significantly different in the two samples, as shown in Figure 53. The carrier concentration in the polycrystalline film is roughly an order of magnitude larger than in the homoepitaxial film above room temperature, and shows a minimum near 260 K while the homoepitaxial film shows no evidence for such a minimum down to 200 K.
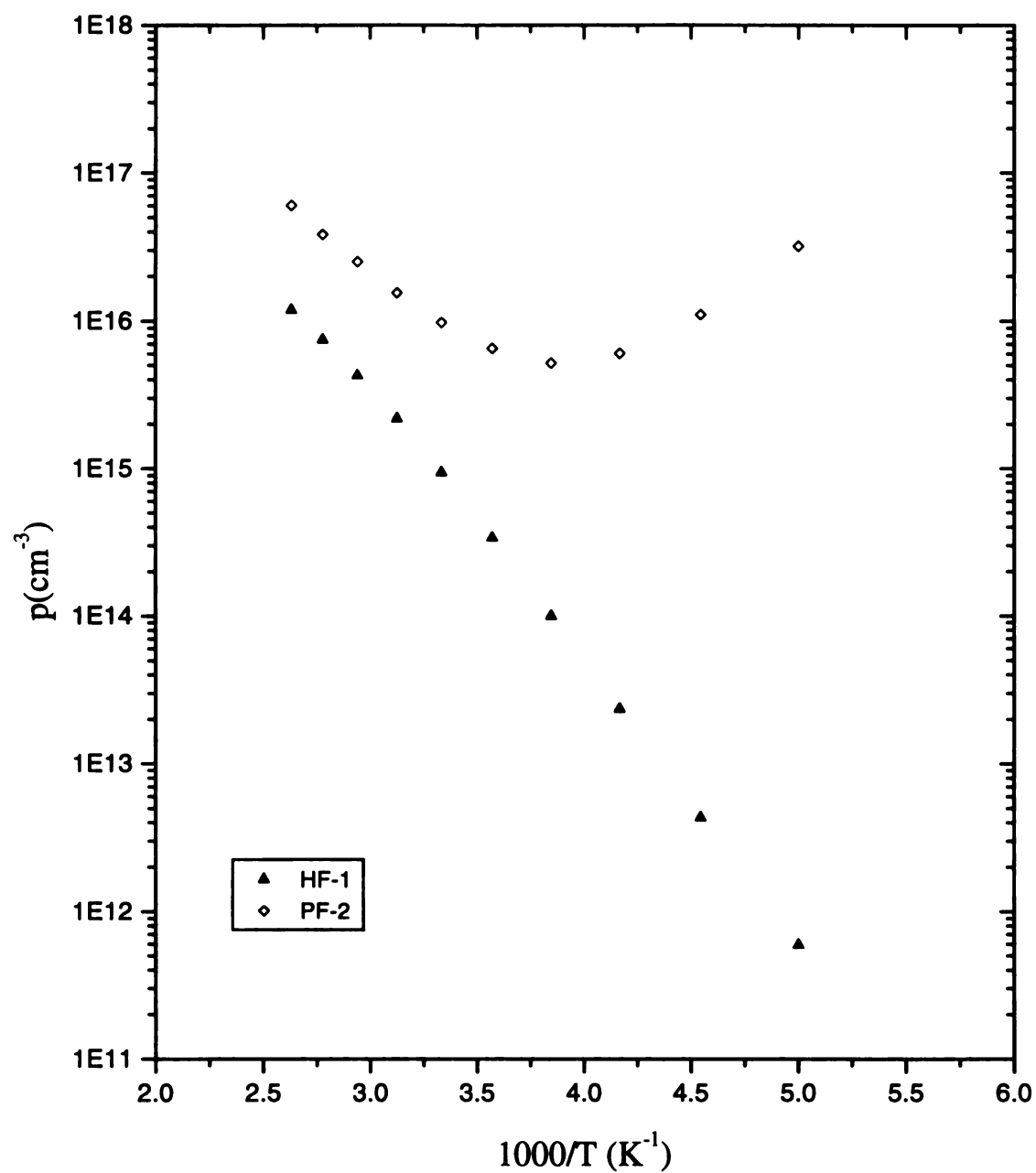
Figure 53 Hole concentrations from Hall effect for samples HF-1 and PF-2.

6. HALL MOBILITY FOR DIAMOND FILM SAMPLES

The Hall mobility μ_H is defined as the product of the Hall coefficient and the conductivity

$$\mu_H \equiv |R_H \sigma| = |R_H|/\rho .$$

The Hall mobilities for HF-1 and PF-2 were calculated from their temperature-dependent Hall coefficients and resistivities, and the results are shown in Figure 54. Again, a substantial difference in behavior exists between the homoepitaxial and polycrystalline films. The homoepitaxial film exhibits a Hall mobility near 600 cm^2/V-s which is relatively temperature independent below room temperature. The polycrystalline film exhibits a Hall mobility near 30 cm^2/V-s at an obvious maximum near room temperature with a sharp drop at lower temperatures.

The Hall mobility is related to the drift mobility μ of the carriers (single species) by the Hall factor r_H, $\mu_H = r_H \mu$. Assuming a Hall factor of ~1, even the homoepitaxial film shows a hole drift mobility which is about half that in natural diamond, namely ~ 1700 cm^2/V-s. (See Table 5.) The hole mobility in the polycrystalline film is even lower.

In principle, measuring the temperature dependence of the Hall mobility gives insight into the scattering mechanism and, therefore, the value of r_H, so that the carrier drift mobility can be determined from the above expression. For example, ionized impurity scattering is predicted to produce $\mu \sim T^{+3/2}$, and scattering by acoustic phonons is predicted to produce $\mu \sim T^{-3/2}$. In practice, however, the Hall mobility usually does not exhibit a clean enough temperature dependence to unambiguously identify a specific scattering mechanism. Interpretation of the Hall-effect when a hopping conduction process dominates involves the theory of small polarons since the electrons are in localized states. Interpretation of the results can then be quite complicated since under certain circumstances holes can give a negative Hall coefficient and electrons can give a positive Hall coefficient.[139]
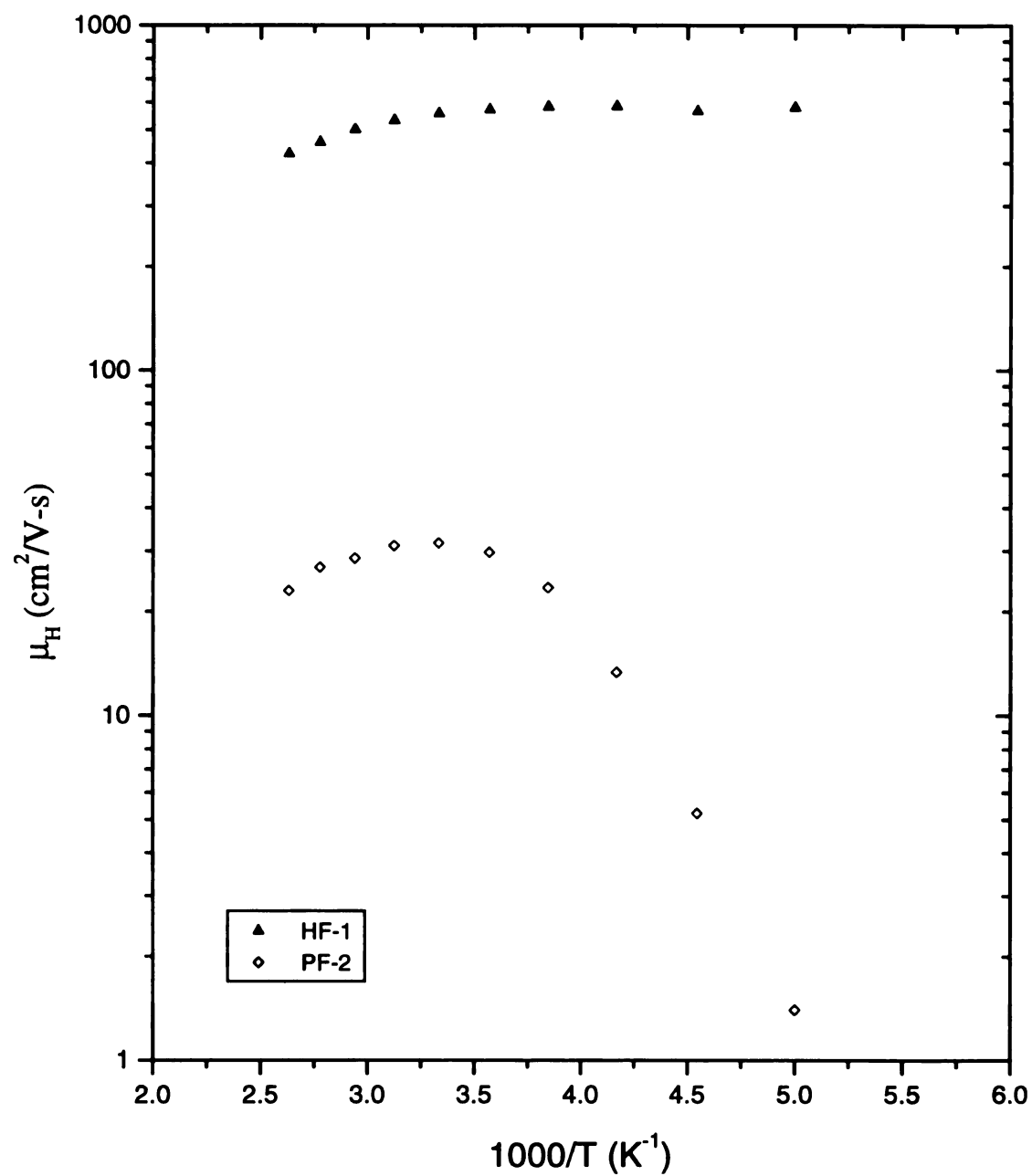
Figure 54 Hall mobility for samples HF-1 and PF-2.

7. ANALYSIS

A.   Resistivity—Fit to Model for Lightly Doped Semiconductors

Some of the resistivity data shown in Figure 50 extend over enough temperature range to show evidence for the knee expected at the cross-over between impurity conduction freeze-out at intermediate temperatures and hopping conduction at low temperatures. This behavior was introduced in Chapter II.4. (See Figure 2, p. 13.) Only the HF sample data shows no sign of curvature down to 200 K. The low temperature curvature in the PF data and the MC-A data is broad compared to that of the MC-B sample.

The resistivity data for PF-2, MC-A, and MC-B were inverted to give conductivity, $\sigma = \rho^{-1}$, and fit to the expected temperature dependence for this knee given in Equation 8, p. 14. The conductivity model is composed of two activated terms,

$$\sigma = \sigma_1 \exp(-E_1/kT) + \sigma_3 \exp(-E_3/kT)$$

which correspond to the two conduction mechanisms discussed earlier in Chapter II.5. Temperature was the independent variable and the fitting parameters were σ_1, σ_2, E_1, and E_2. The fits were over the temperature range $T < 370$ K, where the conductivities showed no sign of high-temperature saturation. The data points were weighted inversely to their magnitude as $1/\sigma_i$ to add weight to the few low-temperature data points which are presumably below the cross-over. The results are shown in Figure 50 as continuous lines through the data markers, and have been extrapolated to lower temperature than the data points. The prefactors, σ_1 and σ_3, and the activation energies, E_1 and E_3, are listed in Table 11. The fit to the MC-B data was difficult at low temperature since only a few data points extend into the temperature region where hopping conduction dominates. Data was also the most difficult to acquire at the lowest temperatures due to the high resistance of the samples.   The   cross-over   temperatures   listed   are   defined   as   the
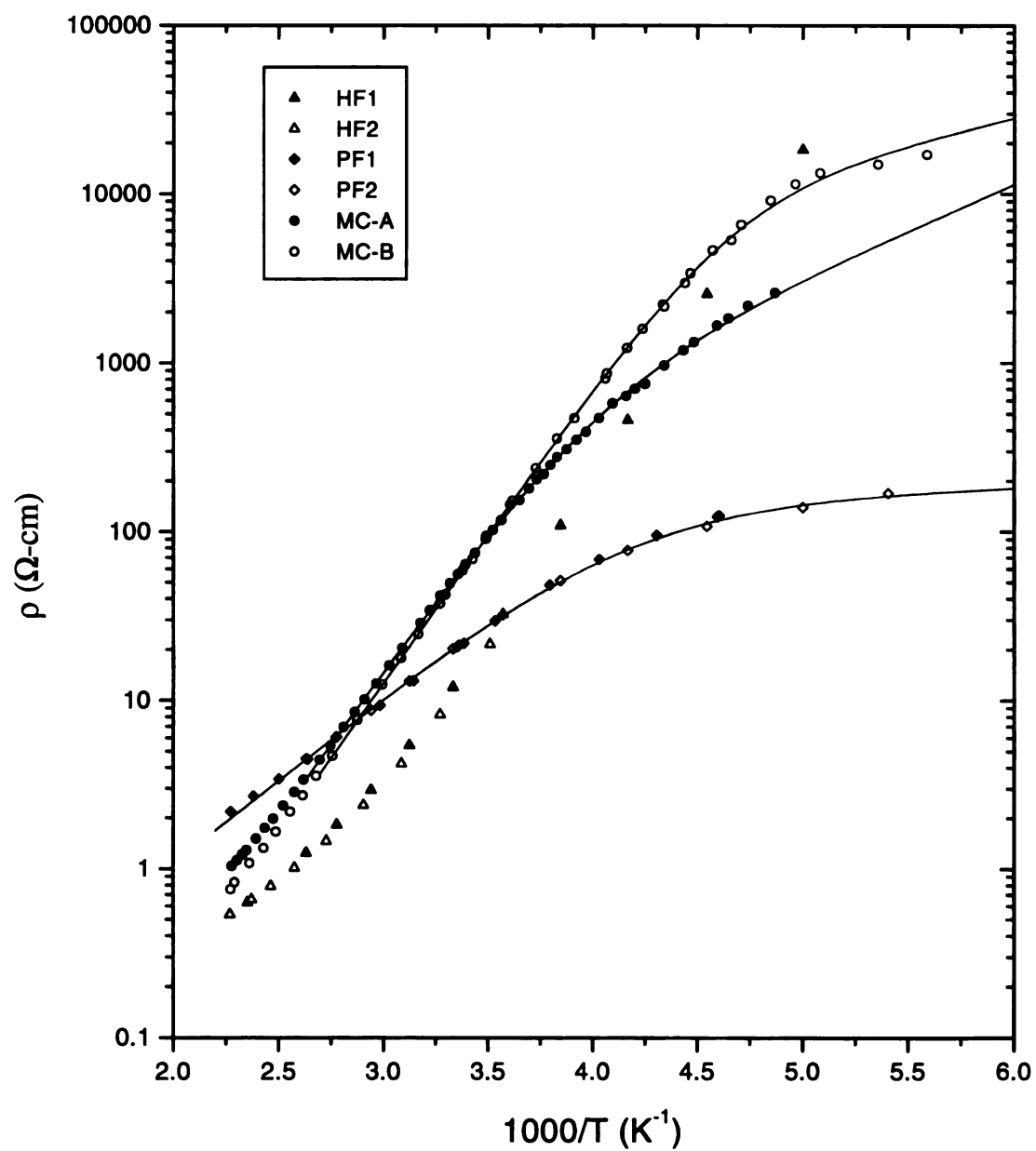
Figure 55 Resistivity vs. 1000/Temperature with fits.

Table 11 Fit results to conductivity model with two activated conductivity terms for data in Figure 55.

Sample	Cross-Over Temperature (K)	σ_1 $(10^2\,\Omega^{-1}\,cm^{-1})$	E_1 (eV)	σ_3 $(10^{-4}\,\Omega^{-1}\,cm^{-1})$	E_3 (eV)
MC-A (Microcrystal)	249	114±4	0.347±0.001	1711.9±345	0.109±0.004
MC-B (Microcrystal)	214	163±5	0.351±0.001	21.8±17	0.059±0.014
PF-1 (Polycrystalline Film)	241	0.95±0.12	0.199±0.004	102±6	0.0089±0.009

temperature at which contributions from the two conduction mechanisms are equal. The energies E_1 for the high-temperature valence band conduction mechanism are in very good agreement for the two microcrystals. The E_3 energies which correspond to the low-temperature hopping mechanism show greater disagreement, though the fit results are less accurate in this region because there are fewer data points. The cross-over temperatures for the MC-A and MC-B samples differ by 35 degrees, and the PF cross-over temperature is intermediate between the two. The cross-over temperatures, however, will be affected by the accuracy of the σ_3 and E_3 fit parameters. The values for the cross-over temperatures correspond to the extreme high-temperature end of the regions of obvious low-temperature curvature in Figure 55. The corresponding cross-over temperature for the HF sample, if it exists, must therefore be at or below the 200 K minimum range of the HF-1 data. The uncertainties in Table 11 are the uncertainties from the data fits.

B. Carrier Concentration—Fit to Model for Partially Compensated p-type Semiconductor

The expression for the carrier concentration p in a partially compensated p-type semiconductor was given by Equation 7. The temperature dependent carrier concentration data for HF-1 and PF-2 were fit to this expression by assuming a value of 1.07 for the effective mass of holes m^* from Reference 115 and a value of 4 for the valence band degeneracy g since diamond has two doubly degenerate hole bands. The data were fit in the high temperature region where valence band conduction is believed to be the dominant conduction mechanism. For HF-1, this corresponded to the entire data range from 380 K down to 200 K. For PF-2, only the 5 data points between 380 K and 300 K were believed to be in this range. The fit results are shown graphically as solid lines through the data points in Figure 53 and the values of the fitting parameters N_A, N_D, and E_a are listed in Table 12 along with the calculated compensation ratio K = N_D/ N_A. The uncertainties are from the fits.

The fit results indicate that the HF sample has insignificant compensation, less than 1%. The acceptor ionization energy E_a is consistent with the 0.35 eV activation energy for E_1 conductivity in the microcrystals from Table 11. The results for the PF sample appear unreasonable, since the compensation ratio is much lower than expected and the ionization energy is significantly higher than expected from the E_1 value of 0.199 eV in Table 11. The results for the polycrystalline film could be due to fitting the data at too low a temperature, so that valence band conduction is not the dominant process. As can be seen in Figure 56, the fit was performed in a region where there is still much curvature in the data due to low temperature effects.

Table 12 Hole concentration fit results using a model for a partially compensated semiconductor.

Sample	N_A (10^{18} cm^{-3})	N_D (10^{18} cm^{-3})	K (N_D/ N_A)	E_a (eV)
HF-1	1.23±0.09	0.01078±0.00069	0.009	0.351±0.004
PF-2	119±57	10^{-4}	8×10^{-7}	0.416±0.015
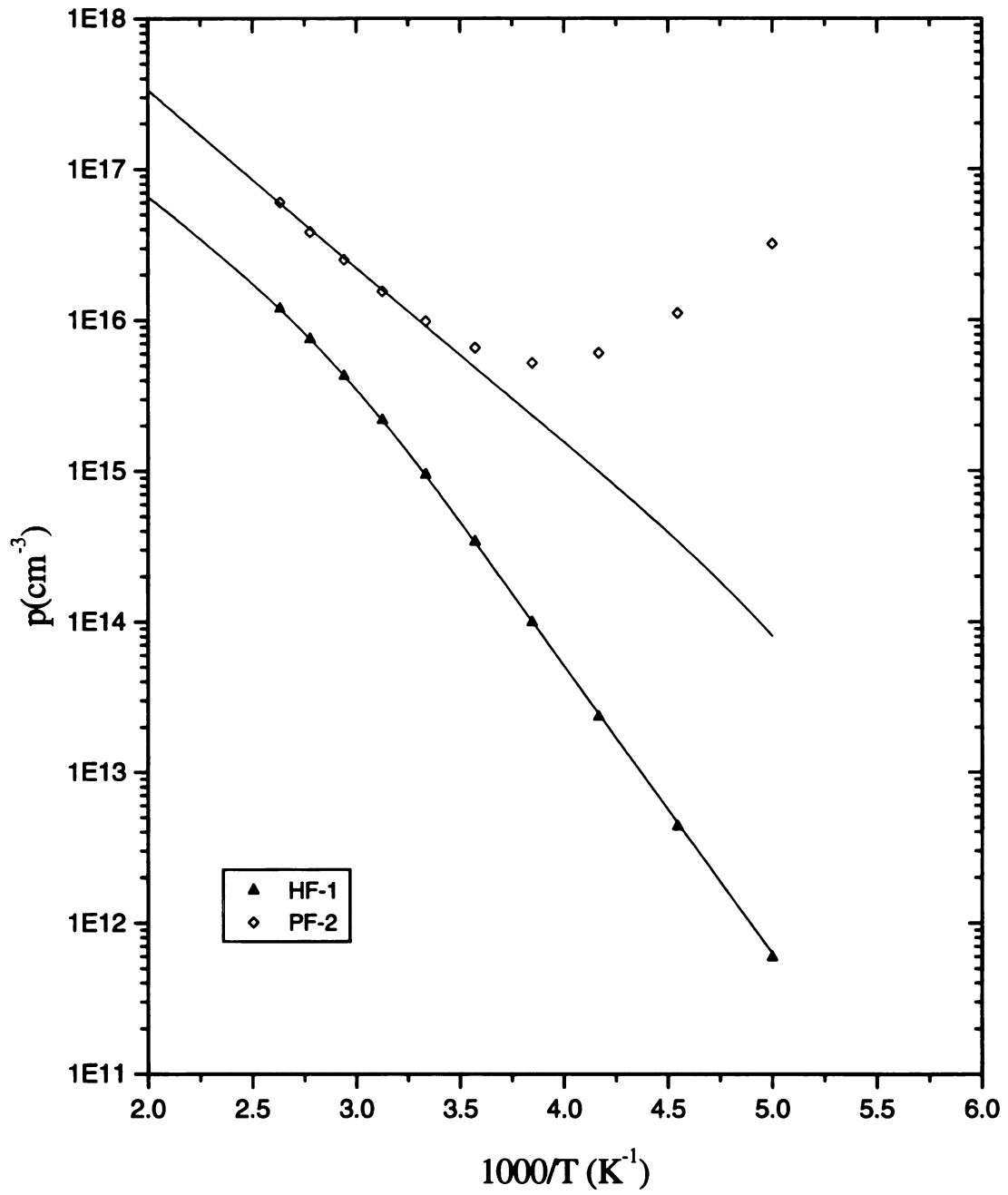
Figure 56 Hole concentration data and fits to expression for partially compensated *p*-type semiconductor.

The B concentrations for the HF and PF samples are not known since they were not directly measured using a technique such as secondary ion mass spectroscopy (SIMS). It is therefore not possible to compare N_A from the fits to the measured B concentrations of the films to get a measure of the fraction of B impurities acting as dopants.

C.   Comparison with Other Studies

The results of this study are consistent with those of Malta *et al.*[1] who studied large area diamond films that were also grown at Kobe Steel using the same technique and similar conditions to those of this study. They compared the electrical transport properties of simultaneously grown single-crystal, polycrystalline, and highly oriented doped diamond films grown homoepitaxially. They measured the resistivity, Hall mobility, and hole concentration of four sets of films with different B doping concentrations, and fit their results to the same models employed in this study for a lightly doped, partially compensated semiconductor. The Malta *et al.* data for the third sample set was reproduced in Figure 23, Figure 25, and Figure 24, and is the data for their films which most closely compare in resistivity to the HF and PF films of this study. The resistivity, carrier concentration, and mobility data for the present study in Figure 50, Figure 53, and Figure 54 show the same qualitative temperature dependence as the Malta *et al.*[1] data, which covers a larger temperature range and shows the cross-over between the two conduction mechanisms more clearly.

Malta *et al.*[1] also interpreted the knee in resistivity occurring just below 200 K in their films as indicative of a cross-over from a low-temperature variable-range hopping process to a higher-temperature valence band conduction process. This interpretation predicts a corresponding minimum in the carrier concentration at the same temperature, which is observed near 263 K in the PF-2 data shown in Figure 53 as well as their data. This minimum is expected to occur at the knee temperature just above the transition temperature between the two conduction mechanisms, which for the PF sample is 241 K from Table 11. (The apparent increase in p at low temperatures is due to

failure of the model for the Hall effect in the hopping conduction regime. The actual carrier concentration is not expected to increase at low temperature.) The p data for HF-1 in Figure 56 does not extend to low enough temperatures to show such a minimum, and the resistivity data for HF-1 in Figure 50 does not show evidence of a knee down to 200 K. This is not unexpected, since the Malta et al.[1] data for a similar homoepitaxial film shows the cross-over occurring near 170 K, just below the range of HF-1 data obtained.

Malta et al.[1] analyzed their data using the same model equations as are used in this study. The values for the fit parameters of this study are compared to those for Malta et al. in Table 13 for fits to the conductivity and Table 14 for fits to the carrier concentration. The conductivity fit parameters for the two studies for the valence conduction regime agree fairly well, with the greatest discrepancy observed for the polycrystalline films. Poor agreement between conductivity fit parameters for hopping conduction probably arises because the results for the present study are less accurate in this regime. Only a few data points at the lowest temperatures measured in the present

Table 13 Conductivity fit results for present study from Table 11 compared to Malta et al.[1]

Sample	Cross-Over Temperature (K)	σ_1 $(10^2\,\Omega^{-1}\,cm^{-1})$	E_1 (eV)	σ_3 $(10^{-4}\,\Omega^{-1}\,cm^{-1})$	E_3 (eV)
MC-A (Microcrystal)	249	114±4	0.347±0.001	1711.9±345	0.109±0.004
MC-B (Microcrystal)	214	163±5	0.351±0.001	21.8±17	0.059±0.014
PF-1 (Polycrystalline Film)	241	0.95±0.12	0.199±0.004	102±6	0.0089±0.009
HF (Homoepitaxial Film)	—	—	—	—	—
HMD3[†] (Homoepitaxial Film)	170	489	0.377	0.00633	0.017
HOD3[†] (Highly Oriented Film)	215	9.65	0.311	1.33	0.020
PD3[†] (Polycrystalline Film)	225	1.59	0.266	6.4	0.025

[†]Samples from Malta et al.[1]

Table 14 Fit results to carrier concentration for present study from Table 12 compared to those from Malta *et al.*[1]

Sample	N_A (10^{18} cm^{-3})	N_D (10^{18} cm^{-3})	K (N_D/N_A)	E_a (eV)
HF-1	1.23±0.09	0.01078±0.00069	0.009	0.351±0.004
PF-2	119±57	10^{-4}	8×10^{-7}	0.416±0.015
HMD3[†] (Homoepitaxial Film)	1.1	0.030	0.03	0.351
HOD3[†] (Highly Oriented Film)	1.1	0.15	0.13	0.312
PD3[†] (Polycrystalline Film)	4.8	0.63	0.13	0.285

[†]Samples from Malta *et al.*[1]

study show evidence of hopping conduction as the dominant mechanism. This decreased accuracy also affects the cross-over temperatures.

The fits to the carrier concentration show excellent agreement for the homoepitaxial samples of each study. As mentioned earlier, the fit results for PF-2 are unrealistic because the data were fit in a temperature regime where valence band conduction did not dominate conduction sufficiently to satisfy the assumptions of the model.

8. DISCUSSION

The data show differences among the transport properties of microcrystals, homoepitaxial films, and polycrystalline films. These differences are presumably associated with differences in film morphology, since the samples were grown either simultaneously or under identical conditions. The unique feature of the present study is that the resistivity for the isolated microcrystals, MC-A and MC-B, is the first data for single-crystal CVD diamond on non-diamond (oxidized Si) substrates. The important physical differences between the samples to keep in mind while comparing the electrical behavior are the following: (1) The microcrystals are considered single-crystal diamond grown on oxidized Si and can be compared to the single-crystal homoepitaxial

film. (2) The microcrystals are considered representative of the single-crystal material within each grain of the polycrystalline film since both the microcrystals and the polycrystalline film were grown on similarly prepared oxidized Si substrates. (3) The microcrystals and polycrystalline film were grown on oxidized Si and the homoepitaxial film was grown on (100) natural diamond. (4) All samples were grown under identical conditions, though the polycrystalline film was grown in a separate run from the homoepitaxial film and the microcrystals. (5) The microcrystals and the polycrystalline film exhibit both (111) and (100) facets, while the homoepitaxial film exhibits essentially only a single (100) facet which is the top face of the film.

The most significant result from the resistivity data is seen by comparing the activation energies of the samples for valence band conduction. The activation energy for the two microcrystals, 0.347 ± 0.001 eV and 0.351 ± 0.001 eV, obtained from the fit to the resistivity (Table 11), is the same as the acceptor ionization energy of 0.351 ± 0.004 eV for the homoepitaxial film, which was obtained from a fit to its hole concentration under the assumption of partial compensation (Table 12). However, the activation energy 0.199 ± 0.004 eV for the polycrystalline film, obtained from the fit to the resistivity (Table 11), is significantly smaller than the activation energies for the microcrystals or the homoepitaxial film. The results from the fit to the hole concentration for the polycrystalline film appear unrealistic and therefore will not be used.

The activation energy of a dopant is determined by its bonding in the host's crystalline environment. The important result that the acceptor activation energy is the same for the microcrystals and the homoepitaxial film implies that B impurities are incorporated in similar structural environments in the three single-crystal samples. Thus, substrate differences appear not to significantly affect the structural incorporation of B during growth, at least as far as homoepitaxial diamond compares to diamond on oxidized Si. However, as shown in Figure 49, transport measurements on the microcrystals are sensitive primarily to the top region of the crystallites near the contact pads, since the current density is highest there. The current density is

low near the interface with the substrate, so transport effects due to SiC layers or high stress regions near the interface will play a minor role in the microcrystal measurements if their influence is limited to the first few tenths of a micron distance from the substrate.

The lower activation energy observed in the polycrystalline diamond film must be caused by grain-boundaries, since we have shown that doping properties in the absence of grain boundaries are similar to single-crystal diamond. Dopant activation energy can be lowered by disorder in local bonding at grain-boundaries caused by lattice misorientation, defect migration, impurity segregation, and over-all higher impurity concentrations due to higher dopant incorporation rates during growth. The disorder created by these phenomena will, in general, broaden the impurity level so that carriers need only be excited to the low-energy edge of the band to ionize an acceptor atom. This creates an effective ionization energy which is the energy difference between the bottom of the broadened band and E_V. Malta et al.[1] measured the B concentrations in their samples using SIMS and found that *polycrystalline* films incorporated 2-4 times more B than simultaneously grown *homoepitaxial* films. Thus, higher B concentrations at grain-boundaries are a strong possibility and may play a leading role as a source of impurity level broadening.

The second interesting comparison from the data is that the two microcrystals exhibit similar resistivities over a temperature range from 250 K to 440 K, and that this resistivity is higher than the homoepitaxial film resistivity by over a factor of 2 in the temperature region where valence band conduction dominates. The resistivity is determined by the concentration p and drift mobility μ, and is given by $\rho = (q\mu p)^{-1}$ when n-type transport is neglected. This assumption is valid for at least the HF sample, since its compensation ratio is small. The effects due to p and μ cannot in principle be separated from the resistivity alone. Mobility data was unavailable for the microcrystals, but we may speculate about its role in determining their resistivity based on mobility observations for the homoepitaxial film. The mobility of the homoepitaxial film is roughly temperature independent in the valence band conduction temperature regime. The temperature

dependence of the resistivity in the homoepitaxial film is therefore dominated by changes in the carrier concentration. Since the microcrystals display the same temperature dependence of the resistivity as the homoepitaxial film, it is likely that the mobility of the microcrystals is also temperature insensitive in the valence band conduction regime. This line of argument predicts that the higher resistance of the microcrystals is thus due either to a lower overall doping concentration or a smaller, essentially temperature-independent, mobility.

The differences in resistivity may be due to differences in B incorporation during growth for different crystal facets. Diamond (111) surfaces incorporate higher B concentrations than (100) surfaces when grown in the same CVD run.[140] The homoepitaxial films were grown on (100) diamond substrates and have negligible (111) surface area during growth, but the microcrystals and the polycrystalline films exhibit both (111) and (100) surfaces. The homoepitaxial film is expected to possess a lower B concentration and therefore to exhibit a higher resistivity compared to the microcrystals. This is contrary to observation, so we conclude that differences in B incorporation due to film morphology are not the cause of this discrepancy. This refutes speculation[1] that greater B incorporation rates observed in polycrystalline films with (100) and (111) facets compared to simultaneously deposited (100) homoepitaxial films are due to the differences in growth surfaces, and supports a picture in which B is preferentially incorporated at grain boundaries.

B levels in the much smaller grain boundary volume must be large to explain the factor of 3 difference in boron levels between simultaneously grown homoepitaxial and polycrystalline films observed by Malta et al.[1] by secondary ion mass spectroscopy (SIMS). It has also been observed that high B doping levels ($\geq 10^{18}$ cm^{-3}) broaden the impurity band in diamond and reduce the observed activation energy. The observed activation energy is reportedly reduced to 0.2 eV at a B concentration of approximately 3×10^{18} cm^{-3}.[141] It is therefore plausible that conduction processes in polycrystalline films are dominated by highly doped grain-boundary regions with a lower activation energy than the lower doped regions in the nearby bulk diamond. This simplistic picture must of

course be modified to include the band broadening effects of increased disorder at grain-boundaries and possibility effects of carrier depletion or addition between the differently doped grain-boundary and bulk diamond volumes.

The resistance of diamond can also be affected by strain. The microcrystals and polycrystalline film were grown on oxidized Si and are therefore strained, while the homoepitaxial film is not strained. Internal stress in diamond films is caused by various sources such as impurities (eg. Si), structural defects such as dislocations, and interactions across grain boundaries.[60] Anisotropic elastic strain causes bond lengths and angles to distort, thereby affecting the band structure and the effective mass of carriers. The strain in a thin diamond film grown on oxidized-silicon can be obtained from the film stress as measured by the shift of the diamond Raman peak from 1332 cm^{-1}. Knight and White[57] measured a shift of +5 cm^{-1} for diamond on SiO_2 glass and interpreted this as corresponding to an internal stress of +2.1 GPa, where the positive sign indicates a film in compression. Bergman et al.[60] measured the thermal and internal stress of polycrystalline films grown on (100) Si by different methods, and found internal compressive stresses ranging near 0.23 GPa which correlate roughly with relative concentrations of graphitic phase carbon. In Si, compressive stress (negative) shifts the light-hole band up in energy relative to the heavy hole band, causing a *decrease* in resistivity.[142] This neglects effects on the effective mass due to changes in curvature of the bands. If diamond behaves similarly to Si in this respect, then internal stress does not account for the higher resistivity of microcrystals on oxidized Si compared to homoepitaxial diamond, since the predicted effect of *decreased* resistivity is contrary to the observed *increased* resistivity.

The above discussion points to a picture in which the structural environment of B acceptors in the grains (microcrystals) comprising a polycrystalline film is identical to that for single-crystal homoepitaxial film. The B acceptor level in diamond is therefore unaffected by strain effects due lattice mismatch with oxidized Si, at least to within the sensitivity of the microcrystal measurements

in ths study. The higher resistivity for microcrystals compared to homoepitaxial diamond is unexplained by internal strains or higher B concentration in diamond with (111) facets. B acceptors in polycrystalline diamond, however, must exist not only in the single-crystal environment within each grain, but also in a very different structural environment within grain boundaries where disorder and much higher dopant concentrations are expected to play a role.

Chapter VII

CONCLUSIONS AND FUTURE RECOMMENDATIONS

The results from the resistivity measurements on isolated diamond microcrystals are the first electronic transport data for *single-crystal* CVD diamond on oxidized Si substrates, and the first of their kind for transport measurements on isolated 3-dimensional micron-sized crystallites. The microcrystal resistivity obeyed a model of thermally activated valence band conduction due to B acceptors above 240 K, with evidence for a cross-over to variable-range hopping conduction below that temperature. The activation energy observed for valence band conduction in microcrystals on oxidized Si had an average value of $E_a = 0.349$ eV, which was indistinguishable from that of simultaneously-deposited homoepitaxial diamond, $E_a = 0.351$ eV. This result showed that substrate differences between (100) diamond and oxidized Si do not noticeably affect the crystalline environment of B acceptors in single-crystal CVD diamond films. Polycrystalline diamond on oxidized Si, on the other hand, exhibited a lower activation energy of 0.199 eV. By measuring isolated diamond grains, this research showed that this lower E_a was conclusively due to the presence of grain boundaries, and not to possible intragrain differences associated with different substrates. B in polycrystalline films therefore also exists in a structural environment associated with grain-boundaries that is very different from that in single-crystal material.

Although the resistivity temperature dependence for microcrystals and single-crystal homoepitaxial diamond was similar in the valence band conduction regime, the measured resistivity of microcrystals was two times higher than that of single-crystal homoepitaxial diamond. This difference was contrary to expectations that microcrystals should have higher B concentrations than simultaneously deposited (100) homoepitaxial films due to differences in growth surface morphology. The higher resistivity was also unexplained by higher lattice strain in microcrystals due to mismatch with the non-diamond substrate (oxidized Si). The resistivity difference was

141

speculated to be due either to lower doping concentrations or smaller temperature independent mobility for microcrystals on oxidized Si. This was based on observations of similar resistivity temperature dependence for microcrystals and homoepitaxial diamond and a roughly temperature independent mobility measured in single-crystal homoepitaxial diamond.

The above results, in combination with observations by Malta *et al.*[1] that 2-4 times more B is incorporated in polycrystalline films than in simultaneously deposited homoepitaxial films, suggest that B concentrations are much higher in grain boundaries than in the single-crystal material comprising grains. High dopant concentrations ($\geq 10^{18}$ cm^{-3} in diamond),[76] disordered bonding, or a combination of the two at grain boundaries could act to broaden impurity levels and produce the lower effective activation energy observed for valence band conduction in polycrystalline films.

The next logical step towards understanding electronic transport in polycrystalline diamond involves measurements of single grain boundaries as shown in Figure 29. Such measurements will allow investigations of the activation energy for B acceptors and the density of states within grain boundaries.

Little is known about the origins of compensating carriers in diamond films. This could be investigated by repeating the above resistivity measurements for simultaneously deposited crystallites, (111) and (100) homoepitaxial films, and polycrystalline films of several doping levels to temperatures well below the cross-over from valence band conductivity to hopping conductivity. Differences in compensation affecting the variable-range hopping mechanism would be exhibited as systematic shifts in the cross-over temperature between conduction mechanisms. The insight provided by such a study could possibly lead to the discovery of a method of producing *n*-type diamond by exploiting the electrical properties of defects.

Specific questions remain regarding how B dopants are electronically incorporated in grain boundaries. Does the acceptor level merely broaden with concentration as for single crystal material or is the effect more strongly dependent on the degree of structural disorder as long as a

critical number of dopant species is present? Does the B tend to cluster at grain boundaries or is it uniformly distributed as, for example, with the density of broken bonds? Studies of isolated grain boundaries would provide the most direct and quantitative answers to these questions, though much could first be learned from studies of very highly doped films ($> 5 \times 10^{18}$ cm^{-3} B concentration). For example, a first question is whether the metal-insulator transition, predicted to occur above 10^{20} cm^{-3},[143] occurs at the same B concentration for polycrystalline films as for (111) and (100) homoepitaxial films. A significant difference between polycrystalline films and homoepitaxial films would again point to higher dopant incorporation at grain boundaries.

The experimental techniques developed in this research proved successful for measuring the electronic properties of diamond microcrystals, and would also enable the studies of isolated grain boundaries mentioned above. Diamond proved a very difficult material to contact, due to the difficulty of forming Ohmic contacts to a relatively inert, wide bandgap semiconductor. The electrical contacts and leads fabricated in this work intentionally had dimensions ≥ 0.2 μm, since alignment error between successive lithographic steps was of that order. In principle, the technique could be scaled down in size to nearly the limits of electron-beam lithography, which are < 0.05 μm. Substrate topography and crystal height must also be within the limits for planarization by thin film technology, roughly < 10 μm height for sharply sloped steps.

The lithographic contact technique should prove invaluable for measurements of other materials for which large single-crystal material is unavailable, such as organic conductors, superconductors, or other wide bandgap semiconductors. The most obvious microcrystalline materials of interest are ones which can be grown or deposited on substrates, though loose crystals could be embedded in polymer films with the top facets protruding to hold the crystals in place and to provide a planarized contact surface. Other measurements should be enabled as well, such as Hall-effect, thermopower, and thermal conductivity. The technique would be especially adaptable to thermal measurements, since submicron heaters and thermocouples can be defined by

lithography and since the electronic current density analysis for 3D structures used in this study is

identical in form to that for thermal transport.

APPENDICES

APPENDIX A

APPENDIX A

CONTACT PROCESS DEVELOPMENT—DETAILED CONSIDERATIONS

1. POLYIMIDE FILM

Polyimide was used in this study as an insulating planarization layer for microfabrication. Polyimide is routinely used in industry for such purposes. It can be easily spin-applied, is highly insulating (10^{16} Ω-cm), and has a high dielectric breakdown voltage (157 V/μm).[144] When lightly cured it can be wet-etched using NaOH or photoresist developers. When fully cured it is thermally stable up to 500 °C and is chemically inert. It can still be patterned, however, using a dry reactive ion etch (RIE) incorporating an oxygen plasma. The polyimide used was PI-2555 Polyimide Coating by DuPont.[145] This product normally costs $600 for 500 g, but the DuPont Electronic Department provided a 500 g unit free of charge since only a small quantity was needed for trial purposes. They also provided one unit of VM651 Adhesion Promoter and one unit of polyimide thinner.

Initial experiments with polyimide consisted of characterizing suitable spinning, baking and etching parameters to provide the planarization layer. An off-shoot of this work was aimed at using electron-beam lithography to pattern submicron pits in a polyimide insulating layer to expose point-contact regions on the surface of a bismuth single-crystal. These exposed areas were then metallized and used for electron-focusing.[146] Details of that experiment appear in Appendix B.

An organosilane adhesion promoter was used in conjunction with the polyimide, since polyimide adheres poorly to silicon substrates on its own. Adhesion promotor solution consisted of 3 drops of VM-651 Adhesion Promoter by DuPont[145] with 50 ml of deionized water (DI). This solution was allowed to normalize at least 12 hours before use. Methanol was also tried as a solvent, but it gave poorer results than the DI solutions, possibly due to residues left by the

methanol itself. The DI solutions were discarded after 7 days, as recommended.[147] The adhesion promotor solution was spin applied to clean substrates at 5,000 rpm and then baked in a 140 °C preheated oven in an uncovered petri dish for 60 seconds to dry. The substrate was allowed to cool for 15 minutes before polyimide was spin-applied at 5,000 rpm for 60 seconds. For diamond crystallites 1 to 2.5 μm high, undiluted PI-2555 polyimide was used which spins to about 2.5 μm thickness on a planar surface. This completely covered the crystallites and planarized the surface.

Initially, a light polyimide cure consisted of baking the substrate for 30 minutes in a 140 °C preheated oven in a covered petri dish with an aluminum foil-lined bottom. It was easier to throw away the aluminum foil than it was to clean the petri dish if polyimide leaked over the edge of the substrate. This polyimide cure worked well on thick single crystals of bismuth and thin bismuth films on Si as mentioned in Appendix B, but did not work well for diamond crystallites on Si substrates. In the case of diamond on Si, this oven cure created a thin layer of polyimide, conformal to the crystallites and substrate, which was more resistant to wet-etching than the upper regions of the polyimide film. The planarized surface profile was not preserved when isotropically back-etching such films due to their anisotropic etch-resistance. It was suspected that the high thermal conductivity of diamond contributed to heat flow from the substrate into the polyimide film during the bake, ensuring that the etch-resistant layer would also cover the crystallites. Various schemes of reducing the thermal contact between the substrate and the foil-lined petri dish, varying the time and temperature of the bake, and varying the time and temperature of the wet-etch could not prevent the formation of this layer. The layer resisted etching even after 22 minutes in 0.25 N NaOH solution at 30 °C, while the less-cured region etched away in less than 6 minutes.

An infrared (IR) cure was then used to try to heat the polyimide more uniformly throughout its thickness. A 3.5 hour cure in a make-shift IR oven (Al-foil lined bricks with an IR lamp) produced a very light cure which allowed the polyimide film to etch isotropically. A mercury

thermometer with the bulb located near the substrates provided a very rough monitor of baking conditions and typically read 100 ± 5 °C during the IR bake.

Polyimide films in a partially cured state can be wet-etched by NaOH solutions or photoresist developers. Complete wet-etching or stripping of fully cured polymide was unsuccessful using either of these etchants, though one report claims accelerated etching of Kapton films using a heated solution of NaOH in ethanol. NaOH solutions were tried first and worked well for the electron focusing experiment, but not for diamond on silicon samples. The polyimide film seemed to soak up etchant and took on a jelly-like appearance when removed from the etchant. The films also tended to de-laminate in one big gooey blob. Photoresist developers were reported to produce a much more buffered etch,[144] so a diluted solution of Shipley MF-319 photoresist developer in DI was tried with IR baked samples. A solution of 1 part MF-319 developer to 10 parts DI held at 30.0 ± 0.5 °C with slow magnetic stirring produced good isotropic etches without attacking the structural integrity of the polyimide film. Sensitivity to this etch was high, however, as the IR bake produced only a very light polyimide cure. Polyimide films 2.5 mm thick were typically etched away in about 22 seconds. Polyimide etch rates are reported to be sensitive to the humidity and temperature history of the polyimide film. These parameters were difficult or nearly impossible to control adequately without a clean-room environment and varied drastically from season to season and from day to day. Etch times could only be calibrated very roughly by processing a bare silicon substrate in parallel with each diamond crystallite sample during the polyimide application steps, and using this substrate to check the time necessary to etch the polyimide film clean for the particular processing conditions. The diamond crystallite sample was typically etched for about 33% of this time to lower the planarized polyimide layer enough to expose the tops of the diamond crystallites. The etch for each diamond sample was fine-tuned by examining the sample at a 50° side-view in an SEM to observe the polyimide level relative to crystallites which were not targeted for electrical contact. Additional etching and SEM examination

continued as necessary until a polyimide profile such as that shown in Figure 35 was obtained. The etch did not appear to go linearly with time following the initial etch, however, so subsequent etches were typically just quick dips lasting a second or less.

It should also be noted that viewing partially cured polyimide in an SEM results in additional local curing so that viewed regions will actually resist the etch more than surrounding regions. For this reason, diamond crystallites targeted for electrical contact were not viewed during etch calibration. This may be useful in future applications, however, as a way of directly patterning polyimide films. Specifically, electron-beam writing can be done directly on partially cured polyimide films to imidize localized regions, and lesser imidized regions subsequently wet-etched away. This eliminates the need for application and patterning of a PMMA layer. Initial observations suggest micron-sized features with tapered edge profiles could be easily fabricated using this technique. The tapered profile is a consequence of the fact that the polyimide is altered by proximity-heating interaction with the electron beam, as well as perhaps being chemically altered by direct interaction with the high-energy electrons.

2. LITHOGRAPHY

The Nanometer Pattern Generation System (NPGS) software by Nabity[148] was used for all electron-beam writing. This software uses the DesignCAD[149] drawing software to generate linear arrays of single dots which are exposed, or "drawn", into poly-methyl-methacralate (PMMA) electron-beam resist on the sample using a JEOL-840A scanning electron microscope (SEM). Exposure parameters which are entered into a run file include the coarse electron-beam current setting of the SEM (for reference only), the actual measured electron-beam current, the SEM magnification setting, the dot-spacing, the line-width, and the area electron exposure in $\mu C/cm^2$. All beam writing was done at 35 kV accelerating voltage. For contacting crystallites with facets of order 1 μm in diameter, submicron alignment was required at several fabrication stages. The NPGS

software allows the use of alignment windows which define areas of minimum electron-beam exposure used for sampling non-critical substrate regions to look for alignment features. A custom designed cross-hair overlay displayed on the computer screen over the scanned image allows determination of an offset matrix to the resolution of the dot spacing in the alignment pattern. This alignment system was used in conjunction with 0.3 μm wide fabricated alignment marks to facilitate submicron alignment of the Ti/Au contacts on the crystal facets and alignment of the Au leads with the Ti/Au contacts.

The main developmental concerns associated with electron-beam lithography centered around alignment. The alignment software is limited in that it does not allow the user to specify the exposure per dot in the alignment pattern. Hence, the exposure per dot will be the product of the beam current (variable) and a fixed exposure time. The minimum beam current setting of the SEM was always used during alignment scans, though even this produced too high of a dose in some cases and resulted in highly exposed alignment scan dots. This did not typically occur for as thin as 0.25 μm thick PMMA on flat substrates, but it presented a huge problem when scanning across the tops of diamond crystallites where resist coatings were often thinner than this. Following PMMA developing, metallization, and lift-off, crystallites often looked like the one shown in Figure 57.

The greatest threat from alignment scan dots occurred during writing of alignment marks when the crystallite itself was scanned for alignment purposes. The substrate is devoid of polyimide at this point, so the resist is very thin on the top of the crystallite. Alignment scan dots were avoided by first using 950K PMMA resist with 7.5% solids, spun at 3,400 rpm to produce a resist layer approximately 2.5 μm thick. This layer was thick enough on the tops of most diamonds to prevent full exposure of a single alignment scan dot array. Second, two sets of alignment scan marks were used. The first set was written by aligning with the crystallite, developed, and metallized using 100 nm of Al and 100 nm of Au. PMMA resist was then reapplied and a second set of alignment marks written at 45° to the first set by aligning with the first set of alignment marks
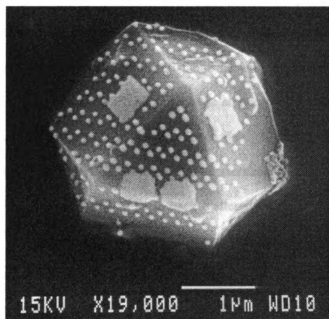
Figure 57 Microcrystallite showing metallized dot artifacts from overexposed alignment scan.

rather than with the crystallite. This second set of alignment marks was metallized with 15 nm of Ti and 200 nm of Au. The Al underlayer of the first set of alignment marks and any unwanted alignment scan dots was etched off in NaOH, taking the Au overlayer with it and leaving only the second set of alignment marks and a clean crystallite behind. Subsequent alignment was always done using the second set of alignment marks so that the thin PMMA on top of the crystallite was no longer in danger of exposure during alignment.

3.   ALIGNMENT MARK VISIBILITY THROUGH THICK POLYMER LAYERS

Another important consideration in electron-beam lithography was the visibility of various alignment features underneath layers of polyimide, PMMA, or both. The electron-beam in a scanning electron microscope interacts with the electrons and nuclei of the atoms in a sample and produces two kinds of emitted electrons. The first kind, called secondary electrons, originate from interactions of the beam with the electron cloud of a sample's atoms and have low energy. Their

energy is so low that they are unable to escape the sample if created deep within its bulk. These are the electrons detected by the SEM's secondary electron detector and provide the image signal for most viewing applications since they are characteristic of the sample's surface. The second kind of electrons originate from interactions of the beam with the atomic nuclei in the sample. They have high energy and provide a strong back-scattered electron flux. Hence their name, back-scattered electrons. Their energy is high enough, up to the full acceleration voltage energy, to escape from deep within a sample's bulk. The flux of these back-scattered electrons depends strongly on the atomic number Z of the sample's atoms, with higher atomic number providing stronger back-scattering and a higher flux. The SEM's back-scattered electron detector is specially positioned to detect these very directional, high energy electrons. Some back-scattered electrons are also detected by the secondary electron detector, however, providing a partial signal from within a sample's bulk. Hence, high-Z materials can be effectively seen in normal viewing mode below several microns of low-Z material provided there is enough material to create a sufficiently strong back-scattered signal at the secondary electron detector. Thick Au layers were always used to metallize alignment features to provide a large backscattered electron signal. The alignment marks were visible even under several microns of low-Z polymers like PMMA or polyimide, provided at least 100 nm of Au was used to provide enough contrast to the surrounding silicon substrate. Even very thick aluminum was unsuitable since its atomic number nearly matches that of the silicon substrate. Ti was used under the thick Au layer to improve adhesion.

4. CONTAMINATION BY SEM HYDROCARBONS

If a small field of view, say 10x10 μm^2, is maintained on the JEOL-840A scanning electron microscope the sample will appear to darken with time due to contamination build-up. This build-up is due to interaction of the electron beam with contaminants from the sample surface and hydrocarbon vapors in the high-vacuum sample chamber. Since the sample chamber

and gun chamber of the electron microscope were continuously pumped by an oil diffusion pump without the precaution of an intermediate cold trap to prevent oil backstreaming, it is assumed that hydrocarbon vapors were the most likely source of beam-interaction contamination layers. Precautions were necessary when viewing samples with sensitive surface chemistry. In the case of diamond microcrystals, virgin diamond surfaces and crystallites with Ti/Au contact pads were protected by > 20 nm of sacrificial Al film when photographed. The Al film was etched off in NaOH afterward, taking the SEM contamination with it. Protective Al coatings could not be used in the case of microcrystallites with polyimide layers, however, because of the risk of etching the polyimide upon removal of the Al film. Hence, no SEM photographs were taken of working microcrystallite devices prior to measurement to avoid the possibility of altering their measured electrical properties with an electrically different contamination layer.

APPENDIX B

APPENDIX B

ELECTRON-FOCUSING IN BI USING LITHOGRAPHIC POINT CONTACTS

1. ABSTRACT

An electron-beam lithography technique for fabricating submicron point-contacts to planar surfaces of bulk samples is described. We have demonstrated the technique by creating a linear array of point-contacts, oriented along the bisectrix axis of a bismuth single crystal, which act as emitters and collectors in multiprobe transport measurements. In a transverse electron focusing geometry, we find the expected series of periodic voltage peaks as a function of applied magnetic field at low temperatures. The lithographically fabricated contacts offer advantages over conducting-needle probes in electrical integrity, thermal robustness, lack of damage to the contact site, ability to make multiple submicron contacts with < 10 μm separations, and ability to align the contacts precisely along crystallographic axes.

2. EXPERIMENT

Transverse electron focusing (TEF) is a ballistic transport phenomenon which has been observed in long mean free path bulk metal samples[150,151] and in the 2-dimensional electron gas of inversion layer devices.[152] It has been used to study the interaction of charge carriers with boundaries[153] and surface structures[151] and the electronic properties of point contacts.[154] As illustrated in Figure 58, TEF in bulk metals requires two point contacts at the surface of a high purity single crystal. Current is injected at an emitter (E) and a voltage is measured at a collector (C) when the current carriers are focused onto C by application of a spatially uniform magnetic field of suitable magnitude lying in the plane of the surface of interest and perpendicular to the contact line between E and C.
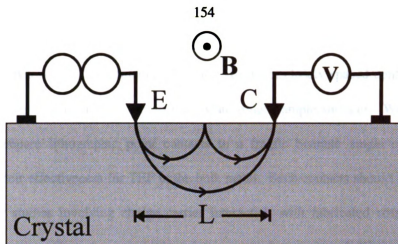
Figure 58 Electron focusing geometry showing emitter E, collector C, magnetic field B, and electron trajectories for field values B_0 and $2B_0$.

If the electron mean-free-path l_e is larger than the contact separation, the electrons travel ballistically from E to C. As the field is increased, they undergo increasing numbers of specular reflections from the metal surface between E and C. The field-dependent collector voltage, called a focusing spectrum, contains peaks at field values for which the contact separation is an integral number of half orbits. The focusing spectrum provides information about the Fermi surface shape, point contact dimensions,[155] metal surface quality in the region between the contacts,[151] and scattering in the point contact region.[154]

Point contacts for electron focusing in bulk metals have previously been produced using electrochemically sharpened conducting needles carefully brought into contact with the metal surface.[156] These contacts, also known as Sharvin probes, can be manipulated at cryogenic temperatures, but it is difficult to make more than a few contacts at a time and contact separations are $\geq$ 10 μm. Two-dimensional lithographic techniques have been used to create point contact constrictions in 2D electron gas devices[157] and 3D nanobridges for point contact spectroscopy,[158] but are not directly applicable to facilitating 3D contacts to bulk samples.

We describe here a lithographic technique for fabricating 3D point contacts to planar surfaces which can leave even mechanically soft bulk single crystals undamaged. These contacts

are fixed in position, but can be precisely oriented and positioned at separations less than 10 μm with contact diameters down to a fraction of a μm. Arrays of closely spaced contacts are feasible and the contact size can be adjusted to accommodate rough sample surfaces. We have used this technique to prepare lithographic point contacts to a fragile bismuth single crystal and have demonstrated their effectiveness for TEF in the bulk metal. Such contacts should facilitate diverse ballistic carrier studies involving charge carrier interaction with fabricated structures on metal surfaces, interference effects from multiple point contacts, hot electron ballistic transport,[159] and TEF in bulk materials with relatively short mean free paths.[160]

The point contacts are created by etching μm-sized holes through a thin dielectric layer to expose submicron areas of substrate surface for metallization. The first step in the fabrication process is to spin-apply a 0.5 μm layer of polyimide[161] to a clean, flat substrate surface at 5000 rpm for 60 seconds. The sample is then baked for 30 minutes at 140 °C to partially cure the polyimide. Layers thinner than 0.5 μm typically lack sufficient insulating integrity for surfaces with micron-sized roughness and show evidence of a very thin, wet etch-resistant layer at the substrate surface in regions of direct electron beam interaction during the first lithography step described below. Macroscopic metallic contact pads with tapered edge profiles are deposited on top of the polyimide layer by thermal evaporation through a mechanical mask mounted a few tenths of a millimeter above the substrate surface. Significant heating of the thin polyimide layer during this deposition is avoided by cooling the sample to -130 °C in the evaporator and then depositing metal a few hundred angstroms at a time, shuttering the sample for 60 seconds after every few hundred angstroms to allow surface heat to dissipate. We use 230 nm total thickness of Ag deposited 50 nm at a time at 1 to 3 nm/s.

PMMA electron-beam resist is then spin-applied over the surface and baked in a preheated oven for 30 minutes at 140 °C to form a 0.25 μm layer. Electron-beam lithography at 35 keV is used to define 0.2 μm diameter holes in the resist which serve as mask apertures for wet etching the

polyimide layer. The resist mask is exposed to an oxygen reactive ion etch (RIE) at 50 mtorr for 30 seconds to ensure that the apertures are clean and uniform. The polyimide film is then wet etched through the mask by dipping in an agitated 0.25 N NaOH solution held at 30 °C. Mask aperture uniformity is particularly important for this step to ensure that all the holes in an array etch at the same rate, since the etch rate is aperture size-dependent for submicron aperture diameters. The etching is stopped after 6 minutes by rinsing in deionized water when the substrate surface is just exposed.

The minimum exposed contact area depends on precise control of the etch duration. The wet etch profile is nearly hemispherical for aperture diameters much less than the polyimide layer thickness, so thinner polyimide layers provide for steeper etch-profile slopes at the substrate surface and, consequently, more control over the contact size through more relaxed etch time requirements. We obtain contact diameters down to 0.4 μm on smooth evaporated film test substrates using a 0.5 μm polyimide layer. We have also produced contact diameters $\gtrsim$ 0.1 μm by stopping the wet etch before the substrate is exposed and using an anisotropic RIE through the 0.1 μm mask aperture to etch the thinned polyimide layer. However, it is difficult to RIE through such long, narrow apertures and RIE processes are likely to produce damage at the contact area. The resist mask is dissolved in acetone leaving behind an array of etched pits in the polyimide with tapered sides and submicron areas of exposed, undamaged substrate at the bottom. Examples of the etch profiles in the polyimide layer are shown in Figure 59 (on Si substrate) and Figure 60 (on a Bi film on Si substrate) for the "wet" and "wet + RIE" techniques, respectively. The outer circle in Figure 60 is the outer rim of the wet etched bowl and the inner circle is the outer rim of the RIE hole in the bottom of the bowl. The bright spots in Figure 60 are due to backscattered electrons from Bi grains comprising the underlying Bi film.

A second electron-beam lithography step connects the contact areas to the metal pads on top of the polyimide film. A fresh layer of PMMA is applied to the etched polyimide surface and
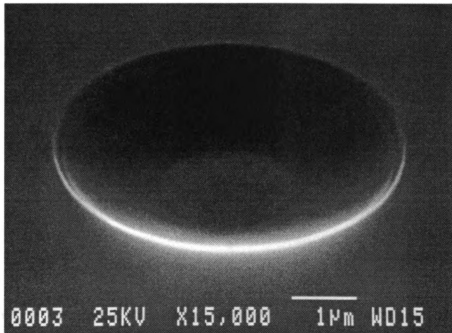
Figure 59 Wet etch profile in polyimide layer on Si substrate. (50° side view.)
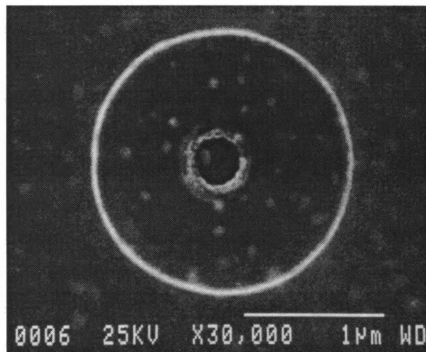

Figure 60 Wet + RIE etch profile in polyimide layer on Bi film, viewed normal to substrate.
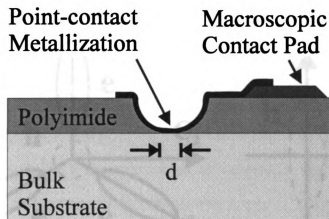
Figure 61 Metallized point-contact of diameter d.

baked as before. The resist is lithographically patterned so that unmasked regions overlap both an exposed point contact area and a corner of a macroscopic contact pad. The sample is metallized with 200 nm of thermally evaporated Ag and the mask lifted off, leaving each point contact area electrically connected to a corresponding metal contact pad, Figure 61.

We have used this lithographic technique to create point contact arrays on a Bi single crystal for electron focusing experiments. Single crystal Bi has $l_e > 100$ μm below 4 K. The Bi Fermi surface consists of three elongated electron ellipsoids (major to minor axis ratio is 15) declined by 6°23′ from the C_1-C_2 plane, and one hole ellipsoid parallel to the C_3-axis as shown in Figure 62.[162] For a crystal with top surface normal to the C_3 crystal axis and contacts aligned along the C_2-axis, injected charge carriers can be focused along a nearly cylindrical cross-section of the C_1 ellipsoid by a magnetic field applied parallel to the C_1 direction.

The Bi crystal was grown in a quartz mold in the shape of a circular disk 2 mm thick and 18 mm diameter with top face normal to the C_3-axis. The crystal surface was unpolished with micron-scale roughness from the mold. The crystal was mounted with GE varnish to a polished copper substrate. Laue back-reflection x-ray scattering determined the orientation of its C_2-axes relative to a designated edge of the copper substrate to within a few tenths of a degree. Linear arrays
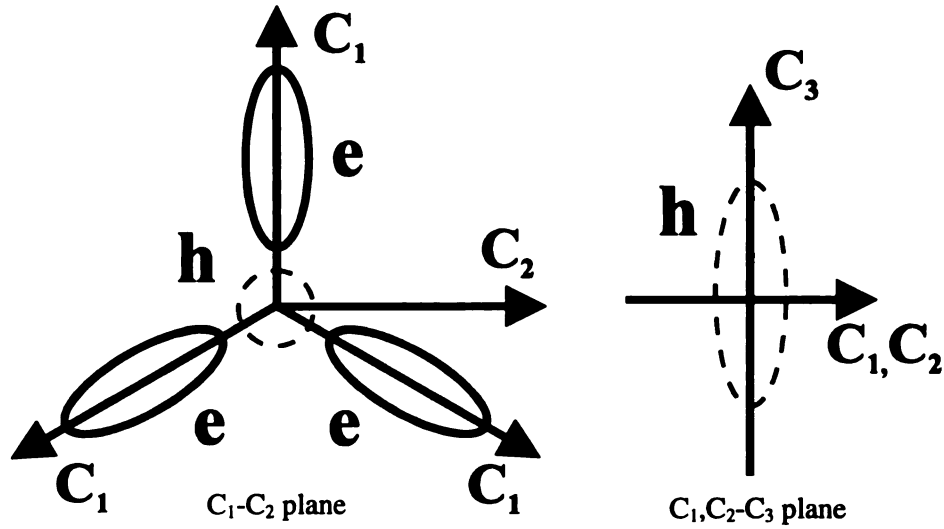
Figure 62 Bi Fermi surface for electrons (solid ellipses) and holes (dashed ellipses) projected onto the C1-C2 plane and C1,C2-C3 planes of the binary (C_1), bisectrix (C_2), and trigonal (C_3) crystallographic axes.

consisting of four point contacts with 20, 40, and 80 μm separations were produced on smooth surface regions. In addition, the sample was subjected to a low pressure anisotropic oxygen RIE while the PMMA etch mask was still in place to ensure that at least a small region of each exposed substrate area the size of the aperture was clean of polyimide residue in the event that the wet etch was not complete. The arrays were aligned to within a degree of the C_2-axis during electron-beam lithography. The sample was loaded into a helium dilution refrigerator with the magnetic field along the C_1-axis.

We made four-terminal measurements of the magnetic field-dependent collector voltage to 13.6 T at fixed sample current and two-terminal measurements of sample current vs. applied voltage at constant field. For TEF, only the low-field region, ± 0.03 T, is of interest. Measurements were done at fixed temperatures between 0.1 and 4.2 K using a lock-in amplifier operating near 80 Hz. No significant heating effects were observed for the 5 μA to 5 mA currents used.

Two-terminal current-voltage curves for measurements between point contacts and a crystal-ground contact were linear up to 0.5 mA and 50 mV, indicating Ohmic contact. The sample

contacts survived repeated cycling from room temperature to 4 K over the course of several data runs and, except in a few cases, were electrically stable without high voltage spot welding. An example of the collector voltage vs. normalized field in an electron focusing geometry is shown in Figure 63. The focusing geometry shown in Figure 58 was used. The measuring current was 0.1 mA and the temperature was fixed at 1.15 K. The positive field spectrum shows peaks in the collector voltage periodic in B superimposed on an increasing background. The nth peak corresponds to electrons impinging on the collector after n specular reflections from the sample surface. The reverse field spectrum shows only a very slow rise in collector voltage without peaks, because the negative field bends electrons away from the collector for this geometry. Focusing peaks are expected to vanish for field values larger than that corresponding to a cyclotron orbit diameter $d_c = 2m^*v_F/eB$ the same size as the effective collector contact diameter d. The peaks in Figure 63 disappear for $B/B_0 > 6$ (B $\approx$ 0.024 T), indicating d = 3.4 μm, which is comparable to our visual estimate of 3.7 μm for the exposed contact area at the bottom of the polyimide etch pit for this collector contact. Figure 64 shows bi-directional electron-focusing which can occur when the center of three closely spaced colinear contacts is used as a collector while the outside two contacts are used as injectors of a.c. current. The spectrum has a non-zero component in -B and -V because of phase-locked detection. The peak periodicity for +B is half that observed for -B because the E-C separation is half that of the contacts responsible for the -B spectrum. (See contact diagram in Figure 64.) This is the first bi-directional electron-focusing spectrum ever observed. The effective contact diameter was much larger than the area exposed to the oxygen RIE, suggesting that the wet etch was a complete process and that the RIE step was not required to ensure a clean, polyimide-free contact area prior to metallization.

In summary, we have described a lithographic method for creating point-contacts to planar bulk samples and demonstrated that such contacts can produce TEF in a bulk bismuth single-crystal. These contacts enabled observation of the first bi-directional electron-focusing spectrum.

The contacts were electrically and thermally more stable than traditional 3D conducting-needle contacts and could be positioned with submicron precision. Non-damaging contacts with diameters $\geq 0.4\ \mu m$ were produced on smooth substrates using a wet-etch process. Smaller diameters are possible with better etch control, thinner polyimide layers (on smooth samples), and by employing RIE techniques which may damage the sample surface. Contact separations of a few microns are feasible, offering possibilities for ballistic transport experiments in μm-scale geometries.
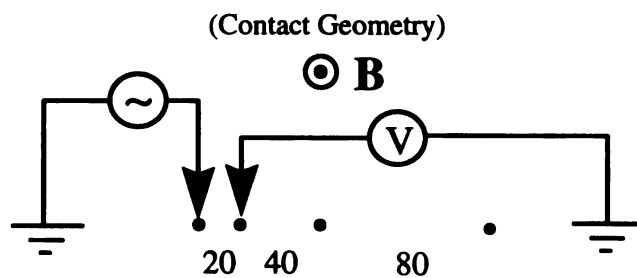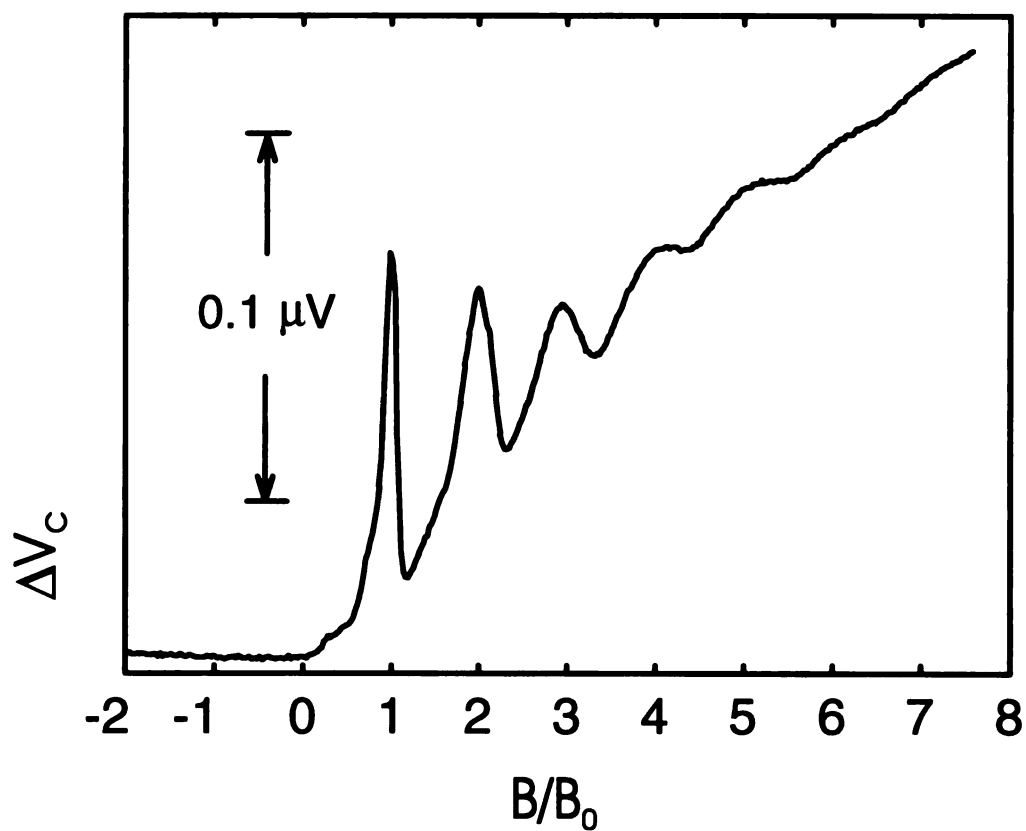
Figure 63 Change in collector voltage ΔV_c vs. normalized magnetic field B/B_0 at 1.15 K for 20 μm separation between point-contact injector and collector. (The other two contacts are to crystal ground.) The measuring current was 0.1 mA and the focusing peak periodicity $B_0 = 40.1$ gauss.
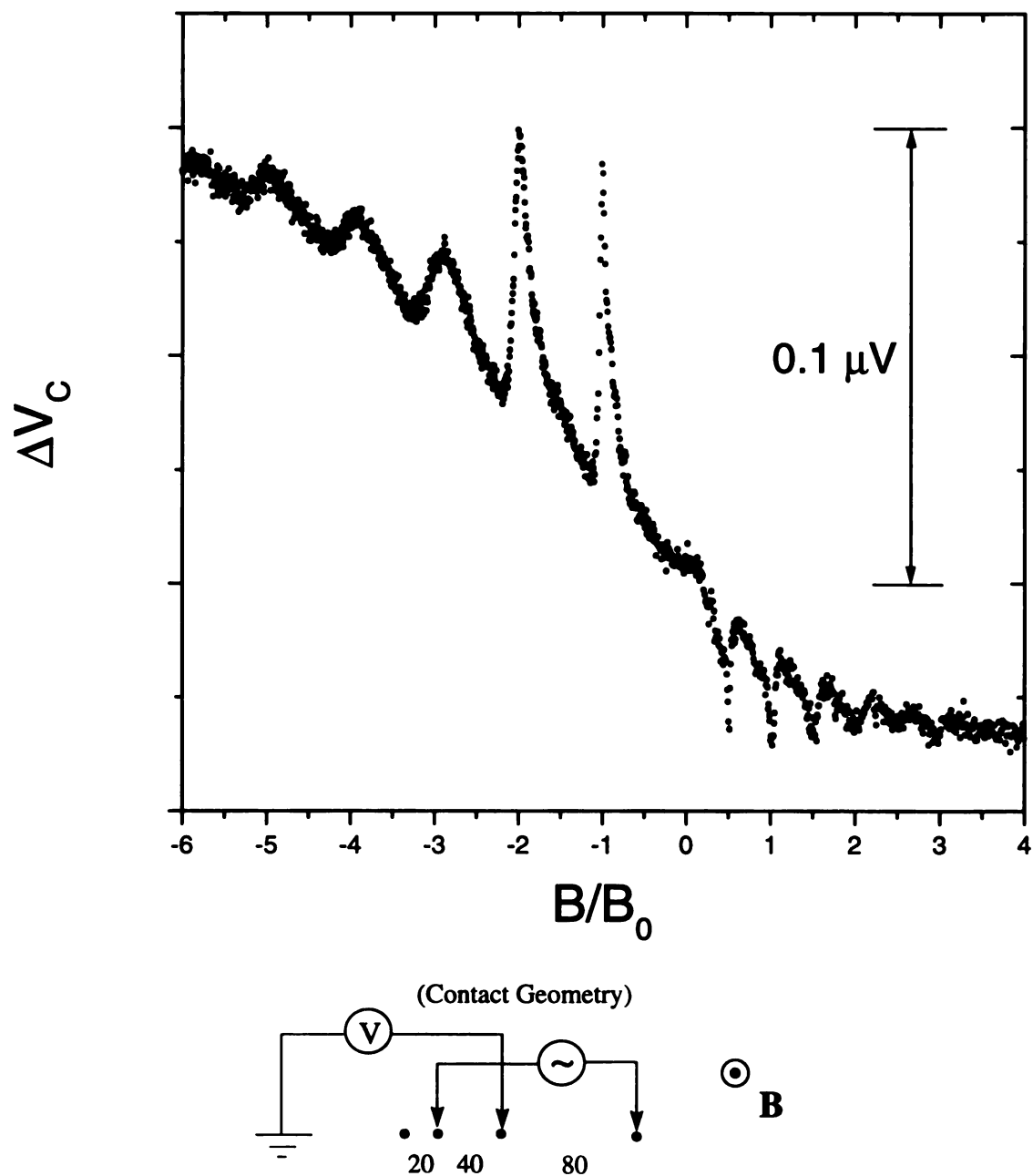
Figure 64 Bi-directional electron-focusing spectrum for colinear current and voltage point contacts where the current contacts straddle one voltage point contact. (One voltage contact is to crystal ground.) $B_0 = 21.2$ gauss, T = 0.21 K, I = 0.5 mA.

REFERENCES

REFERENCES

[1] D. M. Malta, J. A. von Windheim, H. A. Wynands, and B. A. Fox, "Comparison of the electrical properties of simultaneously deposited homoepitaxial and polycrystalline diamond films," J. Appl. Phys. **77**, 1536 (1995).

[2] S. M. Sze, *Physics of Semiconductor Devices* (John Wiley & Sons, Inc., New York, 1981).

[3] William Schockley, *Electrons and Holes in Semiconductors* (D. Van Nostrand Company, Inc., Princeton, NJ, 1950).

[4] J. S. Blakemore, *Semiconductor Statistics* (Pergamon Press Inc., New York, 1962).

[5] Neil W. Ashcroft and N. David Mermin, *Solid State Physics* (W. B. Saunders Company, Rinehart and Winston, Inc., Orlando, Florida, 1976), Chapters 8 and 12, pp. 131-241.

[6] J. S. Blakemore, ibid., pp. 16-48.

[7] S. Han, L. S. Pan, and D. R. Kania, "Dynamics of Free Carriers in Diamond", in *Diamond: Electronic Properties and Applications*, (Kluwer Academic Publishers, Norwell, MA, 1995). p. 242.

[8] S. M. Sze, ibid., pp. 22-4.

[9] J. S. Blakemore, ibid., p. 139.

[10] A.F. Ioffe, *Physics of Semiconductors*, (Academic Press, Inc., New York, 1957), pp. 157-84.

[11] B. I. Shklovskii and A. L. Efros, *Electronic Properties of Doped Semiconductors*, (Springer-Verlag, Berlin, Germany, 1984), Chap. 4.

[12] N. F. Mott and E. A. Davis, Philos. Mag. **17**, 1269 (1968).

[13] Herbert F. Mataré, *Defect Electronics in Semiconductors*, (John Wiley & Sons, Inc., New York, 1971).

[14] Herbert F. Mataré, ibid., p. 92.

[15] Herbert F. Mataré, ibid., p. 93.

[16] C. H. Seager and T. G. Castner, J. Appl. Phys. **49**, 3879 (1978); G. E. Pike and C. H. Seager, J. Appl. Phys. **50**, 3414 (1979); C. H. Seager and G. E. Pike, Appl. Phys. Lett. **35**, 709 (1979); C. H. Seager and G. E. Pike, Appl. Phys. Lett. **37**, 747 (1980).

[17] Jürgen Werner, "Electronic Properties of Grain Boundaries," in *Polycrystalline Semiconductors, Physical Properties and Applications*, ed. G. Harbeke, (Springer-Verlag, New York, 1985), p. 76.

[18] Figure adapted from S. M. Sze, ibid., p. 249.

[19] S. M. Sze, ibid., p. 264.

[20] Heinz K. Henisch, *Semiconductor Contacts, An approach to ideas and models*, (Clarendon Press, Oxford, 1984), p. 2.

[21] Charles Kittel and Herbert Kroemer, *Thermal Physics*, (W. H. Freeman and Compnay, New York, 1980), p. 376.

[22] Hong H. Lee, *Fundamentals of Microelectronics Processing*, (McGraw-Hill Publishing Company, New York, 1990), p. 116.

[23] Sheng S. Li, *Semiconductor Physical Electronics*, (Plenum Press, New York, 1993), pp. 281-2.

[24] Ronald J. Gillespie, David A. Humphreys, N. Colin Baird, and Edward A. Robinson, *Chemistry*, (Allyn and Bacon, Inc., Newton, MA, 1986), p. 356.

[25] C. Y. Fong and Barry M. Klein, "Electronic and Vibrational Properties of Bulk Diamond", in *Diamond: Electronic Properties and Applications*, ed. by Lawrence S. Pan and Don R. Kania, (Kluwer Academic Publishers, Norwell, MA, 1995), p. 3.

[26] W. N. Reynolds, *Physical Properties of Graphite*, (Elsevier Publishing Co. Ltd., New York, 1968), pp. 1-2.

[27] H. W. Kroto, J. R. Heath, S. C. O'Brien, R. F. Curl, and R. E. Smalley, *Nature* **318**, 162-163 (1985).

[28] Robert F. Curl and Richard E. Smalley, "Probing C_{60}," *Science* **242**, 1017 (1988).

[29] Thomas W. Ebbesen, "Carbon Nanotubes," *Physics Today* (June 1996), pp. 26-32.

[30] F. P. Bundy, "Diamond Synthesis and the Behavior of Carbon at Very High Pressures and Temperatures," *Annals of the New York Academy of Sciences* **105**, Art. 17, 951 (1964).

[31] H. B. Dyer, *et al.*, "Optical absorption features associated with paramagnetic nitrogen in diamond," Phil. Mag. **11**, 763 (1965).

[32] C. D. Clark, R. W. Ditchburn, and H. B. Dyer, "The absorption spectra of natural and irradiated diamonds," Proc. Royal Soc. (London) **A234**, 363 (1956).

[33] Michael W. Geis and John C. Angus, "Diamond Film Semiconductors," Scientific American (October 1992), pp. 84-89.

[34] Peter Bachmann, D. Leers, and H. Lydtin, "Towards a general concept of diamond chemical vapor deposition," Diamond and Relat. Mater. **1**, 1 (1991).

[35] Linda S. G. Plano, Kobe Steel USA Inc., Electronic Materials Center, "Growth of CVD Diamond for Electronic Applications," in *Diamond: Electronic Properties and Applications*, ed. by Lawrence S. Pan and Don R. Kania, (Kluwer Academic Publishers, Norwell, MA, 1995), p. 205.

[36] J. Khachan, J. R. Pigott, G. F. Brand, I. S. Falconer, and B. W. James, "A simple microwave plasma source for diamond deposition," Rev. Sci. Instrum. **64**, 2971 (1993).

[37] V. Venkatesan and K. Das, "Ohmic Contacts on Diamond by B Ion Implantation and Ti-Au Metallization," IEEE Electron Device Lett. **13**, 126 (1992).

[38] T. Sung, G. Popovici, M. A. Prelas, and R. G. Wilson, "Boron Diffusion Coefficient in Diamond," *Diamond for Electronic Applications*, Mat. Res. Soc. Symp. Proc. **416**, 467 (1996).

[39] B. E. Williams and J. T. Glass, "Characterization of diamond thin films: Diamond phase identification, surface morphology, and defect structures", J. Mater. Res. **4**, 373 (1989).

[40] Zhangda Lin, Jie Yang, Kean Feng, and Yan Chen, "Hetero-epitaxy of diamond film on silicon," *Applications of Diamond Films and Related Materials: Third International Conference, 1995*, ed. by A. Feldman, Y. Tzeng, W. A. Yarbrough, M. Yoshikawa, and M. Murakawa, NIST Special Publication 885, August 1995, p. 321.

[41] S. Yugo, T. Kanai, T. Kimura, and T. Muto, App. Phys. Lett. **58**, 1036 (1991).

[42] B. R. Stoner, P. J. Ellis, M. T. McClure, and S. D. Wolter, "Heteroepitaxial Nucleation of Diamond," *Diamond for Electronic Applications*, Mat. Res. Soc. Symp. **416**, 69 (1996).

[43] J. H. Won, A. Hatta, H. Yagyu, N. Jiang, Y. Mori, T. Ito, T. Sasaki, and A. Hiraki, "Effect of boron doping on the crystal quality of chemical vapor deposited diamond films," Appl. Phys. Lett. **68**, 2822 (1996).

[44] M. P. Everson and M. A. Tamor, "Investigation of growth rates and morphology for diamond growth by chemical vapor deposition," J. Mater. Res. **7**, 1438 (1992).

[45] Byungyou Hong, M. Wakagi, W. Drawl, R. Messier, and R. W. Collins, "Real Time Spectroellipsometry Study of the Evolution of Bonding in Diamond Thin Films During Nucleation and Growth," Phys. Rev. Lett. **75**, 1122 (1995).

[46] R. W. Collins, Y. Cong, Y. -T. Kim, K. Vedam, Y. Liou, A. Inspektor, and R. Messier, Thin Solid Films **181**, 565 (1989).

[47] R. E. Clausing, L. Heatherly, L. L. Horton, E. D. Specht, G. M. Begun and Z. L. Wang, Oak Ridge National Laboratory, "Textures and morphologies of chemical vapor deposited (CVD) diamond," Diamond and Related Materials **1**, 411 (1992).

[48] C. Wild, P. Koidl, W. Muller-Sebert, H. Walcher, R. Kohl, N. Herres, R. Locher, R. Samlenski, and R. Brenn, "Chemical vapour deposition and characterization of smooth, {100} facetted diamond films," Diamond Relat. Mater. **2**, 158 (1993).

[49] J. E. Graebner, S. Jin, G. W. Kammlott, Y. -H. Wong, J. A. Herb, and C. F. Gardinier, "Thermal conductivity and the microstructure of state-of-the-art chemical-vapor-deposited (CVD) diamond," Diamond Relat. Mater. 2, 1059 (1993).

[50] S. D. Wolter, B. R. Stoner, J. T. Glass, P. J. Ellis, D. S. Buhaenko, C. E. Jenkins, and P. Southworth, "Textured growth of diamond on silicon via in situ carburization and bias-enhanced nucleation," Appl. Phys. Lett. 62, 1215 (1993).

[51] B. R. Stoner, Chien-the Kao, D. M. Malta, and R. C. Glass, "Hall effect measurements on boron-doped, highly oriented diamond films grown on silicon via microwave plasma chemical vapor deposition," Appl. Phys. Lett. 62, 2347 (1993).

[52] Figure from "Diamond Technical Notes: Polycrystalline Diamond, March 1994," Technical brochure by Kobe Steel USA Inc., Electronic Materials Center, P. O. Box 13608, Research Triangle Park, NC 27709.

[53] W. Zhu, "Defects in Diamond," Diamond: Electronic Properties and Applications, ed. by Lawrence S. Pan and Don R. Kania, (Kluwer Academic Publishers, Norwell, MA, 1995), p. 175.

[54] W. Zhu, H. S. Kong, and J. T. Glass, "Characterization of diamond films", in Diamond Films and Coatings," ed. by R. F. Davis, (Noyes Publications, Park Ridge, NJ, 1993), p. 244.

[55] D. P. Malta, J. B. Posthill, R. A. Rudder, G. C. Hudson, and R. J. Markunas, "Etch-delineation of defects in diamond by exposure to an oxidizing flame," J. Mater. Res. 8, 1217 (1993).

[56] D. Shectman, J. L. Hutchison, L. H. Robins, E. N. Farabaugh, and A. Feldman, "Growth defects in diamond films," J. Mater. Res. 8, 473 (1993).

[57] Diane S. Knight and William B. White, "Characterization of diamond films by Raman spectroscopy," J. Mater. Res. 4, 385 (1989).

[58] R. E. Shroder, R. J. Nemanich, and J. T. Glass, "Analysis of the composite structures in diamond thin films by Raman spectroscopy," Phys. Rev. B 41, 3738 (1990).

[59] S. C. Sharma, et al., "Growth of diamond films and characterization by Raman, scanning electron microscopy, and x-ray photoelectron spectroscopy," J. Mater. Res. 5, 2424 (1990).

[60] Leah Bergman, K. F. Turner, P. W. Morrison, and R. J. Nemanich, "Micro-Raman Analysis of Stress State in Diamond Thin Films," Applications of Diamond Films and Related Materials: Third International Conference, 1995, ed. by A. Feldman, Y. Tzeng, W. A. Yarbrough, M. Yoshikawa, and M. Murakawa, NIST Special Publication 885, August 1995, p. 453.

[61] James R. Chelikowsky and Marvin L. Cohen, "Nonlocal pseudopotential calculations for the electronic structure of eleven diamond and zinc-blende semiconductors," Phys. Rev. B 14, 556 (1976).

[62] O. K. Andersen, "Linear method in band theory," Phys. Rev. B12, 3060 (1975); Su-Huai Wei, Henry Krakauer, and M. Weinert, "Linearized augmented-plane-wave calculation of the electronic structure and total energy of tungsten," Phys. Rev. B32, 7792 (1983).

[63] P. J. Dean, E. C. Lightowlers, and D. R. Wright, "Intrinsic and extrinsic recombination radiation from natural and synthetic aluminum-doped diamond," Phys. Rev. **40**, A352 (1965).

[64] S. M. Sze, ibid., pp. 848-51.

[65] Ronald J. Gillespie, *et al.*, ibid., p. 803.

[66] F. C. Champion, *Electronic Properties of Diamonds*, (Butterworth and Co. Ltd., London, 1963), p. 3.

[67] J. R. Olson, R. O. Pohl, J. W. Vandersande, A. Zoltan, T. R. Anthony, and W. F. Banholzer, "Thermal conductivity of diamond between 170 and 1200 K and the isotope effect," Physical Review B **47**, 14850 (1993).

[68] Robert C. Weast, ed., *Handbook of Chemistry and Physics, 60th Edition*, (CRC Press, Inc., Boca Raton, Florida), p. F-217.

[69] C. J. Rauch, *Proc. Int. Conf. on Phys. of Semiconductors*, ed. A. C. Strickland, (The Institute of Physics and the Physical Society, London, 1962), p. 276.

[70] L. Reggiani, S. Bosi, C. Canali, F. Nava, and S. F. Kozlov, "On the lattice scattering and effective mass of holes in natural diamond," Sol. State Comm. **30**, 333 (1979).

[71] F. Nava, C. Canali, C. Jacoboni, L. Reggiani, and S. F. Kozlov, "Electron effective masses and lattice scattering in natural diamond," Sol. State Comm. **33**, 475 (1980).

[72] J. S. Blakemore, ibid., pp. 58-9.

[73] E. C. Lightowlers, in *Science and Technology of Industrial Diamonds*, ed. J. Burls, (*Proc. Int. Diamond Conf.*, Vol. 1, Oxford, 1966), pp. 27-39.

[74] S. A. Kajihara, A. Antonelli, and J. Bernholc, "Impurity incorporation and doping of diamond," Physica B **185**, 144 (1993).

[75] N.Fujimori, H. Nakahata, and T. Imai, "Properties of boron doped epitaxial diamond films," Jpn. J. Appl. Phys. **29**, 824 (1990).

[76] K. Nishimura, K. Das and J. T. Glass, "Material and electrical characterization of polycrystalline boron-doped diamond films grown by microwave plasma chemical vapor deposition," J. Appl Phys. **69**, 3142 (1991).

[77] J. Mort, K. Okumura, and M. A. Machonkin, "Charge transport in boron doped diamond thin films," Phil. Mag. B **63**, 1031 (1991).

[78] B. Massarani, J. C. Bourgoin, and R. M. Chrenko, "Hopping conduction in semiconducting diamond," Phys. Rev. B **17**, 1758 (1978).

[79] R. G. Farrer, "On the substitutional nitrogen donor in diamond," Solid State Comm. **7**, 685 (1969).

[80] M. Neuberger, *Group IV Semiconducting Materials, Handbook of Electronic Materials,* Vol. 5, (IFI/Plenum Data Corporation, New York, 1971), p. 57.

[81] B. I. Shklovskii and A. L. Efros, *Electronic Properties of Doped Semiconductors,* (Springer-Verlag, Berlin, Germany, 1984), Chap. 4.

[82] Sir Nevill Mott, *Conduction in Non-Crystalline Materials,* (Clarendon Press, Oxford, 1987), pp. 27-9.

[83] Eric P. Visser, *et al.,* "Electrical conduction in homoepitaxial, boron-doped diamond films," J. Phys.: Condens. Matter **4,** 7365 (1992).

[84] M. I. Landstrass and K. V. Ravi, "Resistivity of chemical vapor deposited diamond films," Appl. Phys. Lett. **55,** 975 (1989); M. I. Landstrass and K. V. Ravi, "Hydrogen passivation of electrically active defects in diamond," Appl. Phys. Lett. **55,** 1391 (1989).

[85] Sacharia Albin and Linwood Watkins, "Electrical properties of hydrogenated diamond," Appl. Phys. Lett. **56,** 1454 (1990).

[86] Bob L. Mackey, John N. Russell, Jr., John E. Crowell, and James E. Butler, "Effect of surface termination on the electrical conductivity and broadband internal infrared reflectance of a diamond (110) surface," Phys. Rev. B, Rapid Comm. **52,** R17009 (1995).; Bob L. Mackey, John N. Russell, Jr., Pehr E. Pehrsson, John E. Crowell, and James E. Butler, "The effect of hydrogen on the electrical conductivity of the diamond (110) surface," Diamond Materials, ed. By J. P. Dismukes and K. V. Ravi, (The Electrochemical Society, Pennington, NJ, 1995), p. 455.

[87] Yusuke Mori, Hiroshi Kawarada, and Aiko Hiraki, "Properties of metal/diamond interfaces and effects of oxygen adsorbed onto diamond surface," Appl. Phys. Lett. **58,** 940 (1991).

[88] B. B. Pate, "Surfaces and Interfaces of Diamond," in *Diamond: Electronic Properties and Applications,* ed. by Lawrence S. Pan and Don R. Kania, (Kluwer Academic Publishers, Norwell, MA, 1995), pp. 45-60.

[89] Jürgen Werner, "Electronic Properties of Grain Boundaries," in *Polycrystalline Semiconductors: Physical Properties and Applications,* ed. by G. Harbeke, (Springer-Verlag, Heidelberg, 1985), pp. 76-94.

[90] M. A. Plano, *et al.,* Appl. Phys. Lett. **64,** 193 (1994).

[91] R. J. Graham *et al.,* Appl. Phys. Lett. **60,** 1310 (1992).

[92] D. M. Malta, J. A. von Windheim, and B. A. Fox, "Comparison of electronic transport in boron-doped homoepitaxial polycrystalline, and natural single-crystal diamond," Appl. Phys. Lett. **62,** 2926 (1993).

[93] B. A. Fox, M. L. Hartsell, D. M. Malta, H. A. Wynands, G. J. Tessmer, and D. L. Dreifus, "Electrical Properties of Diamond for Device Applications," *Diamond for Electronic Applications,* Mat. Res. Soc. Symp. Proc. **416,** 319 (1996).

[94] Y. Zhang, H. Ichinose, Y. Ishida, K. Ito, and M. Nakanose, "Atomic and electronic structures of grain boundary in chemical vapor deposited diamond thin film," *Diamond for Electronic Applications*, Mat. Res. Soc. Symp. Proc. **416**, 355 (1996).

[95] S. Han, *et al.*, "Correlation of Electrical Properties with Defects in a Homoepitaxial Chemical-Vapor-Deposited Diamond," *Diamond for Electronic Applications*, Mat. Res. Soc. Symp. Proc. **416**, 343 (1996).

[96] B. Fiegl, R. Kuhnert, M. Ben-Chorin, and F. Koch, "Evidence for grain boundary hopping transport in polycrystalline diamond films," Appl. Phys. Lett. **65**, 371 (1994).

[97] V. Venkatesan, K. Das, J. A. von Windheim, and M. W. Geis, "Effect of back contact impedance on frequency dependence of capacitance-voltage measurements on metal/diamond diodes," Appl. Phys. Lett. **63**, No. 8, 1065 (1993).

[98] Takeshi Tachibana and Jeffrey T. Glass, "Electrical Contacts to Diamond," in *Diamond: Electronic Properties and Applications*, ed. by Lawrence S. Pan and Don R. Kania, (Kluwer Academic Publishers, Norwell, MA, 1995), pp. 319-48.

[99] M. C. Hicks, *et al.*, "The barrier height of Schottky diodes with a chemical-vapor-deposited diamond base," J. Appl Phys. **65**, 2139 (1989).

[100] F. J. Himpsel, P. Heimann, and D. E. Eastman, "Schottky barriers on diamond (111)," Solid State Comm. **36**, 631 (1980).

[101] T. Tachibana and J. T. Glass, "Effects of argon presputtering on the formation of aluminum contacts on polycrystalline diamond," J. Appl. Phys. **72**, 5912 (1992).

[102] Johan F. Prins, "Preparation of ohmic contacts to semiconducting diamond," J. Phys. D: Appl. Phys. **22**, 1562 (1989).

[103] C. A. Hewett, J. R. Zeidler, and M. J. Taylor, C. R. Zeisse, and K. L. Moazed, "Specific contact resistance measurements of ohmic contacts to diamond," in *New Diamond Science and Technology*, ed. By R. Messier, J. T. Glass, J. E. Butler, and R. Roy, (Materials Research Society, Pittsburgh, 1991), p. 1107.

[104] K. L. Moazed, Richard Nguyen, and James R. Zeidler, "Ohmic Contacts to Semiconducting Diamond," IEEE Electron. Dev. Lett. **9**, 350 (1988).

[105] K. L. Moazed, J. R. Zeidler, and M. J. Taylor, "A thermally activated solid state reaction process for fabricating ohmic contacts to semiconducting diamond," J. Appl. Phys. **68**, 2246, (1990).

[106] C. A. Hewett, M. J. Taylor, J. R. Zeidler, and M. W. Geis, "Specific contact resisitance measurements of ohmic contacts to semiconducting diamond," J. Appl. Phys. **77**, 755 (1995).

[107] S. A. Grot, *et al.*, "The Effect of Surface Treatment on the Electrical Properties of Metal Contacts to Boron-Doped Homoepitaxial Diamond Film," IEEE Electronic Device Lett. **11**, 100 (1990).

[108] Ashraf Masood, "Technology and Electronic Properties of Diamond Film Microsensors for Thermal Signals," (Michigan State University thesis, 1992), p. 52.

[109] Ultra Virgin Diamond Powder, 0.1 μm, Type: Natural, Lot No. 9-1463, Amplex Corp., Bloomfield, CT 06002 (Provided by Professor Mohammad Aslam, EE Dept., MSU).

[110] Laimer, Shimokawa, and Matsumoto at NRIM in Japan, Diamond and Related Materials 3, 231-8 (1994).

[111] M. P. Everson and M. A. Tamor, "Studies of nucleation and growth morphology of boron-doped diamond microcrystals by scanning tunneling microscopy," J. Vac. Sci. Technol. B 9, 1570 (1991).

[112] B. R. Stoner, P. J. Ellis, M. T. McClure, and S. D. Wolter, "Heteroepitaxial Nucleation of Diamond," *Diamond for Electronic Applications*, Mat. Res. Soc. Symp. Proc. 416, 69 (1996).

[113] Hot -filament diamond growth facilities provided by Professor Mohammed Aslam, Dept. of Electrical Engineering, Michigan State University, East Lansing, MI.

[114] Diamond deposition by microwave plasma-assisted CVD by Kobe Steel USA Inc., Electronic Materials Center, 79 T. W. Alexander Drive, P.O. Box 13608, Research Triangle Park, NC, 27709.

[115] D. M. Malta, J. A. von Windheim, H. A. Wynands, and B. A. Fox, "Comparison of the electrical properties of simultaneously deposited homoepitaxial and polycrystalline diamond films," J. Appl. Phys. 77, 1536 (1995).

[116] Mike Marchywka, Pehr E. Pehrsson, Steven C. Binari, and Daniel Moses, J. Electrochem. Soc., 140, L19 (1993).

[117] Pehr E. Pehrsson, Mike Marchywka, James P. Long, James E. Butler, "Electrochemical Surface Modification of Diamond", *Applications of Diamond Films and Related Materials: Third International Conference, 1995*, ed. by A. Feldman, Y. Tzeng, W. A. Yarbrough, M. Yoshikawa, and M. Murakawa, (NIST Special Publication 885, August 1995), p. 267.

[118] D. K. Reinhard, *Introduction to Integrated Circuit Engineering*, (Houghton Mifflin Company, Boston, MA, 1987), p. 388.

[119] Omega Technologies Company, *The Temperature Handbook*, (Omega Engineering, Inc., Stamford, CT, 1989), p. Z-10.

[120] M. H. Grimsditch, E. Anastassakis, and M. Cardona, Phys. Rev. B 18, 901 (1978).

[121] S. M. Sze, ibid., p. 44.

[122] John E. Graebner, "Thermal Conductivity of Diamond," in *Diamond: Electronic Properties and Applications*, ed. by Lawrence S. Pan and Don R. Kania, (Kluwer Academic Publishers, Norwell, MA, 1995), p.290.

172

123 William Schockley, ibid., pp. 466-475.

124 Ken Okano, "Doped Diamond," in *Diamond: Electronic Properties and Applications*, ed. by Lawrence S. Pan and Don R. Kania, (Kluwer Academic Publishers, Norwell, MA, 1995), pp. 139-74.

125 S. M. Sze, ibid., p. 281.

126 M. F. Thorpe, S. Hyun, and R. Day, M. D. Jaeger, and B. Golding, to be published.

127 L. J. van der Pauw, "A Method of Measuring Specific Resistivity and Hall Effect of Discs of Arbitrary Shape," Philips Research Reports **13**, 1 (1958).

128 Seeger, Karlheinz, *Semiconductor Physics, An Introduction*, (Springer-Verlag, New York, 1991), p. 62-3.

129 Yicai Sun, Oswin Ehrmann, Jürgen Wolf, and Herbert Reichl, "The correction factors and their new curve for the measurement of sheet resistance of a square sample with a square four-point probe," Rev. Sci. Instrum. **63**, 3752 (1992).

130 American Society for Testing and Materials, "Standard Method for Measuring Hall Mobility and Hall Coefficient in Extrinsic Semiconductor Single Crystals," ASTM Designation: F 76-86, 1986.

131 Professor Mike Thorpe, Physics and Astronomy Department, Michigan State University, East Lansing, MI, 48824-1116.

132 Sangil Hyun, Department of Physics and Astronomy, Michigan State University, East Lansing, MI.

133 Professor Roy Day, Department of Physics, Marquette University, Milwaukee, WI.

134 Minimization routine written by Professor Roy Day, Department of Physics, Marquette University, Milwaukee, WI.

135 Finite element analysis performed by Sangil Hyun, Department of Physics and Astronomy, Michigan State University, East Lansing, MI.

136 Finite element analysis packages used were "ABAQUS" and "ANSYS."

137 Image generated by Sangil Hyun using finite element analysis.

138 S. M. Sze, ibid., p. 34.

139 Sir Nevill Mott, *Conduction in Non-crystalline Materials*, (Oxford University Press, New York, 1987), p. 59.

140 A. T. Collins, Philos. Trans. R. Soc. London Ser. A **342**, 233 (1993).

[141] J. C. Bougoin, J. Krynicki, and B. Blanchard, Phys. Status Solidi A **52**, 293 (1979); K. Nishimura, K. Das, and J. T. Glass, "Material and electrical characterization of polycrystalline boron-doped diamond films grown by microwave plasma chemical vapor deposition," J. Appl. Phys. **69**, 3142 (1991).

[142] I. Taher, M. Aslam, M. A. Tamor, T. J. Potter, and R. C. Elder, "Piezoresistive microsensors using p-type CVD diamond films," Sensors and Actuators A **45**, 35 (1994).

[143] M. Werner, *et al.*, "Charge transport in heavily B-doped polycrystalline diamond films," Appl. Phys. Lett. **64**, 595 (1994).

[144] DuPont Bulletin #PC-1 H-24264 2/90, DuPont Company, Electronics Department, P.O. Box 80030, Wilmington, DE 19880-0030.

[145] DuPont Company, Electronics Department, P.O. Box 80030, Wilmington, DE 19880-0030.

[146] M. D. Jaeger, V. Tsoi, and B. Golding, "Lithographic point contacts for transverse electron focusing in busmuth," Appl. Phys. Lett. **68**, 1282 (1996).

[147] DuPont Bulletin #H-24252 2/90, DuPont Company, Electronics Department, P.O. Box 80030, Wilmington, DE 19880-0030.

[148] Nabity Pattern Generation System, Version 7.2, 1992, J. C. Nabity Lithography Systems, P. O. Box 5354, Bozeman, MT 59717.

[149] DesignCAD software by American Small Business Machines, Inc.

[150] V. S. Tsoi, Sov. Phys. JETP Lett. **19**, 70 (1974).

[151] V. S. Tsoi, J. Bass, and P. Wyder, Adv. Phys. **41**, 365 (1992).

[152] H. van Houten, B. J. van Wees, J. E. Mooij, C. W. J. Beenakker, J. G. Williamson, and C. T. Foxon, Europhys. Lett. **5**, 721 (1988).

[153] V. S. Tsoi, Sov. Phys. JETP **41**, 927 (1975).

[154] V. V. Andrievskii, E. I. Ass, and Yu. F. Komnik, Sov. Phys. JETP Lett. **47**, 124 (1988).

[155] V. S. Tsoi and N. P. Tsoi, Sov. Phys. JETP **46**, 150 (1977).

[156] Yu V. Sharvin, Sov. Phys. JETP **21**, 655 (1965); Yu V. Sharvin and L. M. Fisher, Sov. Phys. JETP Lett. **1**, 152 (1965).

[157] H. van Houten, C. W. J. Beenakker, J. G. Williamson, M. E. I. Broekaart, P. H. M. van Loosdrecht, B. J. van Wees, J. E. Mooij, C. T. Foxon, and J. J. Harris, Phys. Rev. B **39**, 8556 (1989).

[158] K. S. Ralls, R. A. Buhrman, and R. C. Tiberio, Appl. Phys. Lett. **55**, 2459 (1989).

[159] U. Sivan, M. Heiblum, and C. P. Umbach, Phys. Rev. Lett. **63**, 992 (1989).

[160] V. V. Andrievskii, E. I. Ass, and Yu F. Komnik, Sov. J. Low Temp. Phys. **16**, 179 (1990).

[161] We used PYRALIN PI-2555 polyimide coating supplied by the DuPont Company.

[162] V. S. Édel'man, Adv. Phys. **25**, 555 (1976).